Identifying Determinants of Antibiotic Resistance in Beta-lactamases

---

A Dissertation

Presented to
the faculty of the School of Engineering and Applied Science
in partial fulfillment of the requirements
for the degree

Doctor of Philosophy

---

by

George Albert Cortina

May 2018

DEPARTMENT OF BIOMEDICAL ENGINEERING

UNIVERISTY *of* VIRGINIA

Approval Sheet

This dissertation is in partial fulfillment of the requirements for the degree of Doctor of Philosophy in Biomedical Engineering

_____

George A. Cortina, Author

This dissertation has been read and approved by the examining committee:

_____

Dr. Peter Kasson
Dissertation Advisor
Department of Biomedical Engineering

_____

Dr. Jason Papin
Committee Chair
Department of Biomedical Engineering

_____

Dr. Kevin Janes
Committee Member
Department of Biomedical Engineering

_____

Dr. William Pearson
Committee Member
Department of Biochemistry and Molecular Genetics

_____

Dr. William Petri
Committee Member
Department of Microbiology and Infectious Diseases

Accepted for the School of Engineering and Applied Science

_____

Dr. Craig H. Benson
Dean
School of Engineering and Applied Science

Abstract

Antibiotic resistant infections greatly increase infectious disease mortality by rendering common drug therapies ineffective. Beta-lactamases mediate resistance to beta-lactam antibiotics, the most commonly prescribed class of antibiotics. Elucidating the mechanisms responsible for drug resistance in beta-lactamases aids in developing future antibiotics. Residues allosteric to the binding site are functionally important in conferring drug resistance and, therefore, predicting change in activity from mutations requires the study of all residues instead of just those in the binding-pocket.

To identify functionally important residues beyond the drug-binding site, we developed a pairwise measure of residue association in a beta-lactamase, CTX-M9, using molecular dynamics simulations. This method ranked residues across the beta-lactamase based on the association of their movement with drug binding-pocket movement. Experimental testing of mutations revealed that high ranking allosteric residues were functionally important to CTX-M9.

Large-scale molecular dynamics simulations provide a computationally intensive but powerful approach to predict mutations that specifically enhance activity. Using these, we identified mutations that increase CTX-M9's resistance by simulating point mutations and ranking the mutation based on a measure of drug hydrolysis favorability in the binding site. A subset of the top-ranking mutations demonstrated increased drug resistance and kinetic activity. Subsequent machine learning analysis revealed that these allosteric mutations resulted in specific changes to side chains in the binding-pocket.

Simulations also enable detailed physical chemistry and statistical learning-based approaches to probe the conformational changes controlling beta-lactamase catalysis and drug resistance. Through these simulations, we characterized a conformational transition responsible for controlling catalytic activity in another beta-lactamase, KPC-2, and identified residues that were responsible for this transition. Mutations to these residues alter this simulated transition in a manner that highly correlates with experimentally measured k_{cat} kinetic values, thus providing another tool to prospectively study the effect of allosteric mutations on drug resistance.

Acknowledgements

The work that follows would not have been possible without the help of many people. Therefore, I use first person singular in offering my ideas and proposals but employ first person plural to describe the findings and work. This is because the experiments and findings in this dissertation are the result of a team effort.

I would first like to acknowledge Dr. Peter Kasson for guiding me through my Ph.D. training. He challenged me to not let the tools I know limit the science I pursue but instead learn the methods needed for the question. This is demonstrated in the diversity of approaches in this dissertation which originate from disciplines such as biophysics, graph theory, microbiology, machine learning, molecular biology, and statistical theory. This provided me with a unique and interesting training experience. Now, preparing to defend, I am thankful for the unique opportunity I had through my training with Dr. Kasson.

Additionally, I would like to thank my committee members: Drs. Jason Papin, Peter Kasson, Kevin Janes, William Pearson and William Petri. Through my training, they have provided guidance on research strategies, experimental results, and strategies for developing well-thought experimental design. Their range of expertise made each committee meeting a rich experience and provided me with novel approaches and directions. I thank them for their time and expertise.

I would also like to acknowledge my lab-mates. First, Malgorzata Latałło, M.Sc., (Gosia) and I worked jointly on the findings in Chapter 3. She performed much of the wet-lab work, especially the kinetics and crystallography. Gosia learned advanced protein purification methods in order to study CTX-M9 and became extremely skilled at working with this very difficult enzyme.

Second, I would like to acknowledge Jennifer Hays. Jennifer implemented the selection and biasing methods in Chapter 4. Additionally, thanks to Jennifer, I can better spot logical holes and question blind assumptions. Lastly, her help and insight in reviewing parts of this dissertation greatly improved its flow and logic.

Beyond Jennifer and Gosia, I received a great deal of help from others in the Kasson laboratory. Drs. Bob Rawle and Eric Irrgang, two post-doctorals in the lab, have both aided me when I faced difficulties in their respective fields. Furthermore, Kasia Zawada, M.Sc., taught me numerous wet lab techniques such as Western Blots, PCR, and others.

Finally, I would like to thank my family. I would like to begin with my grandfather, Dr. Heber Newsome. An medical doctor and scientist, he taught me from a young age to think scientifically and love learning. Even through graduate school, I am incredibly thankful for his sympathetic ear and guidance. I would also like to thank my parents and family. An M.D./Ph.D. is a long endeavor and I could have never have embarked on it without their support.

Table of Contents

Table of Figures

Table of Tables

Chapter 1. Introduction: Antibiotic Resistance and Beta-lactamases

1.1 Foreword: Preparing for Future Bacterial Resistance

A majority of important advances in medicine from transplantation to cancer treatments rely on the ability to control infection [1–3]. Increasing resistance to current antibiotic therapies challenges the future utility of these advances [4–6]. Smarter drug design that specifically considers possible subsequent resistance can potentially avoid a future with incurable infections. In this dissertation, I identify and predict how future resistance may arise in a chief mediator of antibiotic resistance, beta-lactamases, and offer methods that could complement future drug design. This introduction is an overview of beta-lactamase-meditated resistance and a review of the challenges and opportunities in understanding causes of resistance in these enzymes.

1.2 Beta-lactam Antibiotics: A Foundation of Medicine

The discovery of penicillin in 1928 by Alexander Fleming and the first mass production of the antibiotic in 1943 marked a new era for medicine [7–9]. For the first time, clinicians had a safe and consistent means to treat bacterial infections, which served as the foundation for numerous future medical discoveries. Penicillin was the first of a class known as beta-lactam antibiotics. The name for “beta-lactam” antibiotics is a result of a core beta-lactam ring in their chemical structure (Figure 1.1). The beta-lactam ring is critical to the function of the drug [10]. Since penicillin, over 31 beta-lactam antibiotics have been developed with coverage of both gram positive and gram negative infections [11–13]. These drugs are the primary treatment in a wide range of infections such as meningitis, pneumonia, and strep throat [13,14]. As a result, beta-lactams are the most

frequently prescribed antibiotics and rank as one of the most commonly prescribed of all drugs [15]. In 2016, over 54 million prescriptions for amoxicillin, a penicillin, were written in the United States making this antibiotic alone the 12th most prescribed drug [16]. Therefore, the total number of prescriptions for this entire group is likely much higher.

The effectiveness of beta-lactam antibiotics is due to their core beta-lactam ring. Specifically, the beta-lactam is sterically similar to D-ala-D-ala peptidoglycan building blocks and acylates the active site of penicillin binding proteins (PBPs) [17,18]. PBPs aid bacteria in several functions related to cell wall synthesis and maintenance [19]. Once acylated by a beta-lactam these enzymes deacylate very slowly (8×10^{-6} s^{-1} for PBP2x) [20] and are therefore functionally inhibited [20]. PBP inhibition halts the synthesis and maintenance of peptidoglycan while breakdown continues. This results in the bacteria succumbing to osmotic stress and lysis, which allows the immune system to clear the infection [17,18].

1.3 Beta-lactamases Resist Beta-lactam Antibiotics

The arrival of beta-lactam clinical resistance soon followed the widespread clinical use of beta-lactams. By 1949 (six years after its first widespread use), half of all *Staphylococcus pyogenes* isolates were no longer susceptible to penicillin in U.K. hospitals [21]. By the 1950s, resistance was common and basic penicillin was no longer effective in broad clinical use [8]. The rise in beta-lactam resistance was a result of extreme selective pressure exerted by the use of these agents. Since then, resistance has continued to rise. Currently, deaths from antibiotic resistance exceed 23,000 in the United States with an overall incidence of over 2 million cases annually [22]. 70,000 global deaths occur annually, and it is predicted that by 2050 this number could increase to 10 million exceeding the 8.2 million that currently die annually from cancer [23].

There are several mechanisms of bacterial resistance to antibiotics. The focus of this work is on beta-lactamases which confer resistance by hydrolyzing beta-lactam antibiotics and render them ineffective. The success of beta-lactamases is a result of their simplicity and low evolutionary fitness penalty. First, resistance can be conferred with a single domain protein and thus, a single gene on a plasmid [24]. This allows for these enzymes to spread rapidly between bacterial species through the horizontal transfer of genetic material. Furthermore, beta-lactamases have a small fitness penalty as compared to other forms of beta-lactam resistance which involve: (i) modifying or replacing essential bacterial proteins, (ii) requiring ATP or (iii) modifying membrane permeability [25–27]. As a result, resistance through beta-lactamases can be acquired rapidly, but is rarely lost in the absence of antibiotics [28,29].

Since their arrival, the number of identified clinical beta-lactamases has quickly grown. In 2010, there were over 860 types of beta-lactamases [30]. Functionally, each beta-lactamase carries resistance to a subset of all beta-lactam antibiotics, known as its antibiotic spectrum. Currently, all beta-lactams are susceptible to at least one beta-lactamase, making no one drug effective against all resistance, which increases the urgency of understanding these enzymes [31].

1.4 Overview of Beta-lactam Groups Used in this Work

To combat increasing resistance to beta-lactamases, new types of beta-lactam antibiotics were developed resulting in several groups of beta-lactams. Currently, there are 6 classes of beta-lactams [32]. Each group is targeted to different types of bacteria and is susceptible to different families of beta-lactamases. Typically, these groups differ by the type of ring that is fused to the beta-lactam and by modifications of chemical R groups to those rings (Figure 1.1).

The three types of beta-lactams studied in this work are penicillins, cephalosporins, and carbapenems. Penicillins were the first generation of beta-lactam antibiotics (Figure 1.1A).

Generally, there is a high level of resistance to these beta-lactam antibiotics [12]. The second group cephalosporins, were first developed in the 1950's and 1960's (Figure 1.1B). This subgroup of antibiotics is further classified into generations based on their effectiveness against gram positive versus gram-negative bacteria. Later generations of cephalosporins, such as fourth generation, tend to be very effective against most beta-lactamases [13,33]. The third group carbapenems represent "last-resort" beta-lactams (Figure 1.1C). These antibiotics are used in hospitals for infections that carry resistance to all other beta-lactams antibiotics including penicillins and cephalosporins [11].

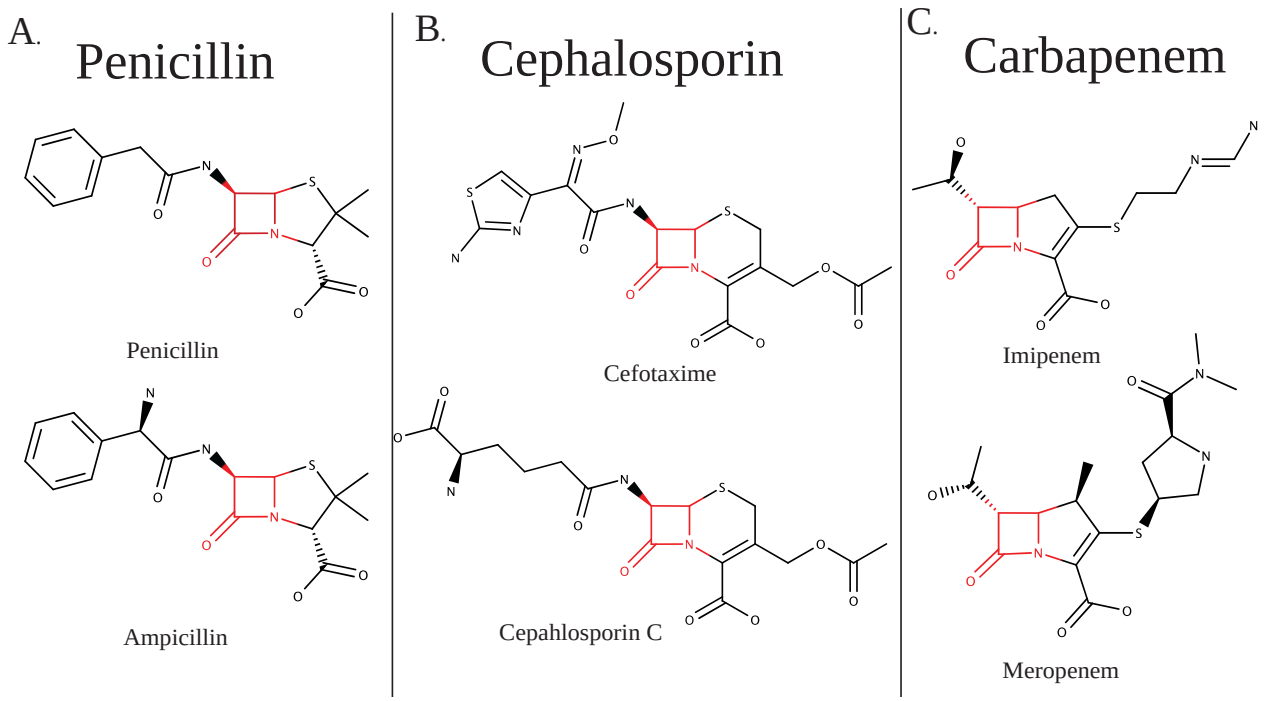

Figure 1.1 Chemical structures of common beta-lactam antibiotics
Example of beta-lactam antibiotics belonging to the classes penicillin (CID: 54607813, 6249) (A), cephalosporin (CID: 5742673, 65536) (B), and carbapenem (CID: 104838, 441130) (C). The core beta-lactam is shown in red. Most beta-lactams within each class have matching fused rings. Members are differentiated by the type of R group added to these fused rings [34].

1.5 Class A: Serine-mediated Beta-lactamases

Beta-lactamases are classified by their structural similarity and mechanism. These enzymes exist in four classes named alphabetically from A to D. Three of the classes, A, C, and D, are serine mediated and thought to have descended from PBP's [35]. The remainder of this dissertation focuses on class A beta-lactamases.

Class A beta-lactamases undergo a three-step reaction in their breakdown of beta-lactams. Schematically, the process would begin with the binding of the enzyme and substrate, which involves the entrance and positioning of the drug in the binding-pocket in conformations favorable to the acylation of the drug by the enzyme at the catalytic serine. This acylation then produces an acyl-enzyme. Finally, the hydrolysis of the serine-drug bond causes release of the hydrolyzed drug and return of the enzyme to the *apo* form (Figure 1.2) [27,36,37].

The deacylation of the acyl-enzyme (E-S) defines the resistance profile of a majority of Class A beta-lactamases and is an important process to understand. Most beta-lactamases form an acyl-enzyme with any beta-lactam drug. Therefore, beta-lactamase spectrum is marked by the drugs that the enzyme can deacylate at a rate that confers resistance. The process of deacylation occurs by the attack of water on the carbonyl moiety of the beta-lactam ring. This results in a high-energy tetrahedral deacylation intermediate, which leads to the hydrolysis of the bond between the drug and serine resulting in the release of the hydrolyzed beta-lactam and return of the enzyme to the *apo* form [27,37,38] (Figure 1.2).

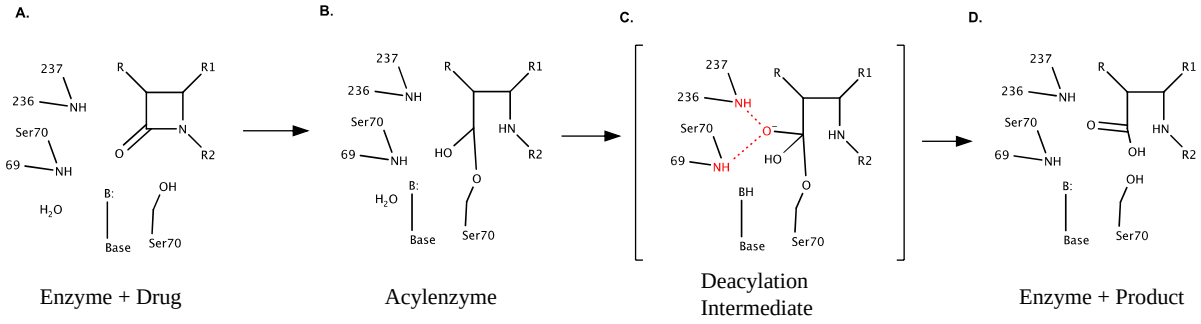

Figure 1.2 Reaction for class A beta-lactamases

Class A Beta-lactamases progress through a three-state reaction. Initially, the beta-lactam drug enters in the binding-pocket (A). This is followed by an attack by the catalytic serine resulting in the acyl-enzyme (B). Most beta-lactam and class A beta-lactamase combinations arrive at this state. The energetic favorability of the short-lived deacylation intermediate (C) determines antibiotic spectrum. This activation energy is lowered by the formation of an oxyanion hole (red) and results in a hydrolyzed product and release (D). Residues are labeled by position with conserved residues shown with their amino acid. Ser70 is broken into two sections of the chemical diagram for clarity on the reaction.

Because of the high energy of the deacylation transition state, the acyl-enzyme intermediate requires specific interactions to support deacylation. One critical interaction is the formation of the oxyanion hole. This hole is formed when backbone amides in the binding-pocket (residue 70 and 237) hydrogen bond with the beta-lactam carbonyl oxygen moiety. The result is a structure that supports an increasingly negative charge on the carbonyl oxygen and thus permits a nucleophilic attack on the beta-lactam carbonyl carbon [38–41]. In the tetrahedral intermediate, the oxyanion is subsequently supported by these bonds making this higher energy transition more favorable (Figure 1.2).

Along with the residues that support the oxyanion hole, it is theorized that additional side chains also coordinate the deacylation step (Figure 1.3). Specifically, Glu166 serves to coordinate with the hydrolytic water. This is supported by structural and kinetic studies that indicate that the Glu166Ala mutation prevents deacylation [42–44]. Additionally, it is thought that Ser130 plays a critical role in drug positioning by interacting with the carboxyl group on the adjoining ring to the beta-lactam ring or the amide on the beta-lactam ring [44,45]. These interactions permit deacylation and therefore determine the spectrum of the beta-lactamase [27,35,44,46]. This results in the energetic favorability of these conformations defining drug spectrum.

Within the class A family, enzymes can be sub-classified by drug spectrum. Members of this class have been organized into groups 2be, 2br, 2ber, and 2f through an antibiotic-spectrum-based classification scheme [30,47]. In general, the "2b" groups confer resistance to penicillins and some early generations of cephalosporins. Group "2be" consists of extended spectrum beta-lactamases (ESBL) [30,47]. ESBL's arose in the 1980s. They confer resistance to all oral beta-lactams resulting in inpatient treatment with intravenous antibiotics and poorer outcomes. More

recently discovered is group “2f”, which consists of serine-based enzymes and confer resistance to penicillins, cephalosporins, and carbapenems [30,47]. Members of this class of beta-lactamases are commonly detected in gram-negative bacteria such as *Klebsiella pneumoniae*, *Escherichia coli*, and *Pseudomonas aeruginosa*, which makes these infections extremely difficult to treat [48].

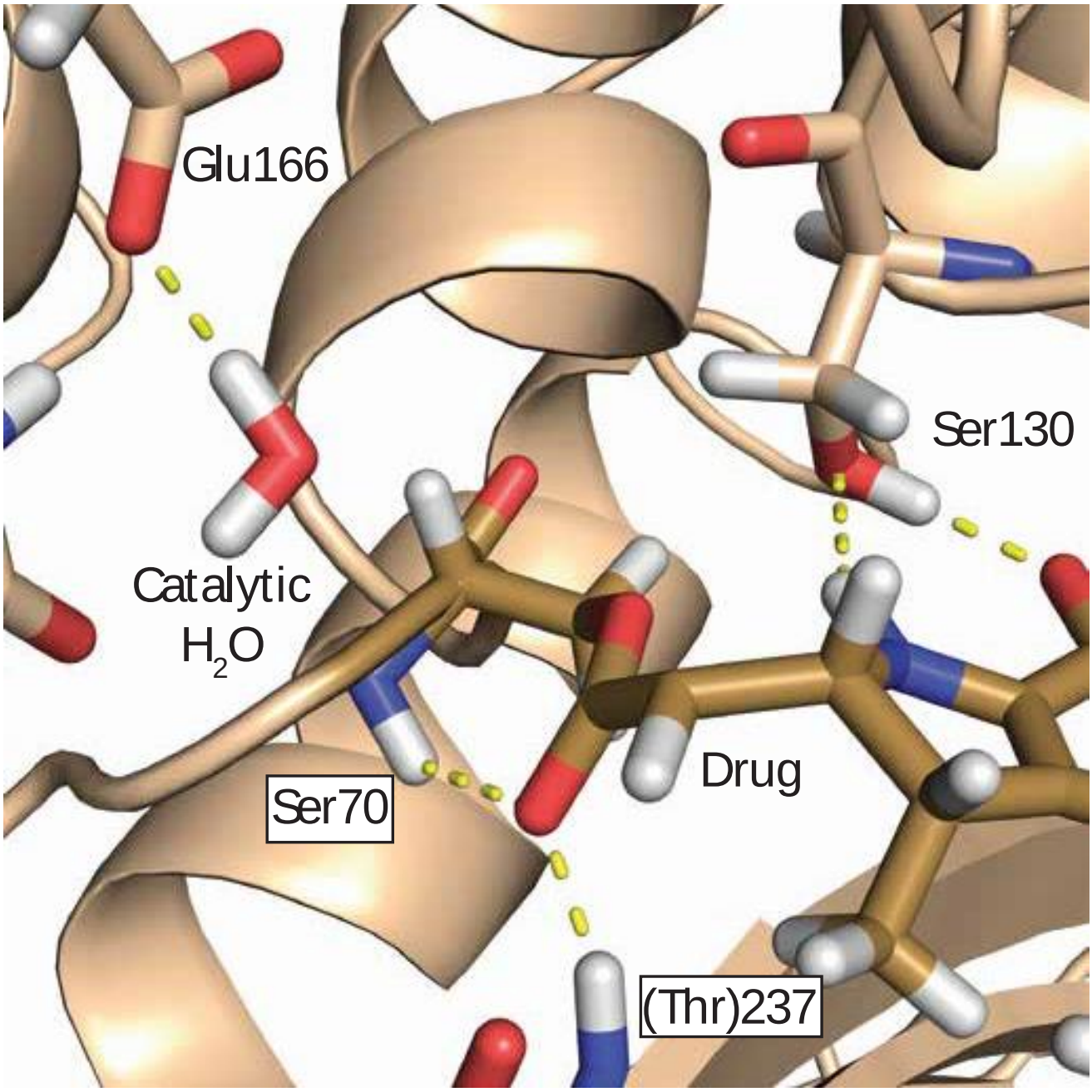

Figure 1.3 Binding-pocket residues that support deacylation
Rendering of binding-pocket residues that support deacylation. Ser70 and residue 237 hydrogen bond to carbonyl oxygen on the drug and support oxyanion hole formation. Glu166 coordinates with the deacylating water. Ser130 interacts with the amide on the ring adjacent to the beta-lactam ring (open in this state) and the carbonyl or carboxyl group on the drug. This rendering is of KPC-2, a member of the KPC family (Section 1.6), with meropenem; some atoms on meropenem are hidden for clarity. Conserved residues are noted by their amino acids while non-conserved residues show the KPC-2 amino acid in parentheses.

1.6 CTX-M and KPC-2 Beta-lactamase Families

CTX-M and KPC are two of the most concerning Class A beta-lactamase families. As a result, we chose to focus on these specific families. Currently, the CTX-M family is the most prevalent ESBL in both healthcare and nosocomial settings worldwide; making its presence nearly ubiquitous [49,50]. Furthermore, they have been found in numerous members of the family *Enterobacteriaceae* and confer resistance to several types of clinical infections. The only beta-lactams effective against these enzymes are carbapenems or beta-lactam inhibitor combinations [51]. Furthermore, these treatments are restricted by their limited pharmacokinetic effectiveness at certain infection sites and their susceptibility to mediators of resistance often carried along with CTX-M [51]. This makes treatment of infections with these enzymes extremely challenging. [49,52].

Until the early 1990's, ESBLs were generally regarded as the most concerning threat to healthcare. This has changed with the widespread arrival of carbapenem beta-lactamases and, for the United States, the KPC carbapenemases. KPC (specifically KPC-1) was first reported in a health-care setting in 1996 in a patient in North Carolina who had demonstrated resistance to all beta-lactams [53]. By the early 2000's, it had spread beyond isolated cases to outbreaks in New York City hospitals [54]. According to Centers for Disease Control and Prevention Data, this family has spread to all 50 states and is regularly observed in health care settings [55]. As a result, the KPC family poses a serious healthcare challenge in hospitals. Often bloodstream infections carrying KPC leave clinicians with very few treatment choices resulting in mortality rates as high as 50% [56,57].

1.7 Approaches to Understanding Beta-Lactamase Resistance

Antibiotics specifically designed to avoid beta-lactamase resistance could prolong drug efficacy and potentially evade future resistance. However, predicting mutations that change function and subsequently resistance is challenging in beta-lactamases [58]. Often, mutations beyond the binding-pocket can alter the resistance and kinetics of beta-lactamases [59–63]. As a result, allosteric mutations need to be considered when predicting mutations that alter resistance (Figure 1.4). Typical approaches, especially structural, informatics, and directed evolution, have some success but have faced challenges in predicting mutations that might affect function. Approaches that model physical changes from allosteric mutations to the binding-pocket could augment existing methods.

A common approach to understand allosteric mutations in enzymes involves experimental structural characterization of mutants. This method is successful with binding-pocket mutations and has characterized the effect of some beta-lactamase mutations [64–66] but can be difficult to apply to beta-lactamases due to subtle changes from allosteric mutations. Typically, through these analyses, such as crystallography, changes from allosteric mutations to the pocket are visualized by comparing wild-type and mutant structures. This allows for development of a potential mechanism to explain the effect of mutations. This mechanism can further serve as a model to predict other important mutations [67–69]. However, these methods work best with mutations that grossly affect structure or demonstrate a clear pattern in the location of mutations. In beta-lactamases, the mutations that affect function come from small changes that do not grossly alter the structure [24,70] and are diffusely located throughout the enzyme (Figure 1.4). This makes such gross structural approaches in beta-lactamase mutation prediction less useful for understanding subtler allosteric mutations.

Informatics based analytical approaches can often predict these subtle mutations, but the evolutionary history of beta-lactamases complicates such approaches. Most beta-lactamase families entered healthcare from pre-existing environmental enzymes that were suited to breakdown clinical antibiotics. Unlike other enzymes which co-evolved with their current substrates [71–73], clinical beta-lactamases gradually evolved to hydrolyze antibiotics in their environmental niche and then were recently and suddenly selected to hydrolyze a novel clinical beta-lactam [74,75]. This means that the development of a family's current beta-lactam class spectrum may be coincidental since there was little co-evolution with synthetic clinical beta-lactams [76–78]. Furthermore, it means that beta-lactam families demonstrate close intrafamily similarity but large interfamily differences in spectrum and sequence. Specifically between families of class A beta-lactamases, there are often sequence dissimilarities close to 50% [78]. For instance, a genetic study of CTX-M suggests that they transferred into healthcare pathogens from the gastrointestinal saprophyte *Kluyvera* and are phylogenetically different (diverging well over 200-300 million years ago) from previously identified beta-lactamases including ESBLs such as TEM-1 [76,79] .

The resulting sequence pattern and diverse evolutionary history of beta-lactamases complicates informatics-based methods. These approaches leverage the inherent patterns in the evolution of an enzyme by analyzing changes across sequences at residues sites based on residue-to-residue contacts, enzyme function, or structural mapping [80–82]. Beta-lactamase families demonstrate wide differences in many informatics based measures and characterization of these features in past studies found that patterns related to evolutionary history more than spectrum [24,70]. While challenging, these analyses have suggested mutations that might affect spectrum and function. These findings are typically mutations near the more conserved binding-pocket, an

area where variability might be more closely linked to spectrum. The evolutionary diversity makes identifying allosteric mutations that contribute to changes in spectrum as compared to other evolutionary noise much more challenging.

Due to the difficulty of developing sequence based models to predict resistance, some researchers have employed directed evolution-based approaches to identify adaptive allosteric mutations that alter spectrum but these studies require extensive prior knowledge of the evolutionary landscape and mutagenic potential of an enzyme. This form of protein engineering involves an iterative process of random mutagenesis followed by an increasingly stringent selection step. For beta-lactamases, this selection step would involve selecting mutants which increase resistance to an antibiotic. This approach is a Darwinian incremental random exploration of mutations and has the benefit of functionally validating any predicted mutation. Past work demonstrates successful directed evolutionary approaches applied to class A and class D (another serine mediated class) beta-lactamases that resulted in an altered antibiotic spectrum, but this method does face challenges in predicting and characterizing the effect of allosteric mutations on function [83,84]. Often directed evolution targets particular regions in the enzyme being studied. This makes a general purpose "off the shelf" method using directed evolution for mutation prediction more difficult [83,84]. Furthermore, class A beta-lactamase mutations demonstrate sign epistasis where, alone, a mutation lowers resistance but increases resistance when paired with another. As a result, this causes uneven sampling of the mutational space in incremental directed evolution as mutational sets which do not demonstrate sign epistasis have a much higher probability of forming in later iterations than those that do demonstrate it [85].

Modeling the direct effect of a mutation on the chemistry of the binding-pocket can augment existing approaches to understand functions and mechanisms that support beta-lactamase

function. First, studies have noted that beta-lactamases share overall structural and functional similarities of the binding-pocket environment even if they globally differ in sequence [70]. Therefore, studying differences in the physical chemistry of the bonding pockets between beta-lactamases with very different sequences and spectrum could identify interactions responsible for spectrum. Second, such a method inherently provides detailed information as to how a mutation affects the pocket. If sequence-based and evolutionary approaches identify a mutation that might affect spectrum, follow up biochemical studies would be needed to understand how that mutation alters chemical function. With a modeling approach, the same approach that discovered the mutation would include this information. One specific modeling approach to accomplish this involves the use of molecular dynamics simulations.

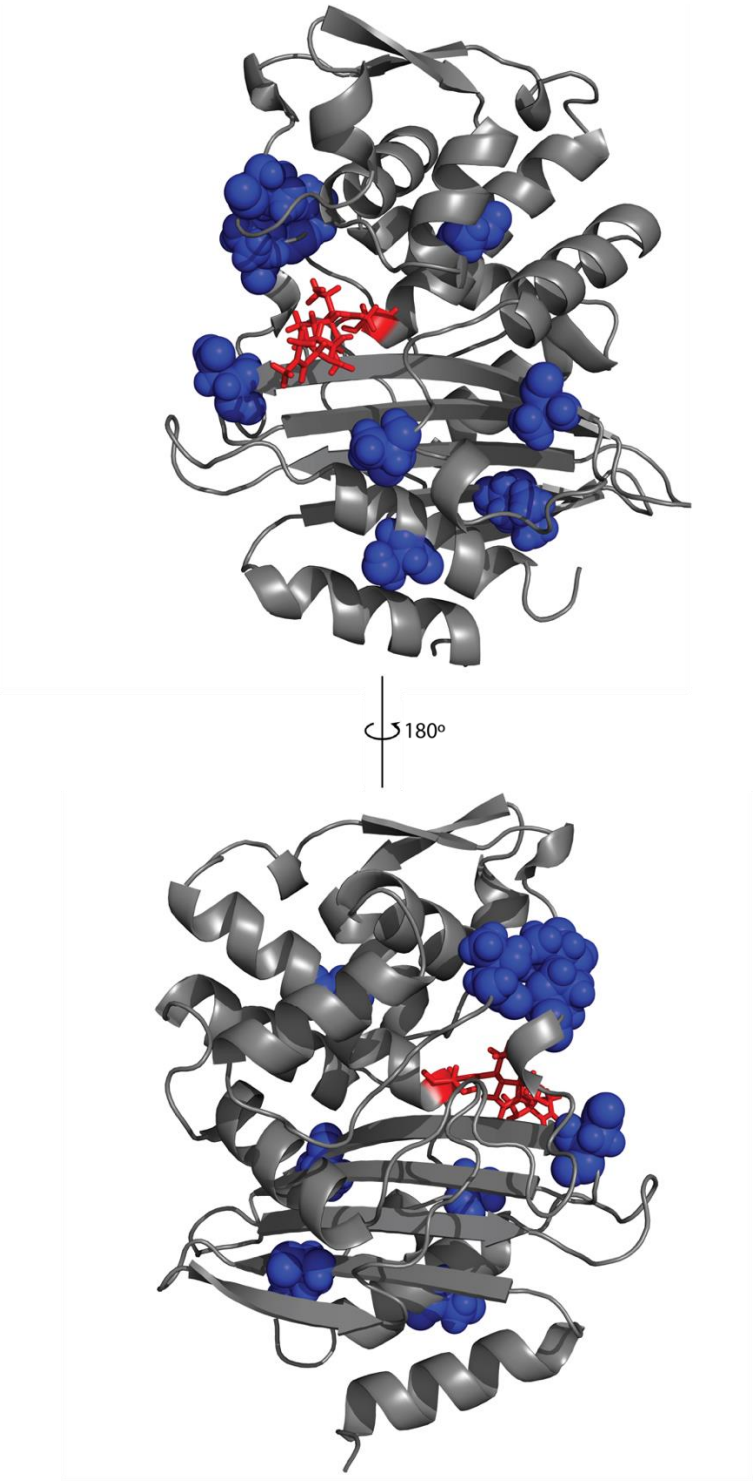

Figure 1.4 Identified allosteric mutations in the CTX family that affect function
Illustration of allosteric mutations that alter enzyme activity mapped onto CTX-M9's crystal structure (PDB 2P74), a CTX-M enzyme [37,59–63]. The binding-pocket is identified by the drug in sticks (red). Allosteric mutations demonstrate no clear structurally related pattern to aid prediction.

1.8 Molecular Dynamics Approaches to Beta-Lactamases

Molecular dynamics offers a means to relate changes in conformations in the binding-pocket to changes in spectrum and function. This approach models aspects of binding-pocket chemistry allowing for the characterization of interactions in the binding-pocket across beta-lactamase families and the screening of mutations that potentially affect spectrum and function. Molecular dynamics offer insight into the motion of atoms and therefore, molecules and proteins, as a function of time. They permit the study of the movement of enzymes beyond often non-biologically relevant conformations provided by crystal structures [86]. Molecular dynamic simulations model the forces exerted across atoms. These forces are obtained from defined force field equations deduced from atom type and molecular structure. Bonded interactions are modeled using spring potentials tuned for length and bond strength. Coulomb's law is often used for non-contact interactions [87]. These forces are then converted into acceleration and velocity using Newton's laws, which ultimately allows for the structure-based animation of protein conformations [87]. As a result, molecular dynamics simulations provide a unique spatial and temporal resolution that allows for the study of interactions that were previously impossible to observe [87]. These simulations have been very useful in studying enzymes. Specific to serine-based enzymes, past works have used these simulations to understand aspects of enzyme binding-pockets and the effect of allosteric mutations [88–91].

To date, this approach has been underutilized in studying the beta-lactam spectrum of beta-lactamases. Past work applying molecular dynamics simulations to beta-lactamases has focused on docking and binding, which often occur irrespective of antibiotic spectrum in these enzymes. These studies have attempted to describe conformational changes in the binding-pocket in relation to the ligand [64,89]. The work that has been performed on identifying potential allosteric effects

identified cryptic allosteric binding sites that could be potential drug targets. This demonstrates that molecular dynamics can identify allosteric effects in these enzymes [89,92,93]. Here, I aim to use molecular dynamics to study the binding-pocket conformations related to the acyl-enzyme state. These simulations provide a conduit to study the drug-enzyme interaction in the binding-pocket prior to the critical deacylation step. Additionally, they offer a method to measure potential effects of allosteric mutations on this chemistry. I specifically am interested in findings that are general enough to be applied across families.

1.9 Goals of this Dissertation

Class A beta-lactamases have large sequence diversity, but chemical and structural similarity in the binding-pocket. This has made traditional mutational approaches to understand the beta-lactam spectrum of these enzymes very challenging. The goals of this dissertation are to characterize residues and interactions that alter beta-lactam spectrum in two clinically important beta-lactamases and, in the process, develop approaches which can be further applied to other beta-lactamase systems. These approaches leverage the chemical similarity of the binding-pocket between beta-lactamases with different spectrums and dissimilar sequences to identify mutations and interactions that drive differences in function and drug spectrum. I present three works that apply molecular dynamics-based predictive study of mutations that potentially affect function, which are then experimentally verified. One challenge of molecular dynamic simulations is that identifying these interactions often involves finding patterns in noisy high dimensional data [94]. Therefore, much of this work offers new methods to find relationships in these simulations, which can translate to other beta-lactamase and potentially enzyme systems.

I begin by identifying residues that are essential for the function of CTX-M9, a member of the CTX-M family (Chapter 2). Next, I identify residues that modulate activity based on predicted

changes to binding-pocket interactions in CTX-M9 (Chapter 3) and translate these chemical findings to a different beta-lactamase family, KPC, with KPC-2 (Chapter 4). Finally, in the discussion and future directions, I close with the proposal of new techniques that would refine these approaches in the field.

Chapter 2. Excess Positional Mutual Information Predicts both Local and Allosteric Mutations Affecting Beta-lactamase Drug Resistance

2.1 Chapter Foreword

Enzymes function as catalysts by assuming active site conformations that reduce the free energy barrier for a chemical reaction either by enforcing specific substrate geometry or by creating a specialized local environment [95,96]. Allostery affects enzyme activity through the communication of positional fluctuations at a site distant from the active site to alter the conformations of the active site [97–99]. In this chapter, we have predicted and verified, using molecular dynamics simulations, allosteric residues that alter CTX-M9's function. Often allosteric effects do not occur through a simple series of interactions from that site to the pocket but more through a diffuse set of interactions [98]. Therefore, we employ a mutual information based method which focuses on the existence and strength of association regardless of how that communication is conveyed. The result helps identify allosteric residues on CTX-M9 and serves as a potential tool for the study of other beta-lactamases. Our work was published in *Bioinformatics* in July 2016 with me as first-author [62]. The text and figures have been adapted for this chapter with permission by and in accordance to the author rights stated by Oxford Journals. It is for non-commercial use.

2.2 Introduction

Although the key catalytic residues in CTX-M enzymes are well known, we wish to understand the basis for modulation of activity and ligand specificity in these enzymes. Even though comprehensive mutagenesis of CTX-M has not yet been experimentally feasible, reports of individual mutations show that single point mutations can alter drug spectrum and catalytic

activity [100–104]. Such point mutants have been identified in clinical isolates of bacteria [60,61,105,106] as well as laboratory mutagenesis experiments [100–104].

A comprehensive experimental understanding of how mutations affect beta-lactamase drug resistance has been hindered by the combinatorial magnitude of the problem. Even for point mutations on CTX-M enzymes alone, rigorous quantitation of how mutants affect activity against a large panel of drugs is extremely resource-intensive, entailing the screening of ~5000 mutants (260 residues x 19 amino acid changes) against multiple antibiotics. Therefore, we wish to identify residues that may contribute to activity and specificity but are not absolutely essential to function. Prediction of such residues can guide a more targeted set of mutagenesis experiments. In designing such an approach, we wish to consider all residues in the protein, not simply those in direct contact with the drug or previously identified via serendipitous mutations.

We have chosen to predict residues modulating antibiotic resistance in CTX-M enzymes based on analysis of molecular dynamics (MD) simulations. We hypothesize that the conformational dynamics of the enzyme and its substrate will yield insight into catalytic activity even though we do not consider catalysis explicitly in classical molecular dynamics simulations, unlike reactive methods [107–109]. Classical MD simulations have been previously used to predict or explain mutations in a number of enzyme systems [110–112].

To predict individual residues to mutate, we seek to identify the influence of individual atoms on catalytic activity rather than overall conformational substates of the enzyme. Molecular dynamics simulations provide a means to quantify this “influence” by measuring positional relatedness between protein atoms and a bound drug, based on the hypothesis that the conformation and orientation of the drug and its environment are related to catalytic activity. We sample

conformations from molecular dynamics simulations, which estimate a Boltzmann-weighted ensemble.

Positional mutual information provides a robust nonlinear metric to quantify relatedness of positional displacement in molecular dynamics simulations [113,114]. Normalized covariance matrices have also been used for such measurements [115,116], but such approaches are restricted by a linear correlation approximation [117,118], which is less desirable for detecting subtle yet important motions. Mutual information quantifies how much knowledge of the probability distribution of positional displacement for one atom *i* affects the distribution for another atom *j* and thus provides a much more general means of detecting relatedness.

Although positional mutual information has been used to analyze large-scale movements in a manner analogous to principal components analysis [118,119], here we desire a more focused approach. To predict residues important to catalytic activity, we score by mutual information to drug conformation. This is corrected for bulk protein movement, yielding excess mutual information

$$I(i, drug) - I(i, protein\_background), \quad (1)$$

where *I(i,j)* denotes the mutual information between residues *i* and *j* [114]. Such a metric encapsulates the precise question "how related is movement of atom *i* to the drug conformation". This metric is designed to identify functionally important residues that meet this criterion; it is of course not designed to detect residues that might not be motionally correlated with the drug but still important to catalysis.

Simulations and analysis were performed on the CTX-M9 beta-lactamase in complex with one of two antibiotics: cefotaxime and meropenem (Figure 2.1). CTX-M enzymes hydrolyze antibiotics by way of an acyl-enzyme intermediate where the antibiotic is covalently bound to the

enzyme [120]. CTX-M9 is able to efficiently hydrolyze cefotaxime, whereas it only forms the acyl intermediate for meropenem without completing hydrolysis [120]. The conformational dynamics of this intermediate may thus yield insight into the residues important

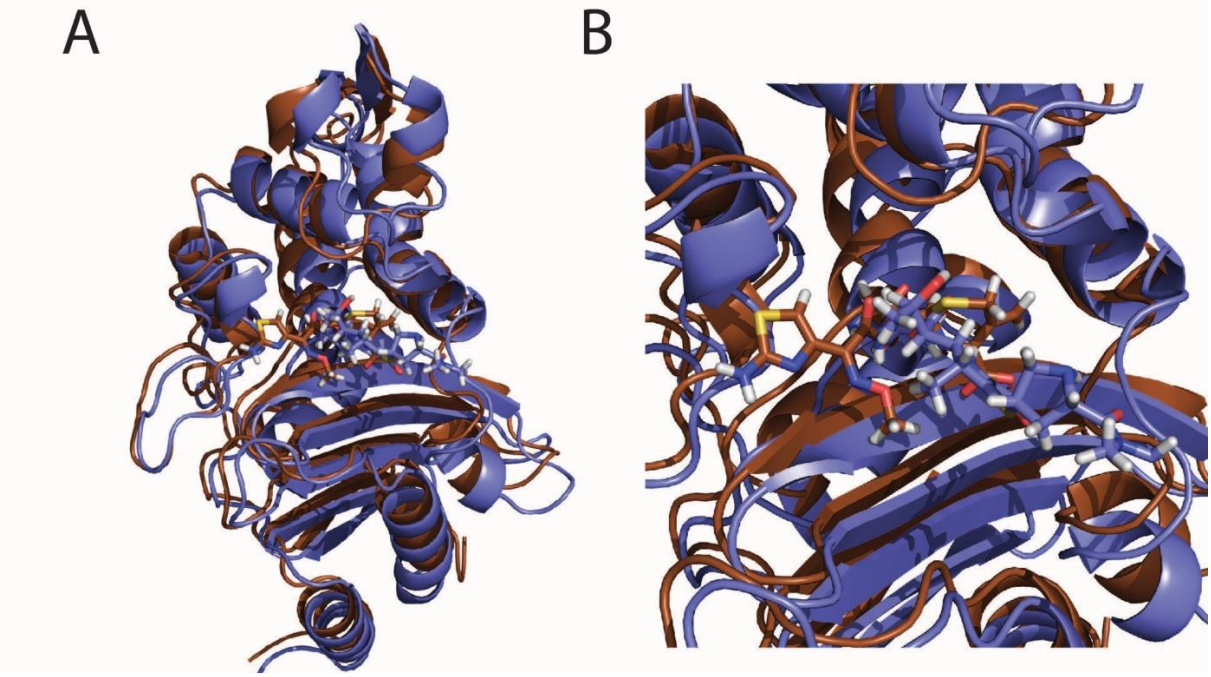

Figure 2.1 Structures of CTX-M9:drug complexes.
The overlaid structures of CTX-M9 acylated to meropenem (brown) and cefotaxime (violet) are rendered in panel (a) with a close-up of the drug-binding-pocket in panel (b). Protein is rendered in cartoon form and drug in sticks. These structures were used for molecular dynamics simulations that served as the basis for positional mutual information calculations.

for hydrolytic specificity in these enzymes. The positional mutual information matrices for both CTX-M9:meropenem and CTX-M9:cefotaxime complexes yield important insight regarding the organization of these enzymes. We then score residues that may affect catalytic activity of CTX-M9 using excess mutual information. These predictions yield a set of residues that have previously been identified as affecting catalytic activity and a set of novel, previously untested predictions. To validate our predictions, we tested the top-scoring residues for CTX-M9:meropenem and CTX-M9:cefotaxime via alanine mutagenesis, a common means to assess the effect of ablating a residue side chain. Six of these eight mutants had a >2-fold decrease in cefotaxime resistance while only one of the four lowest scoring residues for CTX-M9:meropenem and CTX-M9:cefotaxime similarly decreased resistance.

2.3 Methods

2.3.1 Molecular dynamics simulations

We obtained the *apo* crystal structure of CTX-M9 from the Protein Data Bank (PDB Code 2P74) [37]. The acylated meropenem structure was generated by least-squares RMSD fitting of the acyl-meropenem intermediate of SHV-1 (PDB Code 2ZD8) [121] with missing atoms added via rigid-body fitting. The acylated CTX-M9:cefotaxime structure was generated via least squares rigid-body alignment of all common atoms on the beta lactam ring of meropenem and cefotaxime on a Thr71Ser CTX-M9 mutant. Meropenem and cefotaxime were parameterized using the Amber Antechamber program with AM1-BCC partial charges [122]. All simulations were run using Gromacs 4.5 with the AMBER99SB-ILDN force field and TIP3P explicit water [123–125] in a periodic octahedral box with a minimum periodic image separation of 2 nm. The solvent consisted of approximately 24,000 water molecules and 150 mM NaCl. Simulations were run with a 2 fs

time step and hydrogen bonds were constrained using LINCS [126]. The temperature was maintained at 37 C using a velocity-rescaling thermostat [127] and the pressure was maintained at 1 bar with a coupling constant of 10 ps. Short-range nonbonded and electrostatic interactions were truncated at 1.2 nm, and long-range electrostatics were treated with Particle Mesh Ewald [128]. CTX-M9:meropenem simulations were then run using the Folding@Home platform, and CTX-M9:cefotaxime simulations were run on a Cray XC30 or on NVidia GPGPUs. 200 independent simulations were run of CTX-M9:meropenem complexes; 22 of these were randomly selected for subsampled analysis, totaling 2460 ns with a median simulation length of 106 ns. The first 46 ns of each simulation were discarded and the remaining aggregate 2150 ns used for analysis. Three longer independent simulations CTX-M9:cefotaxime complexes were analyzed; two simulations had lengths of 954 ns and one of 289 ns, after truncation, totaling 2197 ns. Snapshots were recorded every 50 ps.

2.3.2 Mutual information analysis of CTX-M9 dynamics

We calculated displacements for all atoms of the CTX-M9:drug complex after rigid-body alignment of the binding-pocket to the starting structure of each respective simulation. For this purpose, the binding-pocket was defined as residues having at least one non-hydrogen atom within 1 nm of the acylated drug carbonyl in >90% of simulation snapshots and where the root-mean-squared positional fluctuation of the backbone atoms was < 7 Å. Alignment using the binding-pocket as a reference was chosen to minimize artifactual drug motion from alignment error; a comparison where alignment was performed on the whole protein and yields similar results. These displacements $d_i(t)$ where i is the index of each atom and t is the time from the initial alignment structure were then used to calculate mutual information and symmetric uncertainty in a fashion

similar to that which we have reported previously [114]. Mutual information $I(i,j)$ was calculated between two atoms i, j using

$$I(i,j) = H(i) - H(i|j) = \quad (2)$$

$$-\sum_{i,j} P_{i,j}(x,y)\, log \frac{P_{i,j}(x,y)}{P_i(x)P_j(y)} \quad (3)$$

The probability density function $P_i(x)$ and $P_j(x)$ were estimated using 2-D histograms of $d_i(t)$ and $d_j(t)$ with 32 bins at even intervals min($d_i(t)$,$\forall t$) to max($d_i(t)$,$\forall t$) and min($d_j(t)$,$\forall t$) to max($d_j(t)$,$\forall t$).

Mutual information values were then normalized using symmetric uncertainty, which represents the relatedness of a pair of atoms independent of the motion undergone by each atom

$$S(i,j) = \frac{I(i,j)}{I(i,i)+I(j,j)} \quad (4)$$

Excess mutual information was calculated for each atom using

$$E(i) = \overline{S(\imath,k)} - \overline{S(\imath,l)} \quad (5)$$

where *k* are atoms in the beta-lactam ring of the drug (C6, C7, C8, N10, and O9 for cefotaxime and C5, C6, C7, N4, and O71 for meropenem) and *l* are all atoms not in the binding-pocket defined as above.

2.3.3 Sequence retrieval and processing

CTX-M family nucleotide sequences were retrieved using published accession numbers [49]. These sequences were then translated and individually aligned to a protein sequence of CTX-M9 (ACR66304.1) using TBLASTN [74,129]. Resulting sequences were aligned using MUSCLE [130]. From this alignment, a consensus sequence was generated for all residues identical across the CTX-M9 family to identify conserved residues.

2.3.4 Creation and resistance measurements of mutants

We performed site-directed alanine mutagenesis on selected residues in CTX-M9 [131]. Mutants were tested for cefotaxime resistance using a Kirby-Bauer antibiotic disc assay [132]. Bacteria were grown to an optical density of 0.1 and then evenly spread on Mueller Hinton agar plates with a cefotaxime antibiotic disc placed in the center. The diameter of clearance was measured after 12-16 hours of incubation. Resistance was measured as fold-change in apparent inhibitory concentration, calculated as the squared diameter of clearance for CTX wild-type divided by the square of the diameter of the mutant.

2.4 Results

We used positional mutual information to analyze the conformational dynamics of CTX-M9 with a bound antibiotic, either cefotaxime or meropenem, based on molecular dynamics simulations. Multiple microsecond-length simulations were used to obtain good statistical sampling of positional motions of the enzyme-drug complex. Mutual information provides a nonlinear analogue to measuring correlated motions. This approach identifies pairs and networks of atoms that are dynamically related and thus statistically interact either directly or indirectly. When applied to the active site of an enzyme, it thus enables a unified analysis of short-range and long-range interactions that may influence catalysis and in this case drug resistance. Furthermore, by measuring the excess mutual information of protein atoms to the drug compared to the rest of the protein, we identified residues that may influence the dynamics of the bound beta lactam ring and potentially subsequent drug hydrolysis.

2.4.1 Pairwise symmetric uncertainty to analyze positional relationships in CTX-M9

To quantify pairwise relationships between all pairs of atoms in the CTX-M9:drug complex, we calculated a positional symmetric uncertainty matrix based on molecular dynamics simulation trajectories. Symmetric uncertainty was used as a normalized information-theoretic metric of positional relatedness (calculated by dividing mutual information by the sum of entropies, see Methods for details). For cefotaxime, this yields a 3977x3977 matrix. Because the size of this matrix is N^2 in the number of atoms, we selected the top 0.25% of interactions (5% squared) for analysis or the top 19,771 pairs. Similarly, symmetric uncertainty analysis of CTX-M9:meropenem yielded a 3992x3992 matrix where the top 19,920 pairs comprise the top 0.25% of interactions.

At a coarse level, the resulting symmetric uncertainty matrices show, as expected, strong relationships between directly interacting atoms as well as stabilization of secondary structure elements. Thresholded matrices for CTX-M9:cefotaxime and CTX-M9:meropenem complexes are plotted in Figure 2.2 and Figure 2.3, and the top-scoring interactions are rendered as dotted lines on the protein structure in Figure 2.2A and Figure 2.3A. This analysis yields statistically coupled yet spatially distant atom pairs as well as a number of strong interactions from directly contacting atoms, as discussed below. The strong near-diagonal band reflects the expected high symmetric uncertainty for atoms that are directly connected by bonded interactions; in addition, salt bridges and Van der Waals contacts between sequence-distant but spatially proximate atoms also resulted in pairs with high symmetric uncertainty. Secondary structural elements are typically strongly connected, except when such structures are so strongly stabilized that they are immobile over the multi-microsecond timescales sampled and thus have near-zero positional entropy. Also present in the high-scoring pairs are interactions between nearby secondary structural elements. For

example, in the CTX-M9:cefotaxime simulations, a number of high-scoring pairs were measured between the alpha helix containing residues Ala28-Ser40 (Fig. 2A, atom indices 45-243) and the helix containing residues Arg276-Ala287 (atom indices 3752-3953).

One striking finding is the lack of strong relationships between the bound drug and the major catalytic residues and similarly between the drug-binding-pocket and the rest of the enzyme in both sets of simulations. The highest-scoring drug-protein symmetric uncertainty value occurs below our 99.75% statistical cutoff, and such linkages remain sparse even at much lower cutoffs (Figure 2.2D and Figure 2.3D). This suggests that the drug and catalytic geometry are relatively isolated from conformational fluctuations of the rest of the protein. Such a finding makes sense in light of theories of catalytic preorganization in enzymes, which can be interpreted to state that optimal catalytic efficiency results from minimal fluctuations of the catalytic residues [133,134]. This is well supported by crystallographic studies of CTX-M9 alone and in complex with different transition-state analogues; in one such series of structures, key catalytic residues such as Ser130, Lys73, Glu166, and Ser237 shift only an average of 0.1 Å over a set of substrate analogues spanning the catalytic cycle [120]. Despite this relative isolation, symmetric uncertainty analysis of CTX-M9:cefotaxime yielded one potentially important network involving Asn104, Arg276, and Asn170. This network is connected by linkages at the 99.5^{th} percentile, below our statistical cutoff, but stronger than any other networks of spatially distant residues. Although none of these residues is directly involved in catalysis, previous work has suggested they have a strong role in function. Asn170 is believed to be involved in establishing the hydrogen bond network [135] with the catalytic water molecule while Asn104 directly interacts with acylamide side chain of cefotaxime [136]. None of these interactions met the pre-defined threshold for significance in our analysis, but they constitute intriguing candidates for further testing.

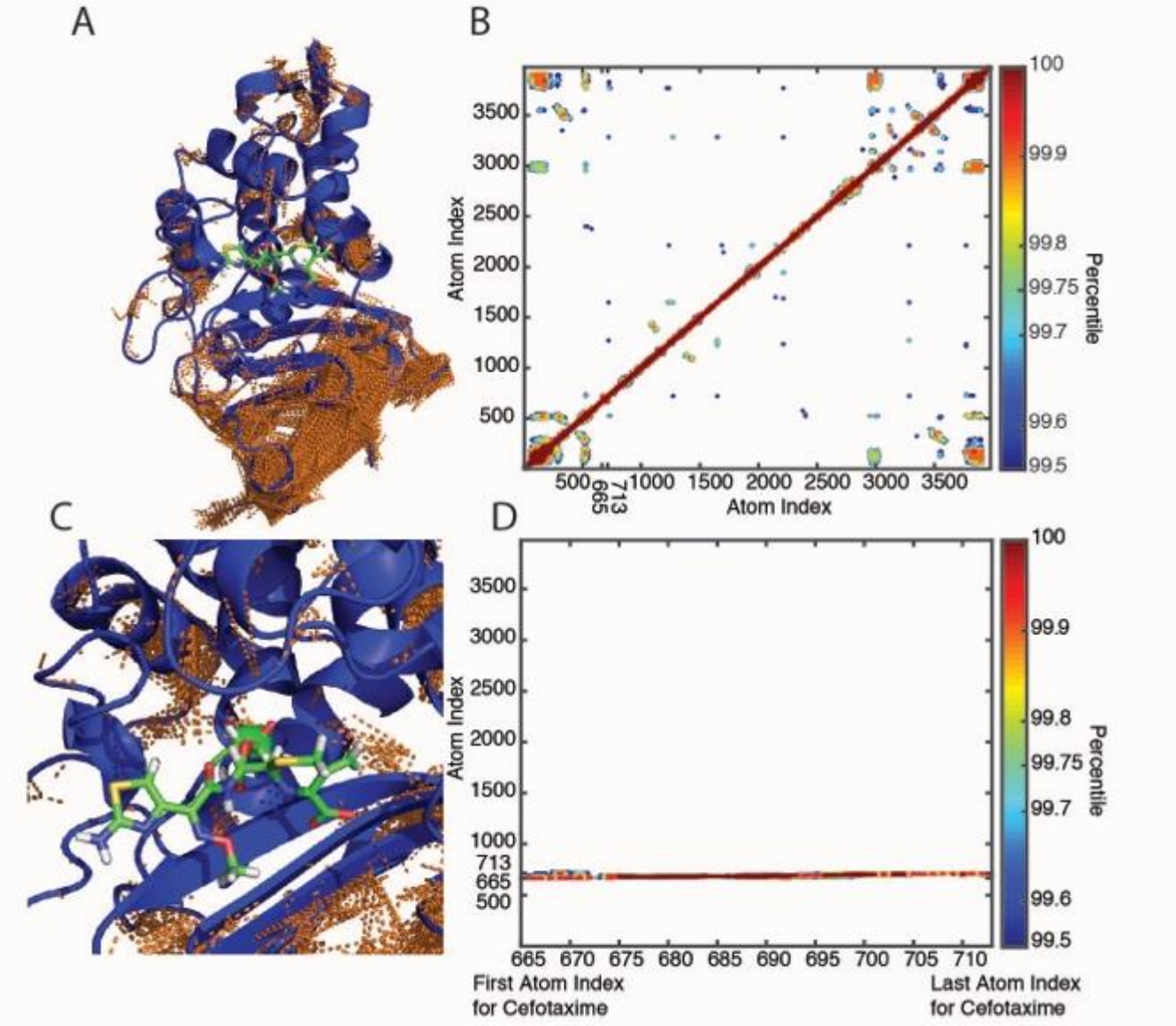

Figure 2.2 Pairwise positional symmetric uncertainty in CTX-M9:cefotaxime complexes. Symmetric uncertainty (normalized mutual information) is used to quantify the degree to which atom motions are associated. Rendered in panel (a) are the top 0.25% of symmetric uncertainty pairs shown as brown lines on the CTX-M9:cefotaxime structure. Panel (b) shows a contour plot of the atom-atom symmetric uncertainty matrix contoured at 0.1% intervals from the 99.5th to 100th percentiles. While numerous connections are identified between secondary structural elements, the drug has few high-ranking interactions with protein atoms, indicating a relative isolation of drug motion from protein motion. This is illustrated in the inset rendering in panel (c) and the portion of the symmetric uncertainty matrix corresponding to drug interactions in panel (d) that shows only self-interactions scoring above 99.5%.

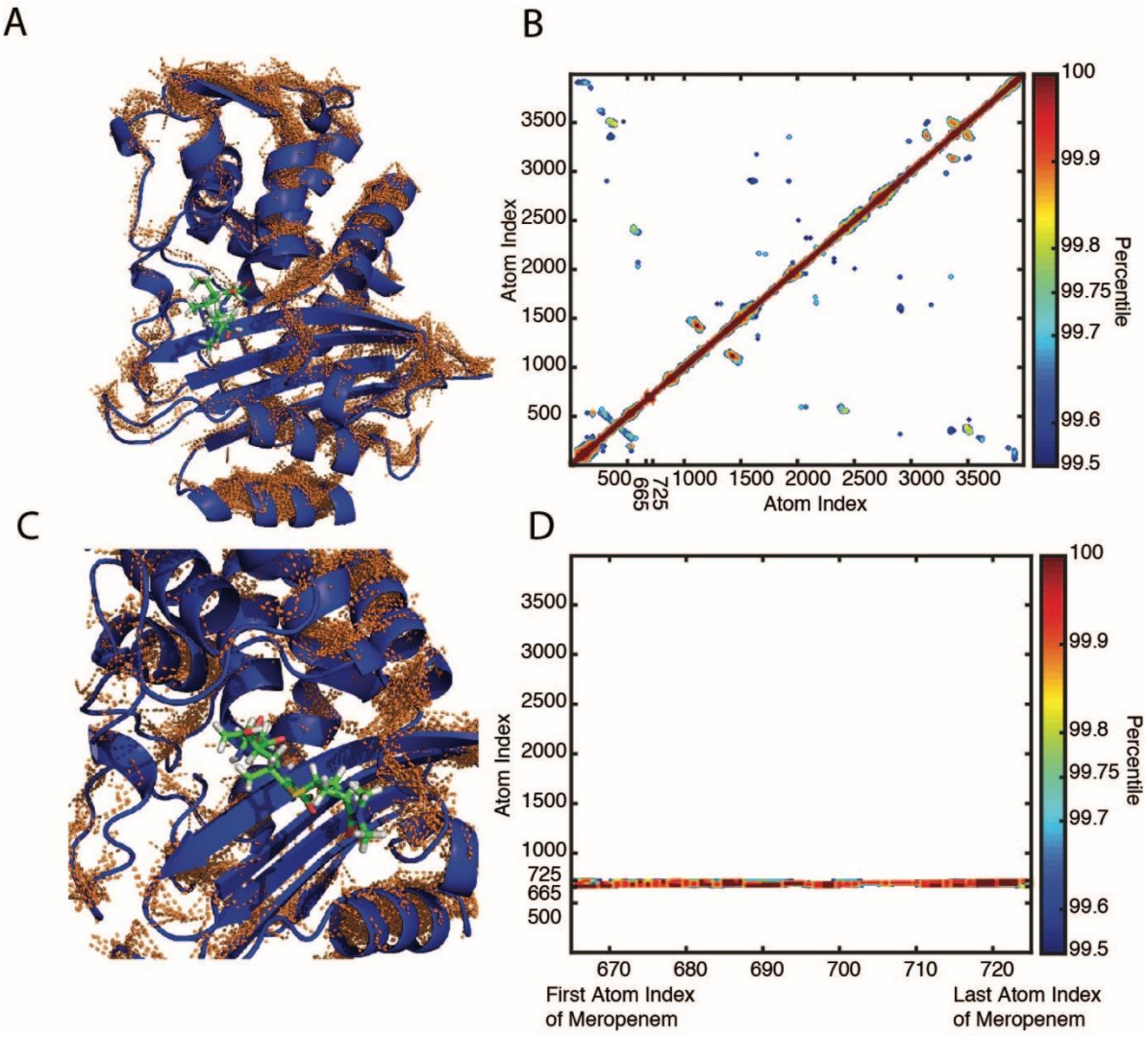

Figure 2.3 Pairwise positional symmetric uncertainty in CTX-M9:meropenem complexes. The top 0.25% of symmetric uncertainty pairs are rendered as brown lines on the protein structure in panel (a), with the matrix contoured at 0.1% intervals at 99.5% and above in panel (b) and insets showing drug interactions in panels (c) and (d). Similar to CTX-M9:cefotaxime, CTX-M9:meropenem simulations showed few interactions between the drug and enzyme or the drug-binding-pocket and the rest of the enzyme.

2.4.2 Excess mutual information identifies residues linked to drug motion

While symmetric uncertainty enables a global analysis of statistical interaction networks in the protein-drug complex, a more targeted statistical metric is desired to identify residues associated with particular motions of the bound drug. Excess mutual information quantifies drug-protein positional coupling in a fashion corrected for protein motions and capable of robustly identifying even weak but physically significant coupling. Excess mutual information measures the symmetric uncertainty between a protein atom and the beta-lactam ring but corrects for bulk protein motion by subtracting the average symmetric uncertainty to the rest of the protein (see Methods for details). The top 5% of protein atoms as scored via excess mutual information to the beta-lactam ring were then selected for both CTX-M9:cefotaxime and CTX-M9:meropenem (Table 2.1 and Figure 2.4).

Table 2.1 Top-scoring residues via positional excess mutual information

Rank	CTX-M9:cefotaxime	CTX-M9:meropenem
1	T235*[C]	T235*[C]
2	N132*	G236[C†]
3	T71*[C†]	T216
4	Y264[C]	T71*[C†]
5	N245*[C]	R276*[†]
6	D246*[C]	S130[C†]
7	N104*[C†]	A219*[C†]
8	Y234*	D246*[C]
9	I221[C]	Y234*
10	N106[†]	Y73*[C†]
11	R222	M68[C]
12	Y73*[C†]	N132*
13	D233[C]	A218*
14	Y105*[C]	C69[C]
15	V103*[†]	S237*[†]
16	S220[†]	N214*
17	A219*[C†]	L119
18	Y60	N245*[C]
19	A218*	A125
20	A263	N104*[C†]
21	Q128*[C]	E166[†]
22	D131*[C]	T133
23	V262[C]	V103*[†]
24	L225	Y105*[C]
25	N214*	G217
26	V46[C]	T215[C]
27	L33[C]	L127[C]
28	S237*[†]	Q128*[C]
29	A231	L102[C]
30	R276*[†]	D131*[C]
31	S72[C]	P167
32		E110[C]

*-Shared between CTX-M9:cefotaxime and CTX-M9:meropenem
C- Conserved residue
†-residue mutated experimentally; altered drug resistance observed

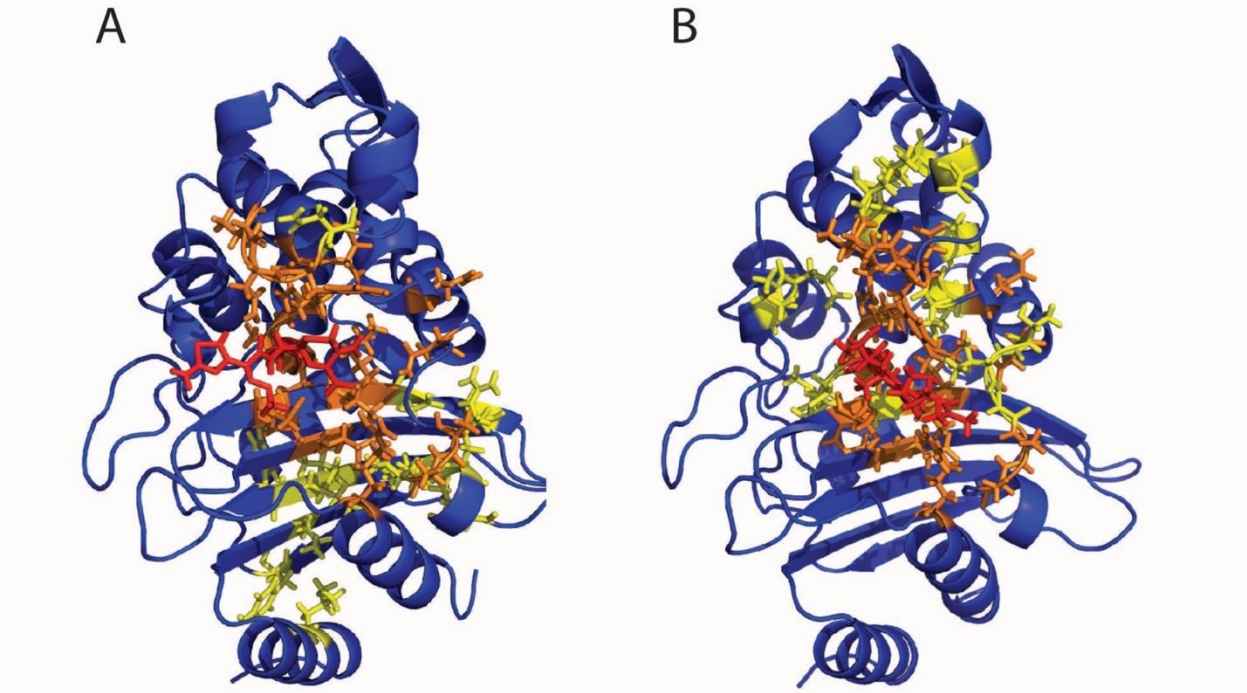

Figure 2.4 Residues linked to drug motion identified by excess positional mutual information. Residues corresponding to the top 5% of protein atoms scored by excess mutual information to the beta-lactam ring are rendered as sticks on the CTX-M9:cefotaxime structure in panel (a) and the CTX-M9:meropenem structure in panel (b). These residues constitute our predictions for sites where mutation will affect catalytic activity and drug resistance. The drug is shown in red, residues identified in both enzyme:drug complexes in orange, and residues identified in only one enzyme:drug complex in yellow.

These top-scoring atoms yield a prediction of functionally important residues for beta-lactam hydrolysis for CTX-M9. The top 5% of atoms scored by excess mutual information in CTX-M9:cefotaxime simulations covered 35 residues, 31 after removing "singleton" residues with only one atom selected (of 265 residues total).

Of these, 9 have previously been tested via mutagenesis experiments, and in all 9 mutations were confirmed to reduce catalytic activity, as assessed by a decrease in both k_{cat} and minimum inhibitory concentration of drug to impede bacterial growth [74,100,101,103,130,136]. In addition, 17 of the 31 residues are sequence-identical across the CTX-M family using the family definition provided in [49]. Of the 10 top-scoring residues, 7 are sequence-identical across CTX-M9, and 3 have been previously tested and confirmed via experimental mutagenesis. This degree of sequence conservation further, although indirectly, supports a functional role for the residues thus identified. Residues predicted by excess mutual information include amino acids both in the drug-binding-pocket and distant from it (allosteric mutations). This second category (including Leu33, Val45, Ala245, Ala263, and Tyr264) is particularly interesting, as they are more difficult to identify via conventional methods. Previous experimental mutagenesis has shown that allosteric mutations can affect hydrolysis of cephalosporins via beta-lactamase enzymes [101], and the prediction of novel allosteric mutations is a major goal of this work. Recent work based on evolutionary conservation has proposed distance to the active site as a means to score functional importance of enzymes [137]. In our data, excess mutual information scores showed correlation values of (0.27 and 0.56) with distance to the catalytic residues, explaining 7.6% and 31% of the variance in MI respectively, demonstrating that for this system excess mutual information contains information other than purely distance. In addition, high-scoring residues ranked moderately in positional mobility (top-

scoring residues in CTX-M9:cefotaxime simulations have root-mean-squared fluctuation of 1.4 to 1.9 Å compared to an overall range of 0.53 to 7.72 Å and median 1.6 Å.

Corresponding analysis of the CTX-M9:meropenem complex yielded a number of residues in common with CTX-M9:cefotaxime (Figure 2.4). The top 5% of atoms scored via excess mutual information mapped to 37 residues, 32 after singleton removal. Of these 32 residues, 17 were in common with CTX-M9:cefotaxime, and the remaining 15 diverged. Although it is tempting to analyze differential scoring between the CTX-M9:meropenem simulations and the CTX-M9:cefotaxime simulations as relating to the capacity of CTX-M9 to hydrolyze cefotaxime but not meropenem, we wish to remain conservative in this respect as the simulation sampling scheme differed slightly between CTX-M9:cefotaxime (fewer, longer simulations) and CTX-M9:meropenem (more simulations of 100-200ns in length), and we cannot exclude a sampling bias in accounting for the different residues identified. Common residues included several involved in catalysis either directly or indirectly such as Ser237, Arg276 [102,120]. Top-scoring residues from CTX-M9:meropenem (but not CTX-M9:cefotaxime) included Ser130 and Glu166, two residues closely tied to catalytic function (Glu166 is believed by many to be the general base for cephalosporin hydrolysis in CTX-M enzymes) [120,135,138]. The identification of these residues suggests that although CTX-M9 cannot fully hydrolyze meropenem, catalytic residues still interact with the drug in a coordinated manner.

2.4.3 Mutation at top-scoring sites decreases drug resistance

As an experimental test of our scoring method, we mutated each of the 5 top-scoring residues via excess mutual information singly to alanine. We used antibiotic resistance of transformed bacteria expressing each enzyme as a metric of enzymatic function. As a control, we also mutated the four lowest-scoring residues and four residues that scored closest to zero excess

mutual information (relationship to drug motion equal to the average across the protein). Of the top-scoring residues, 6/8 had a greater than two-fold reduction in cefotaxime antibiotic resistance (Figure 2.5), with all mutants showing some reduction in resistance. Four of the most affected top-scoring residues were located near the drug-binding-pocket while two were more distant from it, suggesting that excess mutual information can indeed identify both nearby and allosteric residues affecting function. Only one of the four lowest-scoring residues displayed a >2-fold reduction in cefotaxime antibiotic resistance (Figure 2.6C). Similarly, of the four mutants scoring near zero (background correlation only), none showed a >2-fold decrease in drug resistance (Figure 2.6C). These results demonstrate that excess mutual information can robustly identify ($p < 0.05$ via Fisher's exact test or $p < 0.01$ via two-tailed Kolmogorv-Smirnov test) residues likely to be involved in enzyme function and consequent drug resistance.

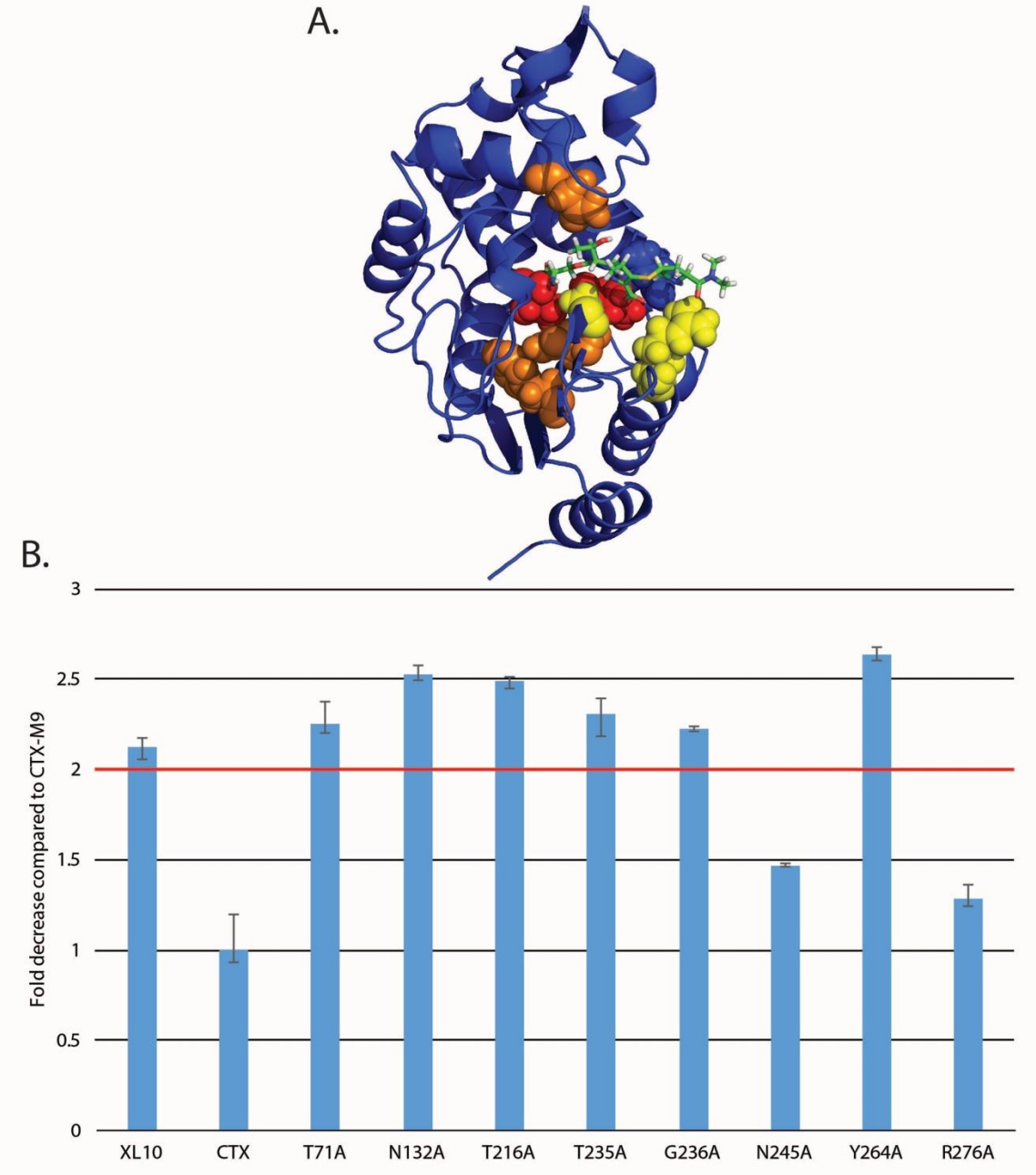

Figure 2.5 Mutation of top-ranking residues via positional mutual information greatly decreases cefotaxime drug resistance.
The five highest-scoring residues for cefotaxime (orange) and meropenem (yellow with residues in both sets as red) were selected for alanine mutagenesis. These were located both inside and distant from the drug pocket (a). Six of the eight mutants displayed a >2-fold drop in resistance.

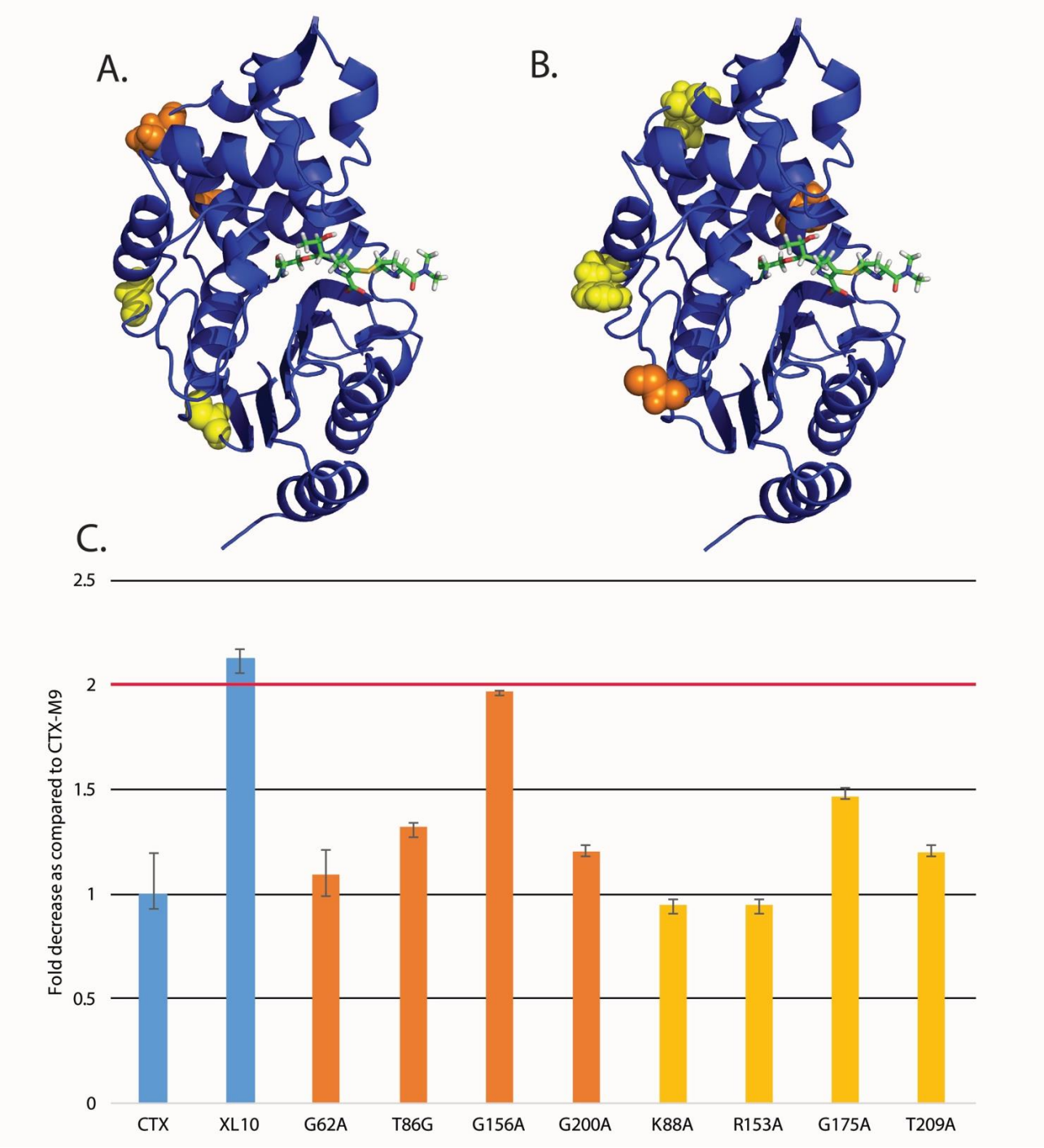

Figure 2.6 Mutation of lowest-scoring residues leaves cefotaxime drug resistance largely unaffected.

As rendered in panel (a), the lowest-scoring residues and (b) the residues with closest to background mutual information in cefotaxime simulations (orange) and meropenem simulations (yellow) were located outside the drug-binding-pocket. As plotted in panel (c), none of near-background mutants (yellow) and one of the lowest scoring mutants (orange) showed a >2-fold decrease in drug resistance.

2.5 Chapter Discussion

We have developed an excess mutual information metric to predict residues important for drug hydrolysis in the CTX-M9 beta-lactamase enzyme based on molecular dynamics simulations. We initially developed excess positional mutual information to score protein residues on the influenza hemagglutinin glycoprotein that influence low-affinity binding of sialoglycans [114]. Here, we show how excess mutual information can be used in a much more sensitive and targeted fashion, detecting motions of an enzyme that are weakly but significantly coupled to dynamics of a bound substrate, and prospectively predicting and testing mutants that affect enzyme function. This marks a substantial expansion on the scope of problems for which excess mutual information can predict mutational effects: from initial work on relatively "floppy" low-affinity ligand binding, it was not obvious that mutual information would successfully predict sites of mutation in a relatively rigid beta-lactamase enzyme. Although positional mutual information has been used very productively to identify conformational substates of a protein, use of excess mutual information allows a much more targeted measurement of how individual residues are related to ligand motion in a manner that is robust even in the presence of weak coupling. As we have shown, excess mutual information identifies residues where mutation alters k_{cat} even though these residues are not strongly related to ligand or binding-pocket motions in the full N^2 symmetric uncertainty matrix.

Our primary goal in developing excess mutual information is to obtain a metric that can predict both binding-pocket mutations and allosteric ones in a single integrated analysis. Since many structure-based approaches concentrate on the ligand-binding-pocket, our prediction of both proximate and distant residues demonstrates the power of such an approach. Another motivation for the use of positional excess mutual information is that it provides an empirical measurement

of positional relatedness that can be complementary to mutational analysis [114] yet leverages state-of-the-art classical molecular dynamics force fields for both force calculation and sampling of statistical ensembles of conformations. In contrast to methods that compute energy-based coupling of protein residues, analyses of molecular dynamics trajectories naturally incorporate entropic terms and yield a free-energy-based coupling of protein residue motions.

Our analysis identified several previously untested mutations predicted to alter the catalytic activity and drug resistance conferred by CTX-M9. We tested a set of these prospective predictions utilizing bacterial drug resistance as a measure of enzyme function, comparing to low-scoring mutations. The predicted high-scoring mutations had a much greater effect on enzyme function than mid-scoring or low-scoring controls (6/8 showing a >2-fold drop in resistance vs. 1/8 in the aggregate control groups; $p < 0.01$ via KS test). Furthermore, these mutations that alter drug resistance are located both within and outside the drug-binding-pocket, with high-scoring mutations as far as 24 Å away, meeting our design criteria of a single global analysis to identify both local and allosteric mutants. The ability to anticipate altered drug-resistance of new variants is of great utility for clinical surveillance of CTX-M beta-lactamase s as well as drug development efforts.

Chapter 3. Predicting allosteric mutants that increase activity of a major antibiotic resistance enzyme

3.1 Chapter Foreword

As discussed in Chapter 2, allosteric residues affect beta-lactamase function. These sites are hard to predict using traditional structural techniques as they can affect important conformations not well sampled with crystallography. We have used molecular dynamics simulations to predict allosteric mutants increasing CTX-M9 drug resistance and experimentally tested top mutants using multiple antibiotics. Purified enzymes show an increase in catalytic rate and efficiency, while mutant crystal structures show no detectable changes from wild-type CTX-M9. We hypothesize that increased drug resistance results from changes in the conformational ensemble of an acyl-intermediate in hydrolysis. Machine-learning analyses on the three top mutants identify changes to the binding-pocket conformational ensemble by which these allosteric mutations transmit their effect. These findings show how molecular simulation can predict how allosteric mutations alter active-site conformational equilibria to increase catalytic rates and thus resistance against common clinically used antibiotics. Furthermore, this offers a screening approach that could be transferred to understand other beta-lactamases.

The work described here was published in *Chemical Science* with the co-first authors Malgorzata Latałło, M.Sc., and George Cortina [63]. Ms. Latałło performed much of the wet lab work and analysis especially kinetics and crystallization. I performed some experiments and the simulation work and conformational analysis. The text has been modified for non-commercial use in accordance to the author re-use permissions.

3.2 Chapter Introduction

Here we are concerned with new point mutations that increase the drug resistance of CTX-M beta-lactamases. Such point mutations have been observed clinically, and a number have been characterized mechanistically [100,139–143]. However, the landscape of mutations affecting drug resistance remains incompletely characterized due to the large combinatorial space involved, and the mechanism for increased resistance by allosteric CTX-M mutants remains largely unknown. CTX-M is also an attractive system to study allosteric mutations because of the strong structural similarity across many class A beta-lactamases despite large differences in sequence, substrate profiles, and catalytic rates.

Antibiotic resistance by class A beta-lactamases proceeds via a two-step kinetic mechanism involving an acyl intermediate:

$$E + S \leftrightarrow ES \overset{k_{ac}}{\rightarrow} EI \overset{k_{dac}}{\rightarrow} EP \leftrightarrow E + P$$

where E denotes enzyme, S the drug substrate, EI the acyl intermediate, and P the hydrolyzed drug product. Previous studies have shown that either the acylation rate (k_{ac}) or the deacylation rate (k_{dac}) can be rate limiting depending on the enzyme variant or the drug substrate [144,145]. Due to this variation and the low 38% sequence identity between CTX-M9 and the better-studied TEM proteins, including a number of residues of functional significance [146], mechanistic studies of CTX-M proteins in particular are of clinical importance. Because CTX-M enzymes have been shown to arrest at the acyl intermediate (EI) in the hydrolysis of meropenem, we hypothesized that the conformational dynamics of the acyl-enzyme complex would be predictive of the hydrolysis of cephalosporin and carbapenem antibiotics.

Many approaches have been taken towards computational understanding of beta-lactamase function. Here, we desire to understand mutational changes that affect a chemically narrow but

clinically important substrate spectrum. We therefore undertook classical molecular dynamics simulation of the acyl-enzyme:drug covalent complex to predict how mutations, including those distant from the active site, would affect conformational dynamics of the drug and subsequent catalytic activity in the deacylation step of hydrolysis. Our focus on the acyl intermediate thus differs from other approaches to beta-lactamase function that have treated the apo and ligand-bound states [92,147]. We simulated 125 different point mutants of the CTX-M9 beta-lactamase, running >1000 simulations per mutant in order to improve estimation of these conformational changes. Measuring k_{cat} changes experimentally for this many randomly selected mutants is a substantial but feasible task; the main reasons to perform molecular simulation are to enable screening for an arbitrary specified set of mutants (not just point mutants) and to facilitate detailed explanation of how allosteric mutations might affect function.

Although it would be unexpected for a single point mutation to confer substantial meropenem hydrolytic capability onto a CTX-M enzyme, we simulated CTX-M9 in complex with meropenem as a demanding test of mutations increasing drug resistance. Mutants were scored by the probability of forming hydrogen bonds believed to stabilize the deacylation transition state (Figure 3.1), and 5 high-scoring mutants as well as 4 lower-scoring ones were expressed in bacteria and tested for cefotaxime and meropenem resistance. We selected three such mutants with substantially increased resistance for further mechanistic and structural testing. All three of these mutations were at allosteric sites: T165W on a loop near the active site and S281A and L48A > 20 Å away on the other side of the enzyme.

3.3 Methods

3.3.1 Constructs

A pET-9a plasmid containing *bla*CTX-M9 was the kind gift of Robert Bonomo (Bethel et al., 2011). The following point mutants were constructed, were sequence-confirmed and transformed into bacterial strains as specified below: L48A; A140K; T165W; T158E; A219H; S220R; and N271D, and S281A.

3.3.2 Molecular dynamics simulations

CTX-M9 and mutant enzymes were simulated in acyl-enzyme complexes with meropenem; wild-type enzyme and 3 top-scoring mutants were also simulated in complex with cefotaxime. Starting structures were constructed by least-squares fitting of a meropenem-SHV-1 acyl-enzyme structure [121] onto the CTX-M9 *apo* crystal structure of CTX-M9 (PDB codes 2P74) [37] . Each protein was placed in an octahedral box with 2 nm minimum periodic separation and solvated with TIP3P water and 150 mM NaCl. Simulations were run using Gromacs 4.5 [123] with the AMBER99SB-ILDN force field [125]. Parameters for meropenem and cefotaxime were determined using the AMBER Antechamber program using AM1-BCC partial charges [122,148]. Partial charges were obtained using Ser70 covalently bound to meropenem or cefotaxime respectively. Bonded and vdW parameters were used from AMBER99SB-ILDN where available and from GAFF [149] where not. Hydrogen bonds were constrained using LINCS, and short-range interactions were truncated at 1.2 nm. Long-range electrostatics were treated with Particle Mesh Ewald [128]. Simulations were run at 310K and 1 bar pressure using a velocity-rescaling thermostat [127] and the Berendsen barostat [150].

Simulations were run on two architectures: 200 simulations of CTX-M9:meropenem and 50 simulations of each of the 125 mutants tested were run on the Folding@Home platform. Additionally, 1000 simulations for each of the 125 point mutants of CTX-M9:meropenem were run using the Google Exacycle platform. Aggregate simulation averaged 5.75 microseconds per mutant for the Folding@Home simulations and 5.24 microseconds per mutant for the Exacycle simulations. Oxyanion hole scoring of mutants on these two datasets was not significantly different and is compared in Figure S2. Convergence analysis is provided in Figure S3; approximately 25 simulations averaging 57 ns each were required for a converged ranking of mutants. Three simulations of wild-type CTX-M9 in complex with cefotaxime were also run, totalling 2.5 microseconds, as well as 20 simulations of each of the CTX-M9 wild-type and the L48A, T165W, and S281A mutants of >80 ns each. Simulation snapshots were saved every 50 ps for analysis.

Simulations were scored by the probability of forming hydrogen bonds that would stabilize an oxyanion in the deacylation transition state (the "oxyanion hole"). Distances between the carbonyl oxygen on the acylated beta-lactam antibiotic and each of two hydrogen bond donors (backbone amide hydrogens on residues 237 and 70) were measured using 3 Å as a distance cutoff for hydrogen bond formation. All point mutant simulations were scored by the fraction of simulation snapshots satisfying both these hydrogen bonding criteria. Simulations were performed to create two independent data sets; scoring of these data sets was highly concordant, particularly for top mutants. Furthermore, simulations of cefotaxime acyl-enzymes ranked the three top experimental mutations in the same order as the meropenem acyl-enzyme simulations. CTX-M9 wild-type simulation snapshots never satisfied both hydrogen bonding criteria simultaneously in complex with meropenem, whereas separate simulations with cefotaxime satisfied the criteria in >90% of snapshots. Separate simulations of the carbapenemase KPC-2 in complex with

meropenem also frequently satisfied the hydrogen bonding criteria, leading us to conclude that these criteria may be a good predictor of deacylation activity.

Positional mutual information was calculated for simulations of CTX-M9 and the L48A, T165W, and S281A mutants in complex with meropenem and with cefotaxime in a manner similar to that described previously [62] except that here each simulation snapshot was rigid-body aligned to the CTX-M9 crystal structure using binding-pocket atoms, where the binding-pocket was defined as all residues having at least one non-hydrogen atom within 1 nm of the drug in >90% of wild-type simulation snapshots. The aligned distance of each binding-pocket atom to its reference position in the crystal structure was measured, and the probability density function was estimated by binning distances across all snapshots of a given mutant using a 1.5 Å bin width (top-10 rankings were identical for bin widths from 1.1 to 3.5 Å). Mutual information was calculated between the position of each binding-pocket atom and the corresponding protein sequence being simulated. The top 10 atoms were selected using this criterion and used to train a decision tree classifier using a Gini impurity criterion and "best split" strategy. Classification accuracy was tested using 10-fold cross-validation on the training set and separately on a randomly selected test set consisting of 20% of the original data set.

3.3.3 Drug resistance assays

Phenotypic testing was performed using MG1655 Omp C-/F- *E. coli* (gift of Linus Sandegren) transformed with each *bla*CTX-M9 mutant plasmid as indicated. Antibiotic susceptibility was tested using the Kirby-Bauer disc diffusion method [132,151,152]. Discs containing the following amounts of antibiotics were purchased from BD Medical (Franklin Lakes, New Jersey): meropenem (10 μg), cefotaxime (30 μg), ceftriaxome (30 μg), cefepime (30 μg), cefuroxime (30 μg), ceftazidime (30 μg), and fold-change measurements were calculated using

wild-type CTX-M9 tested with each batch as an internal control. Bacteria were grown to an OD_{600} of 0.1 in liquid broth and then evenly spread on Miller-Huntington agar plates, and the size of the inhibition zone was measured after 14-16 h of incubation at 37°C. Resistance was assessed as fold change of inhibitory concentration, calculated as the square diameter of clearance of wild-type CTX-M9 over square of the diameter of the mutant. Four samples were tested for each mutant-drug combination. Bacterial growth rates were determined by optical density (OD_{600}) measurements every 30 minutes at 37°C with continuous shaking at 220 rpm in LB liquid broth.

3.3.4 Additional methods

Details of enzyme purification, measurement of hydrolysis kinetics, thermostability assays, simulation preparation, and crystallization, X-ray diffraction, and refinement are given in Appendix A.

3.4 Results

We simulated 125 point mutants of the CTX-M9 beta-lactamase in complex with meropenem, using residues from the structurally similar but highly drug-resistant enzyme KPC-2 as a source of mutational diversity. Mutants were scored by probability of forming two key hydrogen bonds that stabilize the deacylation transition state. Nine of ten top-scoring mutants were identical whether hydrogen-bond length or both length and angle were used as scoring criteria. Five high-scoring mutants and several comparators were expressed in *E. coli* and tested for increased resistance to cefotaxime and meropenem compared to wild-type CTX-M9. The three top-scoring mutants identified by this procedure were then purified and characterized via crystallography, thermal stability, and steady-state kinetics to understand the mechanism of allosteric modulation of drug resistance by these mutants.

3.4.1 Prediction and testing of mutants

Point mutants of CTX-M9 at every site differing from KPC-2 were generated computationally and simulated in an acyl-enzyme complex with meropenem using classical molecular dynamics. The probability of forming hydrogen bonds that stabilize the nascent oxyanion in the deacylation transition state was calculated over these simulations, averaging 5.75 microseconds in total for each of the 125 mutants (minimum of 5.3 μs per mutant), and used to score the mutants. A set of 5 high-scoring mutants and an arbitrary selection of mid-scoring mutants were expressed in E. coli and tested for cefotaxime and meropenem resistance using disc diffusion assays. Results of these tests are shown in Figure 3.1 and Table 3.1. As discussed below, strongly increased hydrogen bond probability is hypothesized to be a predictor of increased resistance but not necessarily in a linear fashion. Three allosteric mutants, L48A, T165W, and S281A, scored particularly well in these tests and were selected for further characterization. Since two of these were alanine mutants, we compared fold-increase in cefotaxime resistance to a set of 13 allosteric CTX-M9 alanine mutants that we tested under identical conditions and reported previously [62]; this comparator group showed a 0.38- to 1.05-fold gain in cefotaxime resistance, so the 1.5- to 3.3-fold gain seen in our three mutants is substantially greater than expected due to chance.

Mutation	Oxyanion hole score	Fold increase cefotaxime resistance	Fold increase meropenem resistance
T165W	0.58	2.62 ± 0.19	1.09 ± 0.12
A140K	0.55	0.96 ± 0.04	1.03 ± 0.03
S266A	0.51	0.62 ± 0.04	1.07 ± 0.01
S281A	0.48	1.57 ± 0.19	1.37 ± 0.02
L48A	0.48	3.34 ± 0.03	1.12 ± 0.02
N271D	0.46	1.00 ± 0.04	1.02 ± 0.02
S220R	0.45	1.16 ± 0.08	0.95 ± 0.02
P167L	0.44		
H112Y	0.42		
N106S	0.40		
Q254T	0.33		
T71S	0.31		
T202P	0.30		
A219H	0.30	0.78 ± 0.04	0.97 ± 0.01
K137L	0.26		
T168E	0.24		
D277A	0.21		
G158T	0.20	1.16 ± 0.04	1.09 ± 0.12

Table 3.1 Top CTX-M9 mutants from simulations with drug resistance measured using disc-diffusion assays.

Oxyanion hole scores were computed from simulations of meropenem acyl-enzymes, and the top five predictions are emphasized with gray highlighting. The fold-increase in cefotaxime and meropenem resistance compared to wild-type was calculated from antibiotic disc assays. Values are reported as median fold increase in inhibitory concentration +/- inter-quartile range. The three highest-resistance mutants showed no impairment in growth .

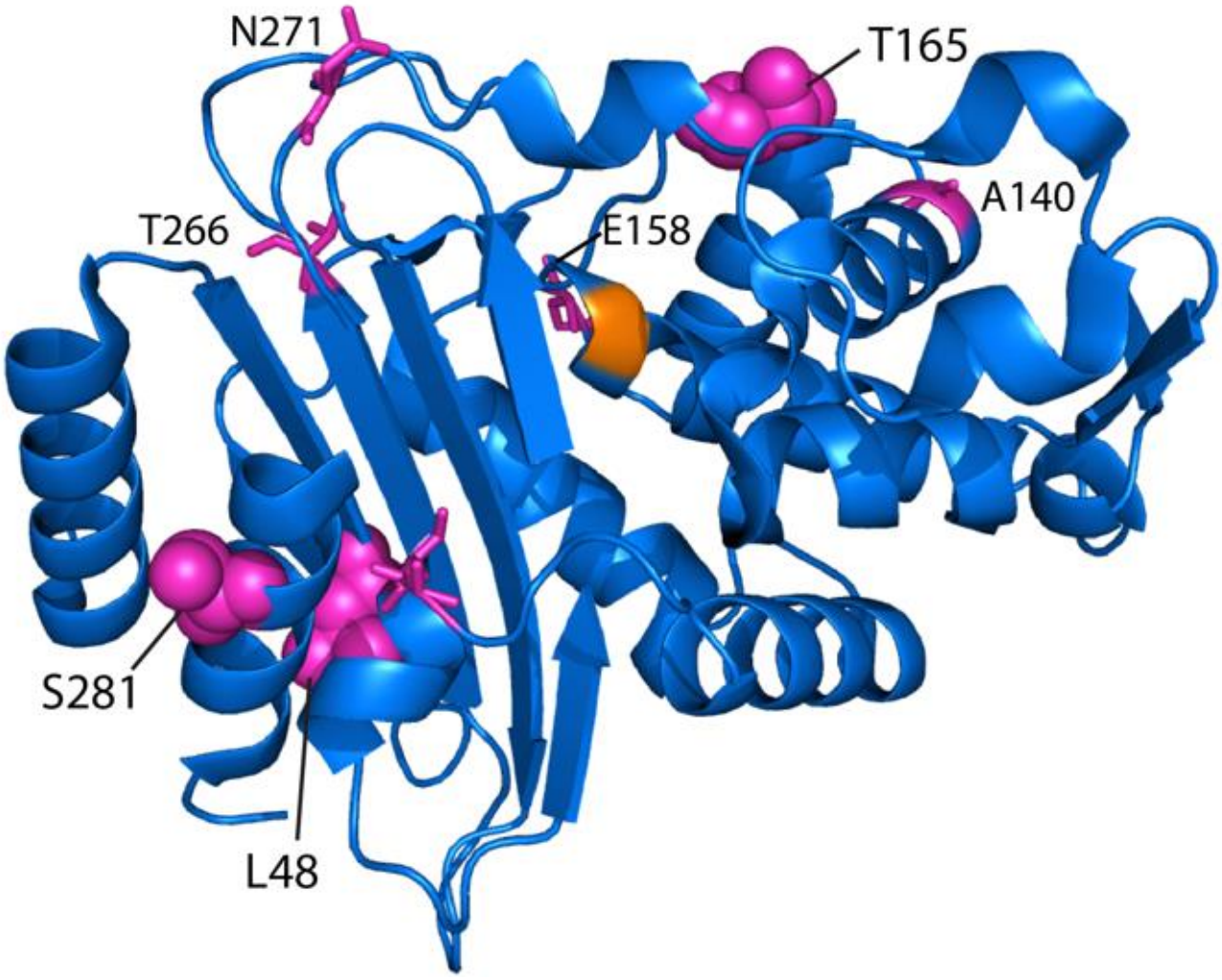

Figure 3.1 CTX-M9 mutants increasing beta-lactam hydrolysis.
The seven top-scoring point mutants from molecular dynamics simulations and two moderate-scoring mutants were transformed into E. coli, and drug resistance was assayed using disc diffusion tests at 37 °C. These top mutations, rendered in magenta on the CTX-M9 structure [120], are located primarily outside the drug-binding-pocket (catalytic serine in orange). Of the five top-scoring mutants from simulation, three (in spheres) showed a substantial increase in cefotaxime resistance and a moderate increase in meropenem resistance.

3.4.2 Broad drug-resistance and bacterial growth rates of high-scoring mutants.

The three top-scoring mutants via experimental gain in cefotaxime resistance were tested against a range of cephalosporin drugs via disc-diffusion assays and showed increased resistance against all of them compared to wild-type CTX-M9 (Figure 3.2). None of these enzymes retarded growth of transformed bacteria compared to wild-type CTX-M9, thus arguing against a fitness penalty for these mutations in the absence of drug. Thermostability assays on purified enzymes showed a 1.5 °C melting temperature stabilization in both the apo and meropenem-acyl forms of CTX-M9 T165W and a mild destabilization (0.5 – 1.5 °C) of the CTX-M9 L48A and S281A mutants (Table 2). Although these shifts were relatively small in magnitude, they were precisely reproducible across three independent experiments per enzyme and are thus considered notable. Based on these data, T165W in particular does not display the stability-function tradeoff that has been previously found in some beta-lactamase mutants [120,153,154].

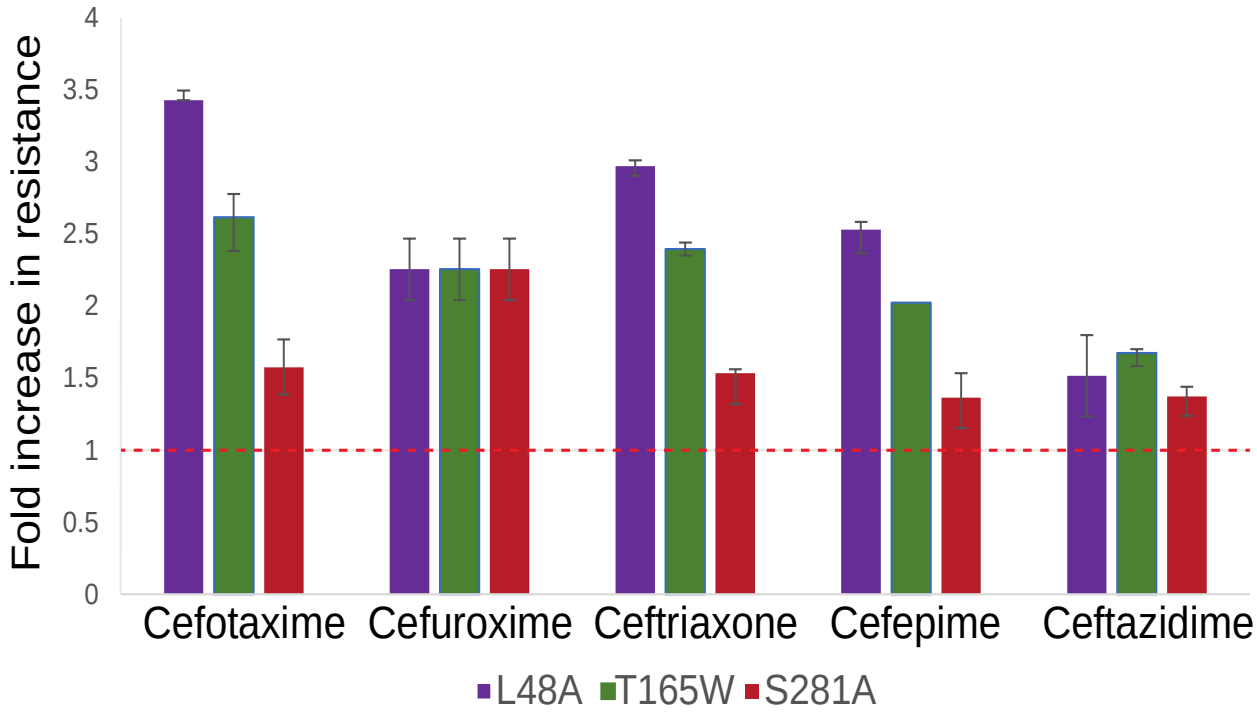

Figure 3.2 Top-scoring mutants increase drug resistance broadly against cephalosporin antibiotics.
Drug resistance to five cephalosporins was measured via Kirby-Bauer disc assays for three top-scoring mutants from initial testing and compared to CTX-M9 wild type. As described in the methods, the fold-increase in inhibitory drug concentration was calculated from disc diffusion assays; values plotted are the median of four independent assays. Wild-type CTX-M9 does not confer resistance to ceftazidime in culture according to clinical lab criteria, although the clinical efficacy of this drug for such infections has been debated [155]. Error bars show inter-quartile ranges. Chemical structures for the drugs used are given in Figure S5.

	CTX-M9	L48A	T165W	S281A
Apo enzyme	48.0 ± 0.5 °C	47.5 ± 0.5 °C	49.5 ± 0.5 °C	47.0 ± 0.5 °C
Acylenzyme	45.0 ± 0.5 °C	43.5 ± 0.5 °C	46.5 ± 0.5 °C	43.5 ± 0.5 °C

Table 3.2 Melting temperatures of apo- and acyl-enzyme conjugates of CTX-M9 and top mutants.

Melting temperatures were determined in increments of 0.5 °C. All enzymes showed a 3-4 °C destabilization in the acyl-enzyme state (measured by pre-incubating enzyme with meropenem); T165W shows a reproducible 1.5-2 °C stabilization compared to the other enzymes, while L48A and S281A show a very mild but consistent destabilization of 1-1.5 °C. Thermal melting curves are given in Figure S6. Uncertainties were limited to 0.5 °C by the precision of the instrument used; agreement between multiple experimental replicas was exact to within this limit.

3.4.3 Steady-state enzyme kinetics

Catalytic parameters of all three top-scoring mutants were determined by measuring the hydrolysis of the cephalosporin antibiotic nitrocefin by purified enzymes and fitting initial velocities according to Michaelis-Menten kinetics. At 28 °C, the S281A mutant displayed the highest nitrocefin k_{cat}, followed by T165W and L48A, with all showing a >two-fold increased k_{cat} over the wild-type enzyme and a >33% increase in catalytic efficiency (Figure 3.3, Table 3.3). Nitrocefin undergoes a shift in visible absorbance upon hydrolysis; these measurements under steady-state conditions yield an aggregate k_{cat} for hydrolysis. These results confirm the phenotypic drug-resistance assays and show that the increased resistance derives from either an increase in k_{ac} or k_{dac} but are insufficient alone to specify which rate constants are altered. Pre-steady-state kinetics of nitrocefin hydrolysis by CTX-M9 suggest that acylation is not rate-limiting. This is consistent with the finding that beta-lactam drugs such as carbapenems that CTX-M9 is unable to hydrolyze are nonetheless readily acylated, although testing nitrocefin was necessary because other beta-lactamases have demonstrated different rate-limiting steps on different classes of substrates. Additionally, E. coli expression levels show that the increase in drug resistance cannot be explained by increased expression of high-scoring CTX-M9 mutants, while preserved or increased K_M argue against increased binding of ligand, suggesting that k_{cat} changes are primarily responsible for the increased resistance.

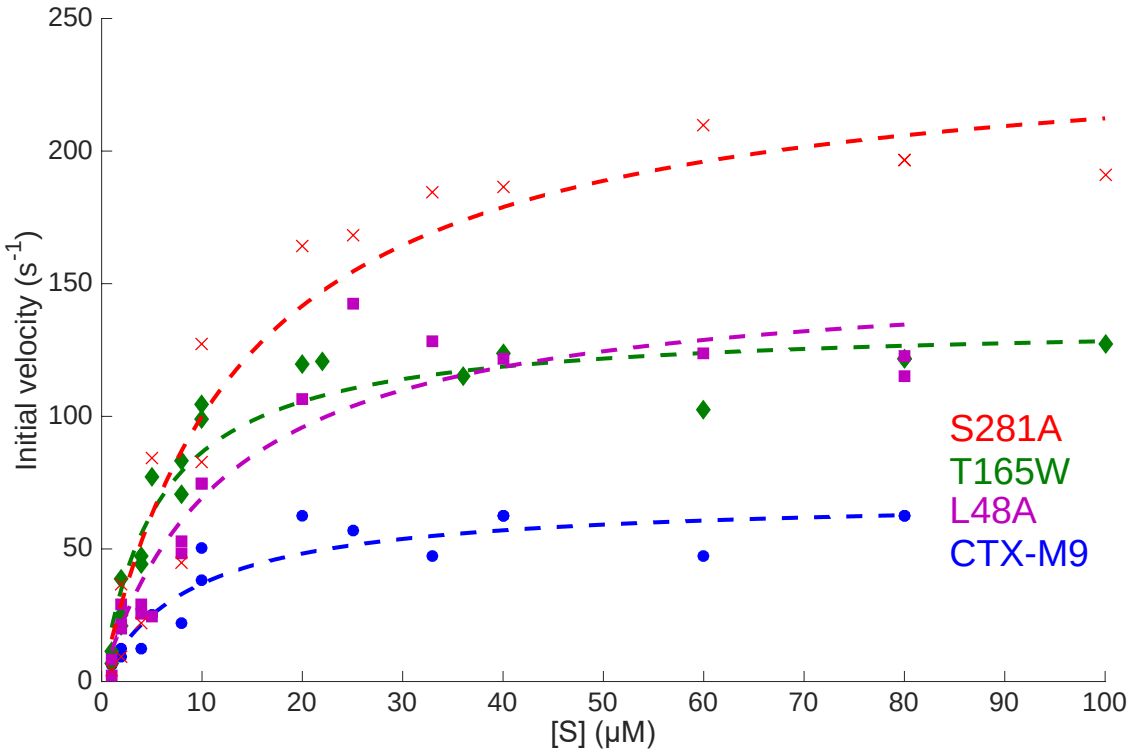

Figure 3.3 Steady-state reaction kinetics show an increased hydrolysis rate of top mutants. Initial velocities for nitrocefin hydrolysis at 28 °C are plotted as a function of substrate concentration with Michaelis-Menten fits overlaid. Experiments were performed at 0.2 nM enzyme, and at least two biological replicas per enzyme were used for fitting. Fit parameters are listed in Table 3 and show a substantial increase in k_{cat} as well as k_{cat}/K_M for all three mutants.

Enzyme	K_M	k_{cat}	k_{cat}/K_M
CTX-M9	8.9µM (8.8-10.6 µM)	70 s^{-1} (69-78 s^{-1})	7.8 μM^{-1} s^{-1} (7.4-7.8 μM^{-1} s^{-1})
L48A	12µM (11.5-13.9 µM)	156 s^{-1} (151-165 s^{-1})	12 μM^{-1} s^{-1} (11.7-13.3 μM^{-1} s^{-1})
T165W	5.7 µM (5.4-6.0 µM)	136 s^{-1} (134-140 s^{-1})	23 μM^{-1} s^{-1} (22.8-24.9 μM^{-1} s^{-1})
S281A	14 µM (12.2-15.8 µM)	243 s^{-1} (236-253 s^{-1})	17 μM^{-1} s^{-1} (15.7-19.4 μM^{-1} s^{-1})

Table 3.3. Steady-state reaction parameters for CTX-M9 and top mutants.
K_M and k_{cat} were determined via nonlinear Michaelis-Menten fits to steady-state initial velocity data. As predicted from simulations, k_{cat} increased substantially in these mutants. This gain did not come at a cost in catalytic efficiency, as k_{cat}/K_M also increased. 95% confidence intervals were calculated via jackknife methods.

3.4.4 Structures of CTX-M9 mutants

To rule out a structural change in the low-free-energy conformations of these mutants, we crystallized all three mutants and performed X-ray diffraction studies. The S281A mutant only diffracted to 6 Å and was not refined, but the structures of CTX-M9 L48A and T165W were solved to 1.73 and 1.8 Å resolution and were indistinguishable from the wild-type enzyme with RMSD of 0.3 Å (Figure 3.4). Structures have been deposited as PDB codes 5KMT and 5KMU. Ligand soaks of these crystals with cefoxitin as previously reported [120] yielded low occupancy, but based on the close similarity of catalytic side chain structure in the *apo* and acyl-enzyme forms of CTX-M9, we expect the low-free-energy conformation to be similar in any trapped acyl-enzyme state. We expect this because a structural difference associated with a more catalytically active mutant would manifest as an acyl-enzyme intermediate more closely resembling the deacylation transition state. Since these two structures are already quite similar for wild-type CTX-M9, we conclude such differences would be quite small, and indeed our simulations of the acyl-enzyme complexes also do not show large structural differences.

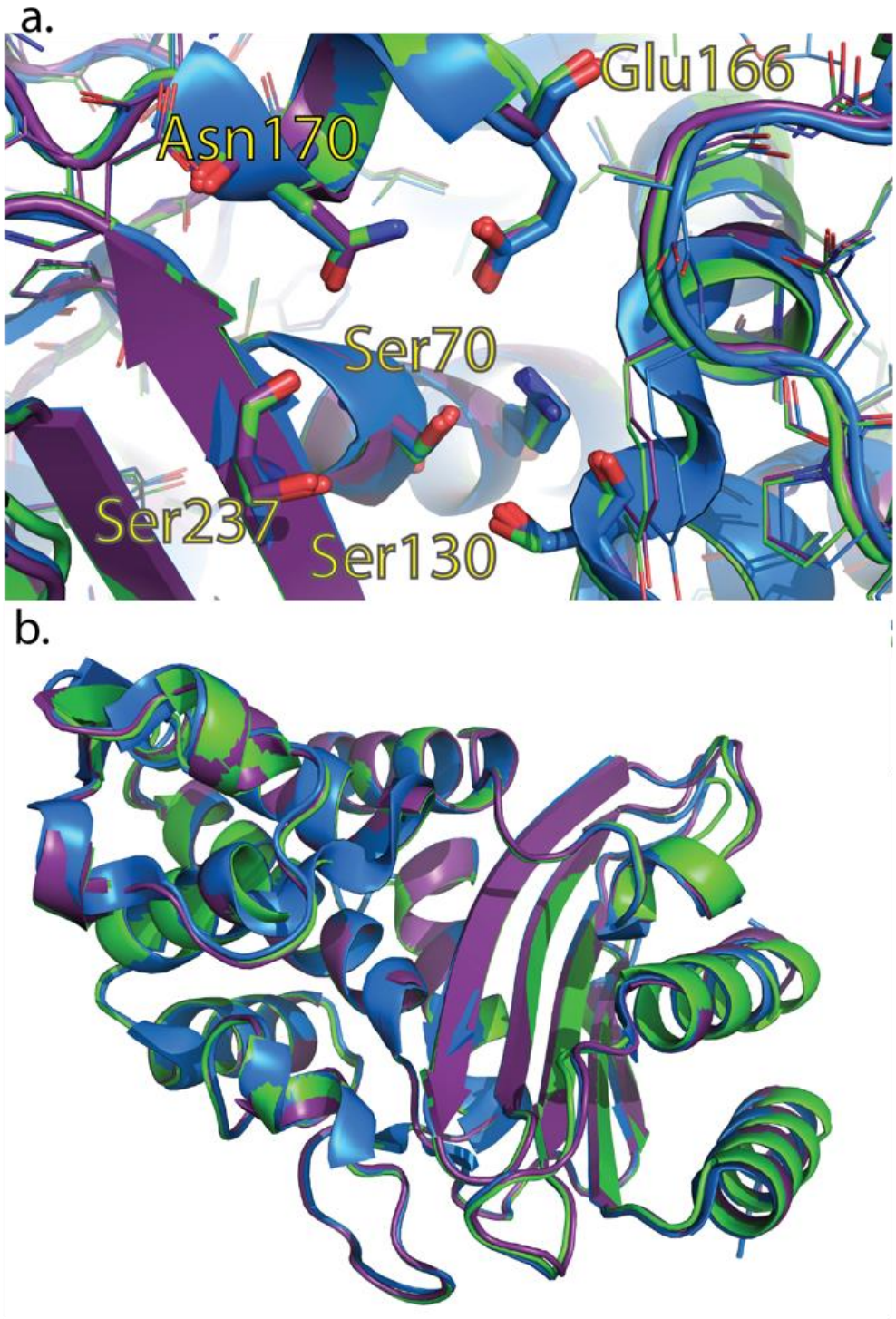

Figure 3.4 Crystal structures of L48A and T165W mutants show no substantial changes from wild-type *apo* enzyme.
Wild-type CTX-M9 (blue) is rendered overlaid with the L48A (purple) and T165W (green) mutants. Crystal structures of these two mutants show no substantial change in the *apo* form in the active site region (panel a) or globally (panel b). All-atom RMSD values are 0.3 Å respectively between each of the mutants and wild-type CTX-M9.

3.4.5 Simulations yield a hypothesis for allosteric effects

Based on our experimental data, we predict that the three mutant enzymes display differences in the population distribution of the acyl-enzyme conformational ensemble rather than large shifts in the lowest-free-energy structure. To localize potential differences and predict how distant mutations may affect enzyme-drug interactions, we calculated root-mean-square fluctuation (RMSF) for all non-hydrogen atoms in simulations of each mutant acyl-enzyme with meropenem and compared them to the wild-type acyl-enzyme simulations. Residues showing the highest percent magnitude difference from wild-type are shown and visualized on the enzyme structure in Figure 3.5. For CTX-M9 L48A and T165W, we observed a substantial increase in conformational flexibility of the loop in the region 103-105 that has been shown important in substrate binding and hydrolysis for a number of class A beta-lactamases [65,156–158]. No such increase was observed in S281A. All three mutants showed an increase in flexibility of N170, an active-site residue thought to be involved in positioning the catalytic water for hydrolysis [135]. In addition, R276, a residue at the edge of the binding-pocket that can interact with the free carboxylate of meropenem or cefotaxime [102,146], increased in flexibility, as did the 221-225 helix in the S281A simulations, although the significance of this last region for enzyme-drug interactions is unclear. There was also an increase in the flexibility of other omega loop residues in the T165W and L48A simulations with meropenem. These findings from simulation lead us to speculate that some combination of V103-Y105 loop interactions and N170 interactions with the drug might be related to the increased drug resistance of the mutant enzymes.

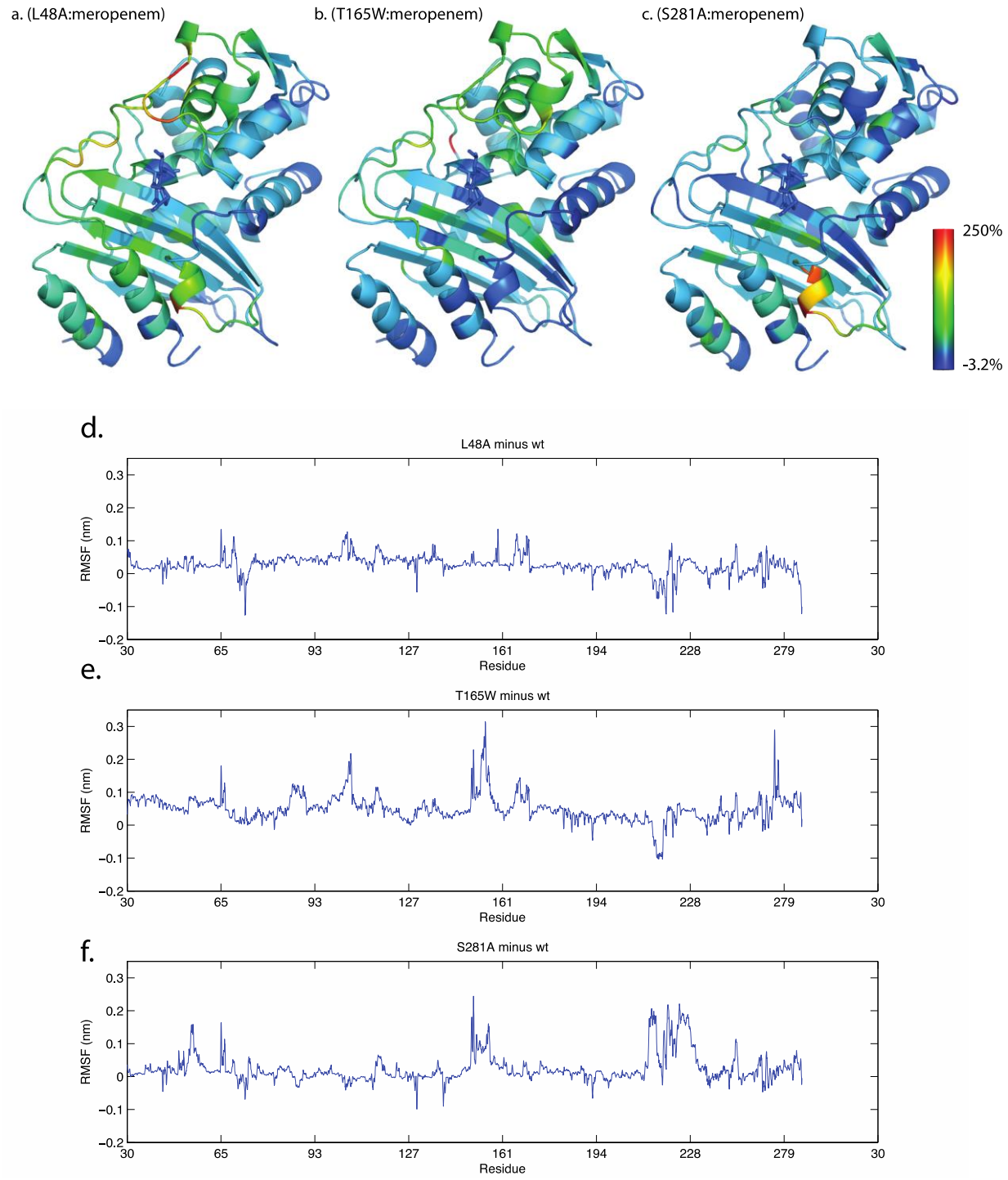

Figure 3.5 Residues of mutant enzymes showing increased flexibility compared to wild-type in simulations with meropenem.

Each CTX-M9 mutant is rendered with residues colored from blue to red in order of increasing percent difference RMSF compared to the corresponding residue in simulations of wild-type CTX-M9. This yields a visual interpretation of which residues show increased conformational flexibility, which is quantitated as a set of per-residue RMSF plots in panels d-f.

We also used simulations to directly predict how our top-scoring allosteric mutations S281A, L48A, and T165W alter the conformational ensemble of the substrate-binding-pocket to effect a change in drug resistance. We employed a machine-learning technique called max-mutual information feature selection [159] on each of the meropenem and cefotaxime acyl-enzyme datasets as follows. In each snapshot from molecular dynamics simulations of wild-type and top-scoring mutant acyl-enzymes, we calculated the mutual information, a nonlinear statistical metric of relatedness, between the position of each binding-pocket atom and sequence of the enzyme. Averaged over the entire mutant dataset, this yields an information-theoretic score for which atoms in the binding-pocket are most positionally responsive to the mutations under study. For the meropenem acyl-enzyme dataset, top-scoring atoms by this criterion are from residues 234, 166, and 104 (Figure 3.6). As a further validation, we trained a decision tree machine-learning classifier (Figure 3.7). Using only the top 10 binding-pocket atoms, we predict the mutation that corresponds to a given binding-pocket conformation with 95.8% accuracy via 10-fold cross-validation (and 99.4% accuracy using the full binding-pocket). Simulations of these mutations in acyl-enzyme complex with cefotaxime identify these residues as well as residue 105 as top-scoring. We thus predict that the S281A, L48A, and T165W mutant enzymes alter the acyl-enzyme conformational ensemble and thus the catalytic rate by changing the positions of residues 104, 166, and 234 in this ensemble, although not in the apoenzyme crystal structures. Of these residues, glutamate 166 is involved in coordinating catalytic water molecules in hydrolysis [120], asparagine 104 has been implicated in substrate positioning in the acyl-intermediate form of other beta-lactamases [136,141], and lysine 234 is highly conserved and thought to interact with the cephalosporin C3 carboxylate moiety [135].

Although all these active-site residues and the allosteric sites 48 and 165 are ≥ 99% conserved within the CTX-M family, approximately 25% of CTX-M sequences contain the S281A mutation. Using a multiple sequence alignment of 500 beta-lactamases most closely related to CTX-M9, residues 281 and 105 showed a strong sequence co-variation, quantified as phylogenetically corrected sequence mutual information [160]. We also analyzed residue-residue dynamic relationships via positional mutual information (as opposed to residue-mutant relationships). Four simulation datasets were examined per mutation site: wild-type meropenem acyl-enzyme, wild-type cefotaxime acyl-enzyme, mutant meropenem acyl-enzyme, and mutant cefotaxime acyl-enzyme. Residue K234 ranked in the top 5 binding-pocket residues linked to residue 48 in 3 of 4 datasets. E166 was most closely linked to residue 165 in all simulation datasets (although this can be explained by proximity), and 104 scored in the top 5 once. K234 again scored in the top 5 binding-pocket residues linked to residue 281 for 3 of 4 datasets. No other binding-pocket residue was similarly enriched in linkage from more than one allosteric site.

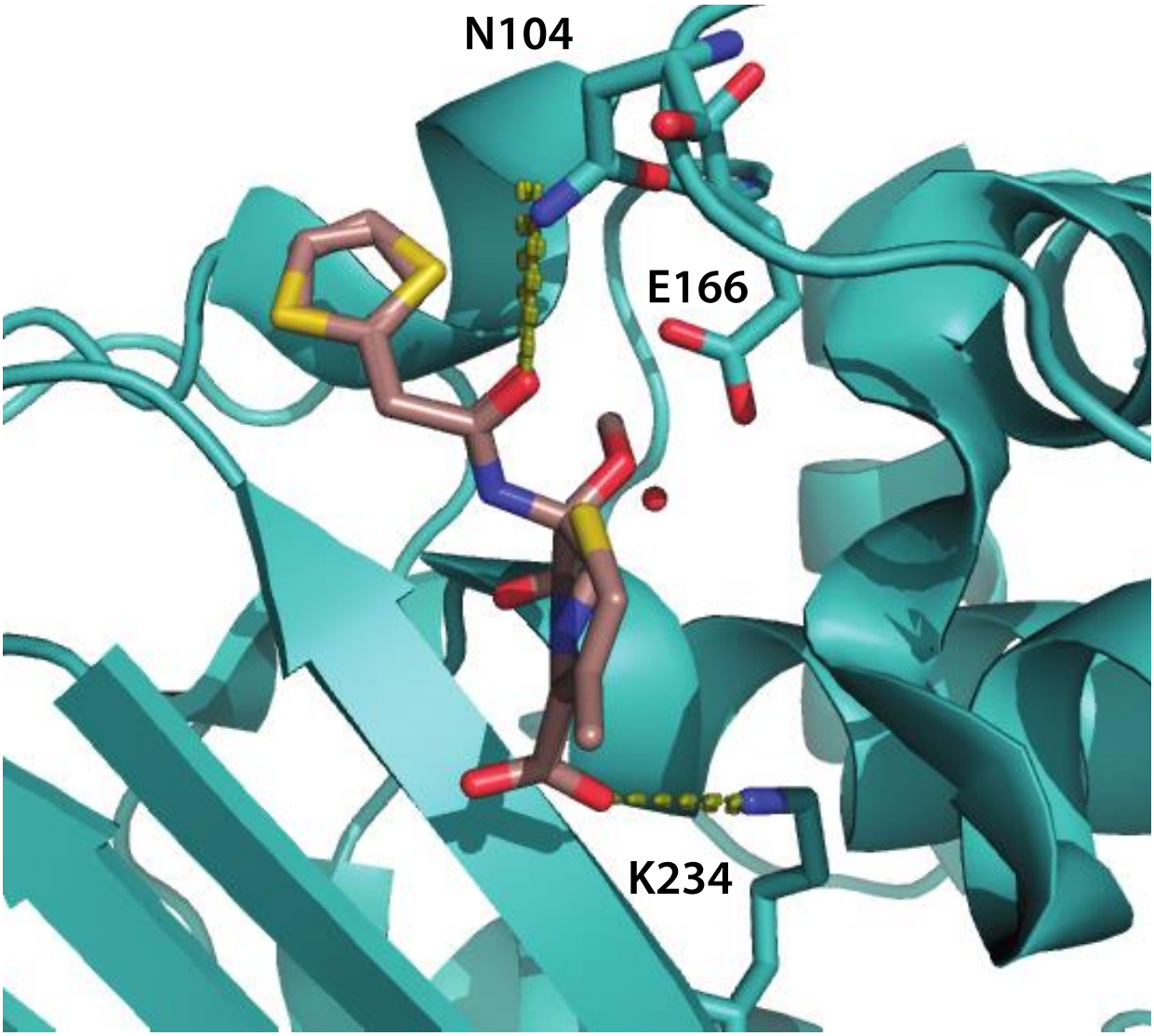

Figure 3.6 Top binding-pocket residues predicted to transmit allosteric mutations.
The top three binding-pocket residues that change position with allosteric mutations affecting cephalosporin resistance are rendered in cyan sticks, visualized using the crystal structure of CTX-M9 in the acyl intermediate form with cefoxitin [120] (rendered in tan). Dotted lines show key interactions between the ligand and N104 and K234; E166 is believed to interact via a catalytic water molecule.

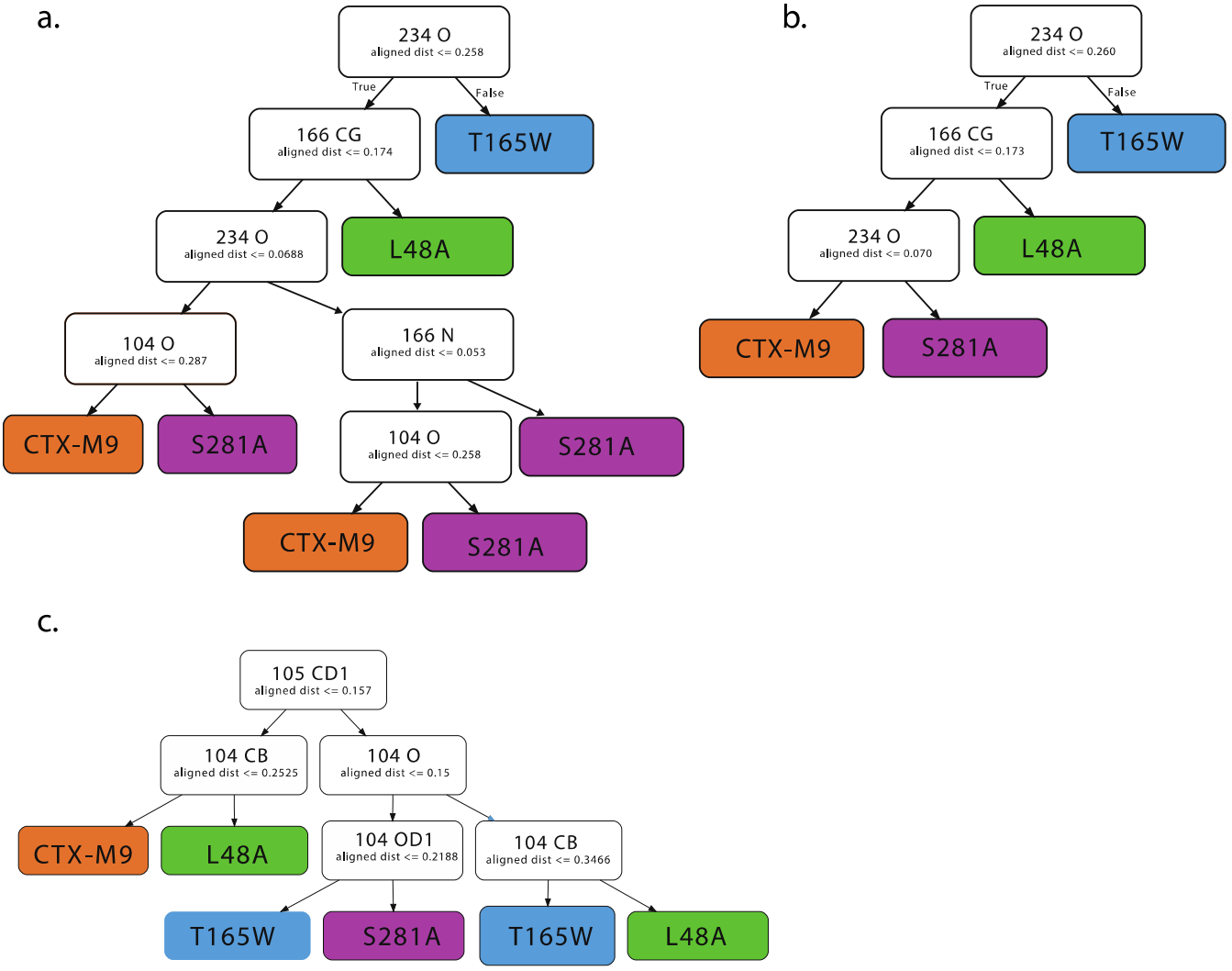

Figure 3.7 Binding-pocket atoms that shift position with allosteric mutations.
Rendered is a decision tree trained on top-scoring binding-pocket atoms that uses the aligned distance in each simulation snapshot of each atom from a reference CTX-M9 wild-type crystal structure in complex with cefoxitin (PDB ID 1YMX) [120] to classify the mutant being simulated. Since this procedure is performed on binding-pocket atoms only, it identifies the binding-pocket atoms most reflective of allosterically induced conformational changes. Binary decision trees were trained on acylenzyme simulations in complex with meropenem using the 10 top-scoring atoms and (1) unrestricted tree size, (2) tree size restricted to 7 leaf nodes (panel a), and (3) tree size restricted to 4 leaf nodes (panel b). These trees achieve a 10-fold cross-validation accuracy of 86.8 and test set classification accuracy of 86.9% for the 4-node tree, 89.3% cross-validation and 89.2% test set accuracy for the 7-node tree, and a cross-validation accuracy of 95.6% and a test set classification accuracy of 91% for the unrestricted tree. An unrestricted tree trained on all binding-pocket atoms (not just the top 10) achieved a cross-validation accuracy of 98.9% and a test-set accuracy of 97.9%. An additional decision tree trained on acylenzyme simulations in complex with cefotaxime is rendered in panel c. This had a cross-validation accuracy of 85.7% and test-set accuracy 85.5% when restricted to a maximum of 7 leaf nodes and 93.0% and 86% respectively when unrestricted in size but limited only to the top 10 binding-pocket atoms.

3.5 Chapter Discussion

Allosteric mutants that increase the activity of an already competent beta-lactamase represent a challenging prediction target, and successful prediction often yields moderate rate enhancement in these cases, in contrast to the larger gains when successfully engineering new substrate activity. Our results demonstrate that simulations of acyl-enzyme conformational dynamics can prospectively identify new allosteric mutations and that the mechanism of such mutations is consistent with a change to the acyl-enzyme intermediate or the deacylation transition state. Clearly, simulations of these conformational dynamics—the classical dynamics in the acyl-enzyme state—neglect much of the hydrolysis process and thus cannot by themselves be expected to capture mutations that affect ligand binding, the acylation transition state, or the reactive chemistry directly. Those steps have been the subject of other simulation studies [38,155,161–167], and it is hoped that a combined multimodal approach may yield a more comprehensive understanding of mutations affecting CTX beta-lactamase function. Our results are striking in that they show how acyl-enzyme conformational dynamics can identify allosteric mutations that do not substantially alter minimum-free-energy structures (of the *apo* enzyme and, we speculate, other intermediates) yet increase catalytic rates and resistance to clinically used antibiotics several-fold. As might be expected, the allosteric mutations thus identified do not lie in the thermostable or rigid core of the molecule—in our tests, mutations there are more likely decrease rather than enhance function. The oxyanion hole stabilization metric used to score mutants is believed necessary but not sufficient for hydrolysis and is likely noisy due to simulation sampling. It thus is not expected to be a linear predictor of k_{cat} but nonetheless demonstrates good predictive ability in identifying mutants with increased resistance (3/5 top-scoring mutants have increased resistance).

If we classify the conformation ensemble of the acyl-enzyme state as an equilibrium between microstates that would stabilize an oxyanion (OXY) and microstates that would not (NON), our simulation dataset samples the OXY->NON conversion rate much better than the NON->OXY conversion rate. We ascribe the predictiveness of oxyanion hole scores computed using meropenem acyl-enzyme simulations for cephalosporin resistance to a correlation between OXY->NON conversion rates across mutants for these drugs. Additionally, since meropenem acyl-enzyme simulations display somewhat faster OXY->NON rates, these simulations provide statistically better-converged estimators of the oxyanion hole scores. We also believe that undersampling of the slow NON->OXY conversion rate also likely explains why our simulation dataset is not predictive of meropenem resistance.

This modulation of activity without substantially changing dominant conformation raises the question of whether our high-scoring mutations alter the free energy of the deacylation transition state and thus control the rate-limiting step for beta-lactam hydrolysis by CTX-M9. Classical molecular dynamics calculations that do not explicitly treat reactivity will not capture this directly. However, the scoring method we use here to assess hydrogen bonds that would stabilize an oxyanion in the deacylation transition state does succeed in predicting (either mechanistically or serendipitously) a set of mutants that increase catalytic activity. We therefore hypothesize that the predicted mutations either decrease the free energy of the deacylation transition state ensemble, likely via oxyanion stabilization, or alter the free energy of the acyl intermediate conformational ensemble with an overall effect of reducing the $\Delta G^{\ddagger}$ for deacylation. The kinetic data support an increase in k_{cat} and, although they do not specifically prove an increase in k_{dac}, are consistent with this hypothesis.

Point mutations that increases resistance to clinically used drugs at no apparent fitness cost—identical growth rates and for at least one mutant improved thermal stability—raise the question of why these mutants have not fixed in the bacterial population. We hypothesize that these indicate that the primary selection factor for CTX-M9 beta-lactamase fitness in the wild must not be cephalosporin hydrolysis (or likely any clinically used beta-lactam) but some non-pharmacological toxin. This would not be surprising given that beta-lactamases likely arose as defences against microbial toxins. However, even circumstantial evidence that these and not pharmacological therapy dominate selection raises interesting implications for the further evolution of drug resistance. Such evidence implies that selection results from the interplay of microbial chemo-ecology and human intervention rather than a scenario where diversity was generated by microbial interactions and current selection is primarily driven by human factors [168–170].

3.6 Chapter Conclusion

Allosteric mutations that enhance k_{cat} raise an important mechanistic question of how the allosteric change is manifested in the binding-pocket. General theories of allostery include analyses of spatial transmission paths or modulation of protein conformational ensembles [171]. Here, we show allosteric mutations that enhance k_{cat} without substantially altering the active-site conformation in apoenzyme crystal structures. Machine-learning analyses can query how the conformational *ensemble* of the binding-pocket is altered by these mutations in simulations and thus predict how distant changes may manifest in the binding-pocket. Our results suggest a particular subset of residues involved in substrate positioning or coordinating catalytic water change in their conformational distribution with allosteric mutations that increase k_{cat}. These findings will help guide future analyses of CTX-M9 substrate specificity and provide a

generalizable method for identifying specific binding-pocket residues with altered conformational ensembles in allosteric mutants.

Chapter 4. A Conformational Intermediate that Controls KPC-2 Catalysis and Beta-lactam Drug Resistance

4.1 Foreword

In Chapter 3, the success of the prediction of mutations which enhance the function of CTX-M9 is likely the result of measuring alterations to an off-pathway conformational transition. In this Chapter, we characterize a similar conformational transition that controls KPC-2's ability to hydrolyze carbapenem antibiotics. Because the conformational dynamics of KPC-2 are complex and sensitive to allosteric changes, we develop an information-theoretic approach to identify key determinants of this change. We measure unbiased estimators of the reaction coordinate between catalytically permissive and non-permissive states, perform information-theoretic feature selection and, using restrained molecular dynamics simulations, validate the protein conformational changes predicted to control catalytically permissive geometry. We identify two binding-pocket residues that control the conformational transitions between catalytically active and inactive forms of KPC-2. Mutations to one of these residues, Trp105, lower the stability of the catalytically permissive state in simulations and have reduced experimental k_{cat} values that show a strong linear correlation with the simulated catalytically permissive state lifetimes.

4.2 Chapter Introduction

Here, we seek to understand the conformational determinants of catalytic permissivity in the KPC-2 acyl-enzyme intermediate. This involves integrating two pieces of data: structural and chemical studies suggest that an oxyanion hole is required for efficient deacylation [27,35,41,46,172] while kinetic studies show the existence of an equilibrium between on-pathway and off-pathway structural forms of the acyl-enzyme intermediate [38,46,173–178] (Figure 4.1a, Figure 4.1b). Our prior work and that of others [27,38,63] suggests that these two may be linked:

in studying the related enzyme CTX-M9, we found kinetic evidence of an off-pathway intermediate, while molecular dynamics simulations also showed an equilibrium between conformations forming an oxyanion hole and those that did not. We showed that allosteric mutations that stabilized the oxyanion hole demonstrated increased catalytic activity in CTX-M9. We therefore hypothesize that these conformational transitions relate to the kinetic relationship between catalytically permissive acyl-enzyme states and catalytically nonpermissive ones for both CTX-M9 and, critically, KPC-2. We therefore seek to understand the conformational transitions between oxyanion-hole states of KPC-2 and non-oxyanion-hole states, identify what features of the protein potentiate such changes, and to use this information to understand mutations that increase or decrease drug-resistance of this clinically important enzyme.

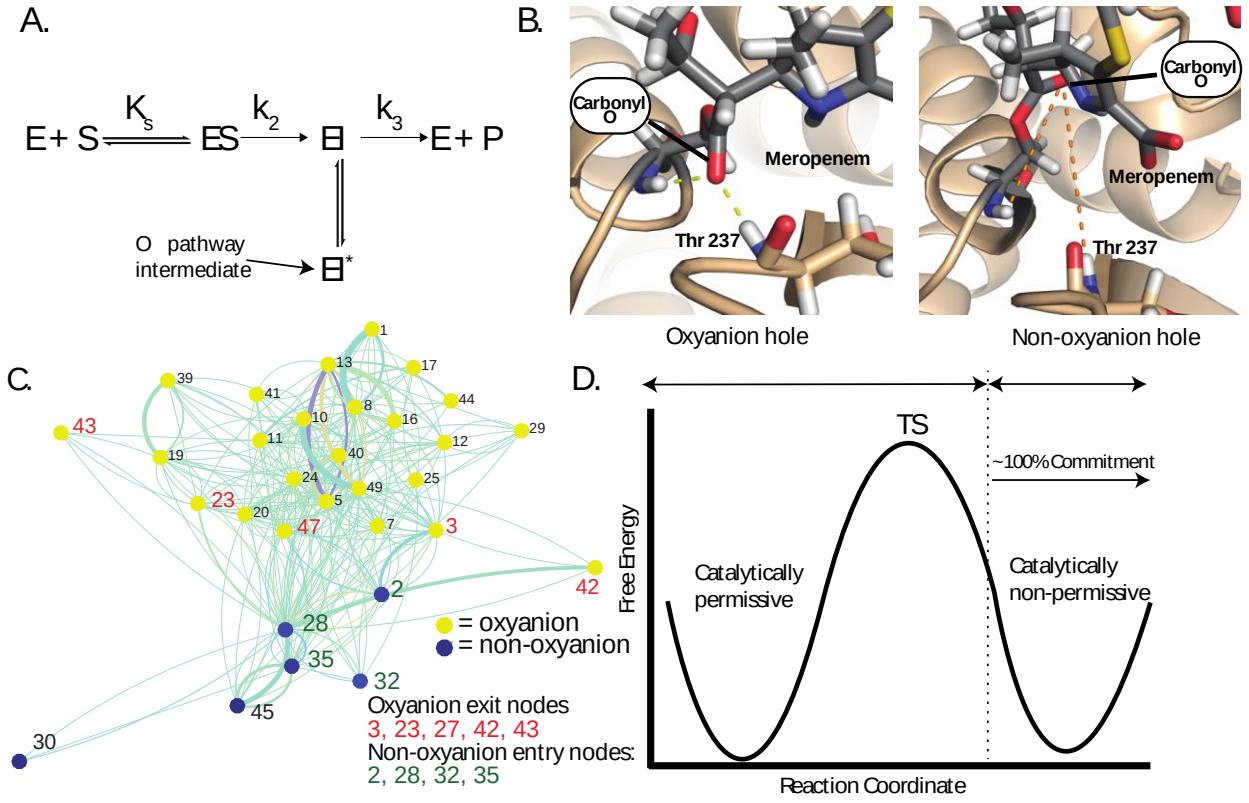

Figure 4.1 Hydrolysis of beta-lactam drugs by KPC-2 involves an off-pathway intermediate that correlates with conformational changes in the acyl intermediate state.
(A) Reaction diagram for beta-lactam hydrolysis by KPC-2 with off-pathway intermediate demonstrated for CTX-M9 and hypothesized for KPC-2. (B) Rendering of hydrogen bonds stabilizing an oxyanion hole in the KPC-2 acyl-enzyme (left) and alternate conformational state that does not stabilize an oxyanion hole (right). (C) Kinetic clustering of KPC-2 simulations shows a subnetwork of oxyanion-hole conformations, a subnetwork of non-oxyanion-hole conformations, and a flux pathway between these that retains an oxyanion-hole hydrogen bonding pattern until relatively late. (D) One-dimensional free-energy schema showing that the transition state for conversion between oxyanion-hole and non-oxyanion-hole conformations occurs before hydrogen bonds are actually lost, as confirmed by subsequent committor analysis.

Understanding transitions in and out of the oxyanion hole and identifying related protein conformational features requires a robust set of order parameters for the free-energy landscape involved. Our initial results indicated that formation of the oxyanion hole state itself, while catalytically required, was not a sufficient determinant of kinetic stability. We therefore employed committor analysis as a means to identify members of the transition state ensemble between catalytically permissive and nonpermissive conformations and to yield an unbiased estimate of the order parameter [179–181]. Using this analysis, we identify critical changes in the drug-binding-pocket that precede and control transitions out of the catalytically permissive state. We demonstrate in molecular dynamics simulations that reversing these transitions drives formation or dissolution of the oxyanion hole. Finally, we validate our predictions by showing that the simulated oxyanion hole lifetimes of mutants at these sites correlates with experimentally measured k_{cat} values for these mutants.

4.3 Methods

4.3.1 Molecular dynamics simulations

Simulations of the KPC-2:meropenem acyl-enzyme were performed using structures and parameters we have previously reported [63]. Briefly, an initial structure with the beta-lactam carbonyl in an oxyanion hole was constructed by least-squares fitting of a SFC-1:meropenem acyl-enzyme structure (PDB code 4EV4) onto the KPC-2 *apo* crystal of KPC-2 (PDB code 2OV5) with the carbonyl beta-lactam hydrogen-bonded to backbone amide protons of Ser70 and Thr237 [38,41]. The protein was placed in an octahedral box with 2 nm minimum periodic separation and solvated with TIP3P water and 150 mM NaCl. This starting state was energy-minimized and equilibrated as previously described prior to production simulations [63]. Simulations were run

using Gromacs 5.1 [123] and AMBER99SB-ILDN protein parameters [125,182]. Meropenem parameters were determined as previously reported [63]. Hydrogen bonds were constrained using LINCS and short-range interactions were truncated at 1.2nm. Long-range electrostatics were treated using Particle Mesh Ewald [128]. Simulations were run with temperature maintained at 310K using a velocity-rescaling thermostat [127] and pressure at 1 bar using a Berendsen barostat. An initial set of 20 simulations each at least 480 ns in length were run from this starting conformation with starting velocities randomly assigned from a Maxwell distribution. Further simulation datasets used in committor analysis and prediction of mutants are described below.

4.3.2 Kinetic map construction

Conformational states of KPC-2:meropenem were determined via an initial fine structure-based clustering of simulation snapshots taken at 50-ps intervals followed by kinetically driven secondary clustering. A single round of k-centers clustering on RMSD of the drug-binding-pocket (see Supplementary Information in Appendix B) to a cutoff of 1 Å RMSD was followed by 10 rounds of k-medoids optimization to yield 2402 fine clusters with RMSD of 0.6 Å from each cluster medoid averaged over the dataset. Kinetically driven clustering was then performed using Robust Peron Cluster-Cluster analysis [183] on the connectivity graph obtained by mapping the original simulation trajectories onto the fine clustering to yield 50 conformational states. The resulting map was visualized as a directed graph with edge weights between nodes *i* and *j* proportional to the probability of an *i-j* transition in the simulation trajectories. This map was then analyzed for transitions from oxyanion-hole conformational states to non-oxyanion-hole conformational states using a 3.3-Å cutoff definition of a hydrogen bond. Additional details are given in Appendix B.

4.3.3 Committor analysis

Because two metastable free-energy basins were observed in the original set of simulation trajectories, commitment probability [181] between the two was calculated to yield a robust reaction coordinate. The catalytically permissive (EI) basin was defined as hydrogen-bonds according to the Wernet Nilsson criteria [184] between: the backbone amides of Thr237 and Ser70 and the beta-lactam carbonyl oxygen, the side chain of Asn132 and meropenem 6α-1R-hydroxyethyl, and the side chains of Glu166 and Asn170. The catalytically nonpermissive (EI*) basin was defined as a loss of the oxyanion hole hydrogen bonds and a distance greater than 1 nm between Glu166 ɣO and Asn170 αC or Asn170 ɣC and Glu166 αC. We compute a number of unbiased molecular dynamics trajectories starting from some point X in conformation space and calculate the number of simulations n_{EI} that reach basin EI before basin EI* and the number of simulations n_{EI*} that reach basin EI* before basin EI. The commitment probability $P_X = n_{EI} / (n_{EI} + n_{EI*})$ is thus a robust reaction coordinate that depends only on the structural definition of the metastable basins and does not require prior knowledge of any collective variables or order parameters. We performed this analysis on 20 conformational snapshots resampled from an unbiased molecular dynamics simulation trajectory that started in EI and ended in EI* to classify the conformational transition and obtain a member of the transition state ensemble similar to an approach used previously for other complex biomolecular reactions [179]. Between 20 and 80 unbiased simulations were used per starting point with a minimum length of 50 ns per simulation. Committor value uncertainties were estimated via bootstrap resampling.

4.3.4 Identification of protein conformational transitions that control catalytic permissivity

Since beta-lactam drug reorientation occurred relatively late in the transition between catalytically permissive and nonpermissive states, we performed information-theoretic feature selection to determine which protein conformational transitions control catalytic permissivity. In addition to the 20 conformations for which committor values were calculated directly, we imputed committor values for related snapshots via agglomerative clustering, yielding 35,651 conformational snapshots fully committed to EI and 4,448 snapshots fully committed to EI*. These two datasets were reweighted to yield a balanced dataset, and minimum-redundancy, maximum-relevance feature selection [159] was then applied to identify the 10 protein-protein interatomic distances that best differentiated EI and EI* states (see Appendix B for details on clustering and feature selection).

To test the effect of these top 10 distances on determining rather than just reporting on catalytic permissivity, we selected KPC-2:meropenem conformations that were strongly committed to either EI or EI* and asked whether biasing the EI-starting conformations to the top-10 distances found in EI* conformations would change overall commitment and vice versa. To test this, we ran an additional set of 20 committor-analysis trajectories with a Hamiltonian bias on the top 10 distances using a minimal-biasing potential formulation [185]. These simulations were run until commitment to either EI or EI* to estimate committor values under biasing and compare with unbiased committor values.

4.3.5 Testing of KPC-2 point mutants

A series of Trp105 point mutants were generated, simulated, and the EI state lifetime compared to experimentally measured k_{cat} values as follows: each point mutant structure was

generated via Modeller [186] using a KPC-2:meropenem conformational snapshot in the EI state as a template. Energy minimization and equilibration were performed identically to the KPC-2:meropenem wild-type enzyme with the exception that position restraints were applied to each atom in the mutant residue 105 that had a matching atom in the wild-type structure, bringing the mutant residue 105 into alignment with the wild-type Trp105. 20 simulations were run per mutant, each until EI* state commitment or > 100 ns. EI state lifetime for each mutant was estimated by calculating the average probability of satisfying criteria for state EI across all simulations and fitting a double-exponential decay to these data after applying a Gaussian filter to correct for fast time-scale fluctuations. The aggregate decay constant, $\tau = A_1\tau_1 + A_2\tau_2$, where A is amplitude and τ is the decay constant, was then compared to experimental k_{cat} values previously reported[64].

4.4 Results and Discussion

4.4.1 Kinetic map of KPC-2 conformational transitions

We constructed an initial kinetic map of conformational transitions of KPC-2 by starting 20 independent simulation trajectories of the KPC-2:meropenem acyl-enzyme from the catalytically permissive, oxyanion hole state. 11 of these assumed a non-permissive state with loss of the oxyanion hole within 500 ns of simulation. We then used these simulations to construct a kinetic map of the conformational transitions associated with loss of the oxyanion hole in KPC-2. This map (Figure 4.1c), generated by fine structural clustering and then analysis of the resulting kinetic network (see Methods), surprisingly showed that loss of the oxyanion hole occurred quite late in the transition from permissive to nonpermissive states. Both oxyanion-hole and non-oxyanion-hole conformations formed kinetic subnetworks with substantial exchange among conformational clusters, but the pathway from oxyanion-to-non-oxyanion conformations included

a large number of oxyanion-hole conformations that demonstrated unidirectional flow towards the non-oxyanion-hole state within our initial sampling. This finding suggests that the hydrogen bonds supporting an oxyanion hole are alone insufficient to define a metastable free-energy basin for catalytically permissive conformations of KPC-2. We therefore developed a more robust set of criteria to capture this metastable basin as outlined below.

4.4.2 An unbiased reaction coordinate for KPC-2 conformational transitions

We employed committor analysis to develop a more robust reaction coordinate for conformational transitions of the KPC-2 acyl-enzyme between catalytically permissive and nonpermissive states. Briefly, committor analysis relies on running a large number of molecular dynamics trajectories starting from the same point in conformation space; given a set of metastable basins {A, B, …}, the committor value of that starting point in phase space is defined as (a_i,b_i,...), where a_i is the fraction of trajectories that reach state A before any other defined basin. This provides a reaction coordinate for an arbitrarily complex free-energy landscape that depends only on the definitions of the metastable basins. Based on prior analysis of KPC-2 [38,41,187], we defined the catalytically permissive basin as conformations fulfilling the following criteria: hydrogen bonds between: (1) the backbone amides of Thr237 and Ser70 and the beta-lactam carbonyl oxygen that form the oxyanion hole, (2) the side chain of Asn132 and meropenem 6α-1R-hydroxyethyl, and (3) the side chains of Glu166 and Asn170. We defined the nonpermissive basin as conformations showing 1) a loss of the oxyanion hole and (2) distance greater than 1 nm between Glu166 ɣO and Asn170 αC or Asn170 ɣC and Glu166 αC (Figure 4.2a, 4.2b). We then ran "shooting" trajectories from starting conformations resampled from an unbiased permissive-to-nonpermissive molecular dynamics trajectory of the KPC-2 acyl-enzyme (Figure 4.2c) and

applied committor analysis in order to better understand the free-energy landscape of this transition.

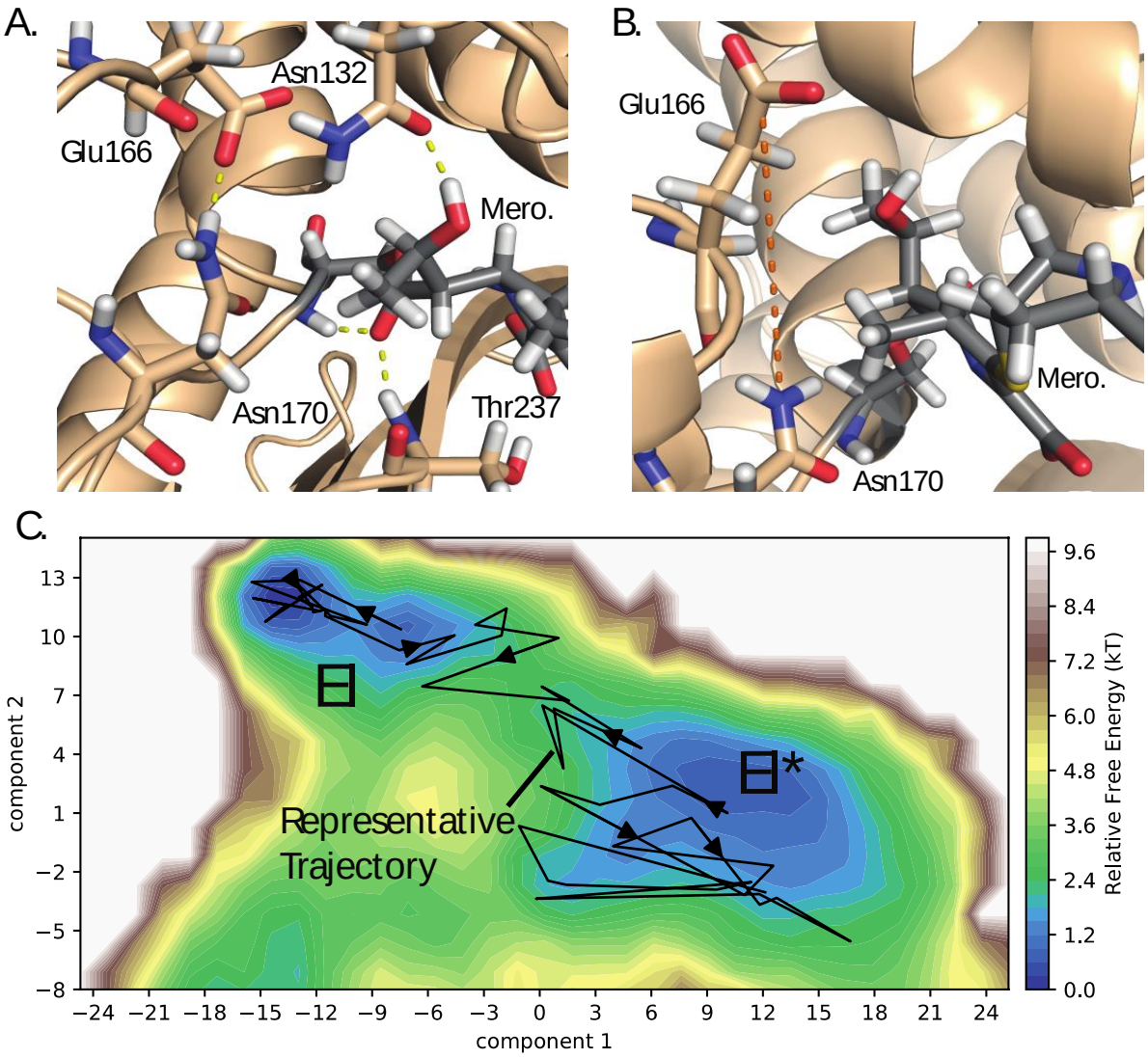

Figure 4.2 Metastable basins of catalytically permissive and nonpermissive state in KPC-2 Rendered in (A) and (B) are the intramolecular distances (dashed lines) used to classify metastable basins for catalytically permissive (EI) and catalytically nonpermissive (EI*) states. The EI basin was defined as hydrogen bonds between the displayed atom pairs (yellow dashes). The EI* basin was defined as a lack of oxyanion hole and a distance > 8Å between 166 CD and 170 CG (orange dashes). Rendered in (C) is a projection of relative free energy onto a 2D plane defined by PCA of all pairwise heavy-atom distances within the binding-pocket. A representative trajectory between EI and EI* is plotted in black.

4.4.3 Analysis of the transition state controlling catalytic permissivity

Committor analysis showed two strongly-committed regions with a relatively broad region of moderate commitment between them (Figure 3a). This is consistent with the probability density projection from our initial simulations rendered in Figure 2c, which suggests a relative "plateau" of the free-energy surface between the two large metastable basins, although both the estimated free-energy surface and the committor values suggest that this intermediate region is far from uniform. As expected from the kinetic map analysis, the member of the transition state ensemble identified via committor analysis still showed the hydrogen bonding pattern that defines an oxyanion hole, confirming that loss of the oxyanion hole occurs after commitment to nonpermissivity in our simulations. Structural comparison of the catalytically permissive basin (EI) and the catalytically nonpermissive basin (EI*) showed movements in the SDN motif loop and the loop containing Trp105 away from the drug (Figure 3b). The member of the transition state ensemble was via gross analysis structurally intermediate between EI and EI*. Quantitative analysis and computational testing of the key protein conformational features controlling the EI to EI* transition of KPC-2 follows.

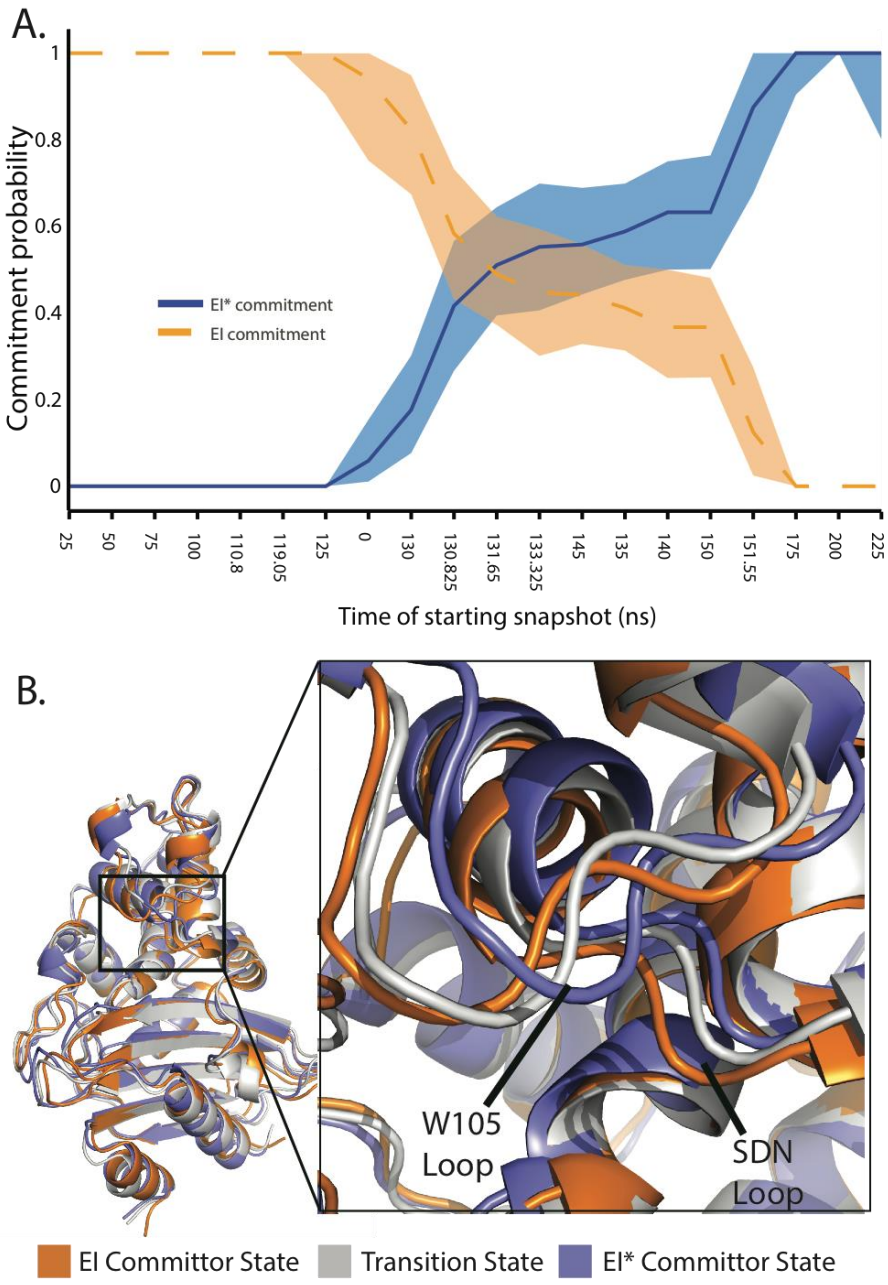

Figure 4.3 Committor values yield a reaction coordinate for catalytic permissivity and member of the transition-state ensemble

(A) Rendering of committor values through the transition region between EI and EI*, identifying a member of the transition state ensemble at 50% commitment. Shaded areas indicate bootstrapped 95% confidence intervals (B) Rendering of the transition state ensemble member and two structures that were EI-committed and EI*-committed (drug not shown). Protein conformational changes from EI to EI* include alterations in the loop containing W105 and the SDN loop. These residues then interact differently with the substrate, and the binding-pocket size increases (Figure 4.4b).

4.4.4 Protein conformational changes controlling catalytic permissivity

Because the KPC-2 transition between catalytically permissive and nonpermissive states is relatively complex, we used information-theoretic feature selection to identify a set of key protein conformational changes that control catalytic permissivity. We applied mRMR feature selection (see Methods) to rank independent interatomic distances that best differentiate conformations in the EI basin from those in the EI* basin (see Methods). We selected the top ten distances (Figure 4a; Table 4.1) and set up the following test to evaluate their effect. If biasing these distances towards EI-committed values reverses commitment to the EI* state and biasing these distances towards EI*-committed values reverses commitment to the EI state, then they can be considered to control catalytically permissive versus nonpermissive conformations. As shown in Figures 4c and 4d, rerunning committor calculations with these biases applied indeed reversed commitment, and since none of the distances involved either the drug or residues used to assess commitment, we conclude that these interatomic distances indeed control oxyanion hole stability and catalytic permissivity.

Since all of the key distances controlling catalytic permissivity increased between EI and EI* states, we hypothesized that some of the conformational changes involved in loss of catalytic permissivity might also affect the binding-pocket size. Indeed, the solvent-accessible surface area of the binding-pocket significantly increased from catalytically permissive states to nonpermissive states (Figure 4.4b), and the free-energy plateau region showed intermediate values. We thus conclude that loss of catalytic permissivity involves relaxation of the binding-pocket structure in ways that permits the beta-lactam substrate to lose proper orientation for hydrolysis.

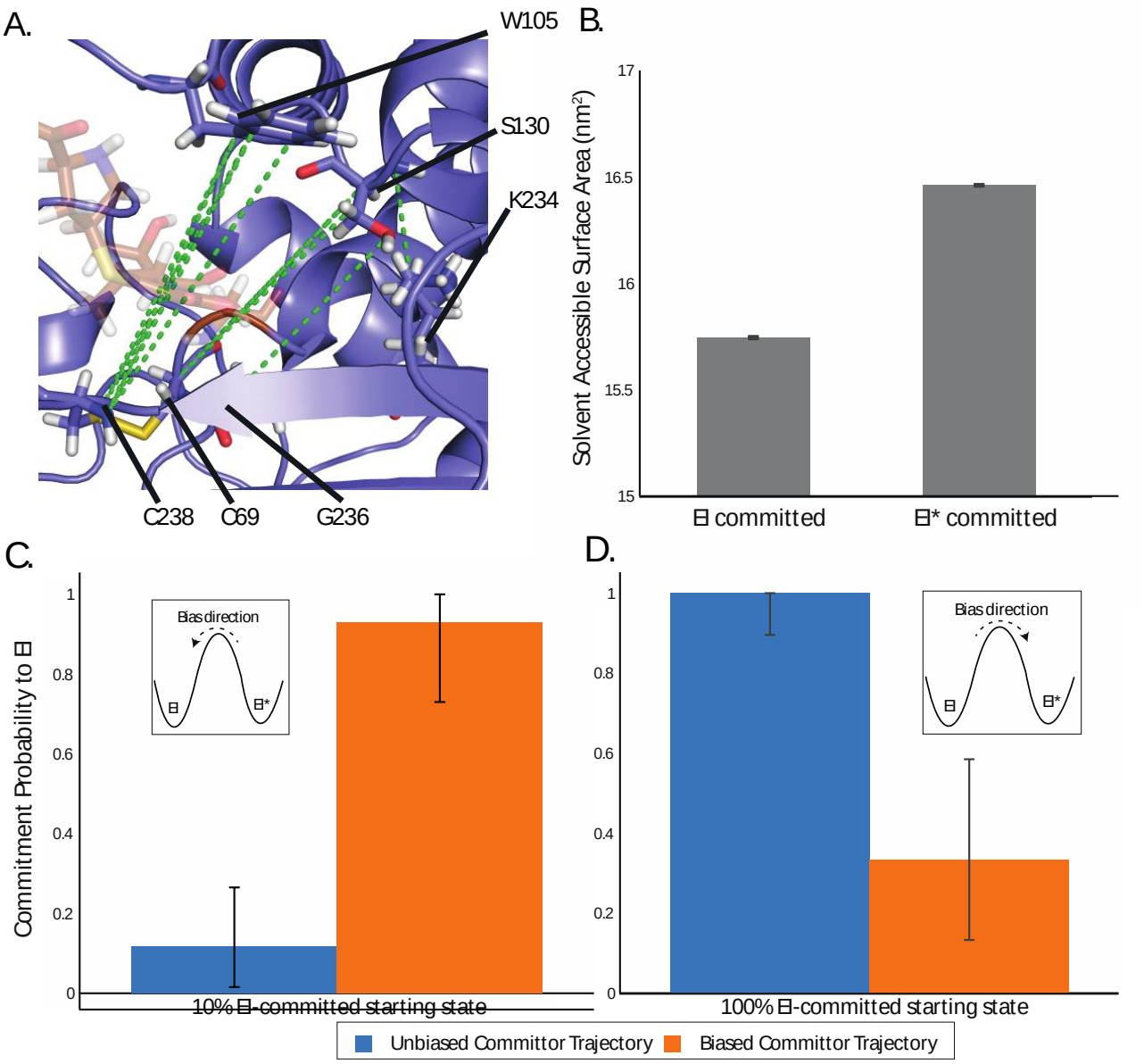

Figure 4.4 Identification and validation of conformational changes between permissive and non-permissive states.

(A) Molecular rendering of key distances that change between EI and EI* states identified by information-theoretic feature selection. (B) Solvent accessible surface area for the ligand-binding-pocket plotted for conformations in the EI permissive state, the EI* nonpermissive state, and states on the free-energy plateau between. Pocket surface area increases significantly from EI to EI* conformations ($p<.0001$ via 2-sample Kolmogorov-Smirnov test). (C,D) Biases on key distances control commitment to EI vs. EI* states. Control of catalytic permissivity by these key distances was validated by selecting starting conformations on either side of the free-energy barrier between EI and EI* and then running MD simulations biased towards the opposite state via restraints on the identified distances. In each case, the applied bias significantly altered commitment compared to an unbiased set of trajectories. Error bars in all plots indicate 95% confidence intervals calculated via bootstrap.

Atom pair	MI Score (relevance portion of mRMR)	Mean EI-committed distance (nm)	Mean EI*-committed distance (nm)
TRP 105 CE2 - CYS 238 N	.545	1.14	1.34
SER 130 N - LYS 234 CE	.090	.50	.53
TRP 105 CG - CYS 238 SG	.541	1.26	1.46
SER 130 OG - GLY 236 C	.500	.712	.854
TRP 105 CD2 - CYS 238 SG	.539	1.33	1.54
CYS 69 CA - SER 130 CA	.527	1.012	1.17
TRP 105 CD2 - CYS 238 N	.536	1.12	1.32
CYS 69 C - SER 130 CA	.521	.88	1.03
TRP 105 CG - CYS 238 N	.540	1.07	1.26
CYS 69 CA - SER 130 N	.520	1.14	1.30

Table 4.1 Top 10 protein-protein atomic distances that distinguish catalytically permissive and nonpermissive states.
Distances were chosen based on iterative mRMR, which balances the MI score against redundancy with previously selected distances. Average distance values are listed for all conformations with >80% imputed commitment to EI or EI* states respectively.

4.4.5 Testing mutants of key residues controlling permissivity

More specifically, all ten distances controlling the KPC-2 acyl-enzyme conformational change involved either Ser130 or Trp105. Ser130 hydrogen-bonds with the meropenem thiazolidine ring, while Trp105 extensively contacts the ring in catalytically permissive conformations (Figure 4.5). To test the importance of these residues and their interactions with the rest of the binding-pocket in controlling carbapenem hydrolysis by KPC-2, we simulated wild-type KPC-2 and four Trp105 mutants that had been characterized experimentally: W105F, W105N, W105V, and W105L [64]. Since occupancy of the catalytically permissive state should correlate with k_{cat}, we measured the time-autocorrelation function of the catalytically permissive state in our simulations and compared it with the imipenem k_{cat} values measured experimentally (Figure 4.6). We observe a Pearson correlation coefficient of 0.95 between calculated EI-state lifetimes and experimental k_{cat} values, suggesting that the EI-to-EI* forward rates vary between mutants more than the reverse rates, and thus the EI-state lifetime controls the equilibrium constant between these two states. The strong linear correlation with k_{cat} values further suggests that Trp105 may indeed control transitions between catalytically permissive and nonpermissive states and thence k_{cat} values and carbapenem drug resistance.

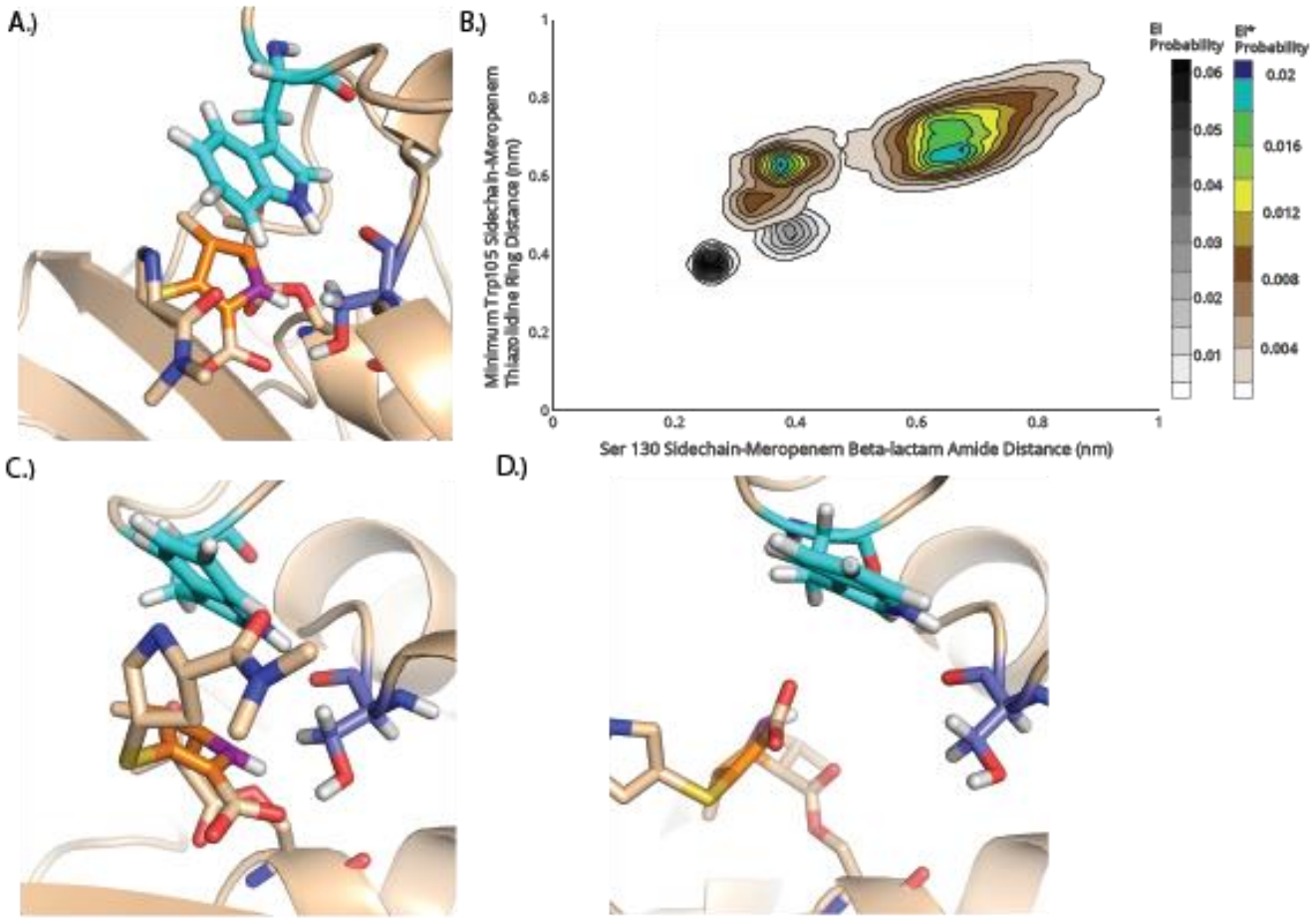

Figure 4.5 Trp105 and Ser130 interact with the meropenem thiazolidine ring in the catalytically permissive state but not the nonpermissive state

(A) In catalytically permissive conformations, Trp105 (cyan) interacts with the thiazolidine ring (orange) through Van der Waals interactions while Ser130 (violet) hydrogen bonds with the amide (fuscia) on the ring and carboxylic group on the thiazolidine ring. These interactions are quantified for both sets of conformations in (B). In catalytically nonpermissive conformations (C,D) both hydrogen bonding between Ser130 and the drug and Van der Waals contacts between Trp105 and the drug are lost.

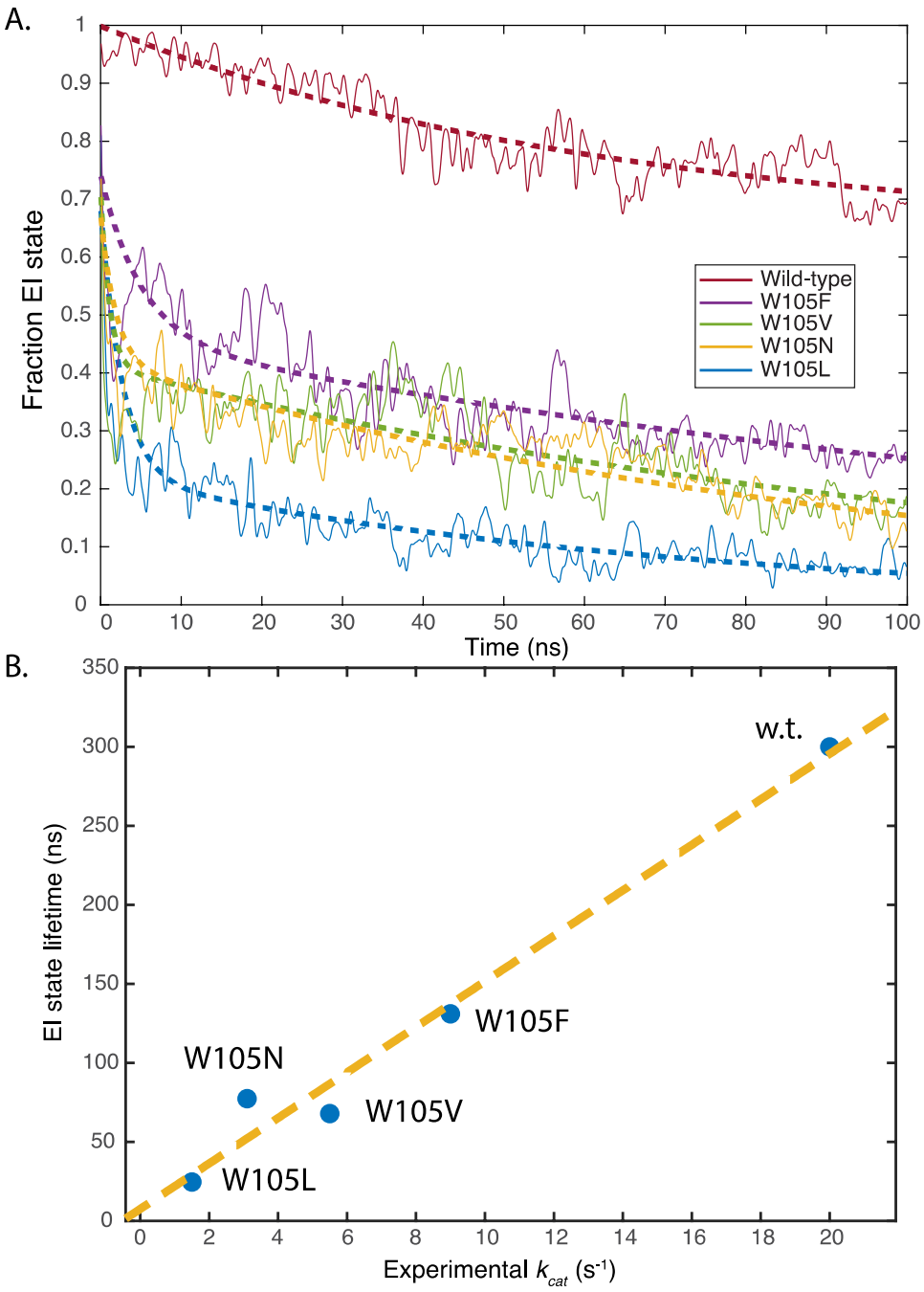

Figure 4.6 Trp105 mutants with reduced k_{cat} values show corresponding reduced lifetime in the catalytically permissive acyl intermediate state.
(A) Probability of remaining in catalytically permissive state calculated from simulations of Trp105 mutants. (B) Lifetime of catalytically permissive state (EI) in each set of mutant simulations is plotted against the corresponding imipenem k_{cat} value. Dashed lines indicate fits (double-exponential for lifetimes, linear for lifetime-k_{cat} relationships). The Pearson correlation coefficient is 0.95.

4.5 Chapter Conclusions

The acyl-enzyme intermediate of KPC-2 is critically important in differentiating this carbapenemase from less-resistant beta-lactamases. Prior work has suggested that the conformational equilibria of this acyl-enzyme state may determine kcat, but a detailed molecular explanation for this has thus far been lacking. Here, we have used classical molecular dynamics simulations of the acyl-enzyme intermediate and committor analysis to analyze slow conformational changes between a catalytically poised substate of the acyl-enzyme intermediate and one that lacks key features for catalysis. The changes we identify to the ligand-binding-pocket, specifically interactions of Ser130 and Trp105, appear critical in positioning the carbapenem drug for hydrolysis. Knowledge of these key conformational changes will now permit better prediction of drug-resistance mutants of KPC-2 and potentially other highly resistant beta-lactamases. It also provides a starting point for the computational evaluation of new small-molecule inhibitors for this beta-lactamase that is the most common cause of carbapenem-resistant infections in the United States.

Chapter 5. Dissertation Discussion and Future Directions

5.1 Dissertation Discussion

In this work, I have presented three approaches to understanding residues and interactions that control beta-lactamase function and subsequently antibiotic resistance. In this section, I will discuss the impact and relevance of some of our observations and approaches.

5.1.1 Significance of prediction of allosteric residues which affect function

The most direct application from our work for predicting future antibiotic resistance involves the two developed approaches that identify functionally important residues or mutations. The first method (Chapter 2) measures the strength of the association of a residue to the pocket. The second (Chapter 3 and Chapter 4) predicts the effect of a *specific* mutation on beta-lactamase function. In the future, these two prediction techniques could guide wet lab experiments or aid drug design that attempts to avoid future resistance.

Our first developed approach maps the strength of the association of every residue site back to the enzyme binding-pocket and lends itself to potential clinical applications that need rapid analysis of newly discovered mutations. We have shown that this approach applied to CTX-M9 identifies residue sites that, when mutated, have large effects on function along with residue sites that have little or no effect on function (Chapter 2). One benefit of this approach is that the resulting data contains a pairwise measure of association between all residues. This is useful for applications that require pre-computed data such as those that might rapidly query the potential functional importance of several residues. With the rise of rapid bench top and bedside genetic sequencing, one could envision a scenario where this approach aids a clinical team that has identified a novel mutation in a beta-lactamase carried in an infection. With these infections, clinicians usually need

to act quickly and cultures and resistance testing takes at least 24 hours [188]. Therefore, this tool could provide a preliminary assessment during this time as to whether the resistance of this new beta-lactamase may be altered from wild-type in this infection. A mutation at a residue with a low association to the pocket could indicate that current treatment protocols could be effective. There are limitations to this application. First, a mutation to a highly associated residue could indicate either a potential decrease or increase of resistance and, therefore, is less useful. Second, such an approach, would not consider other mechanisms of resistance within an infection.

Our second developed mutation prediction approach models the effects of a specific mutation which could improve drug development by identifying high-yield mutations to test for resistance which could aid drug development. This approach carries higher computational costs as molecular dynamic simulations are performed for each queried mutation instead of wild-type simulations as done in our first approach. The benefit of this increased cost is that this provides clearer information as to the effect of a mutation. Furthermore, computational power is rapidly increasing making this approach more feasible in the future [189]. The application of the prediction of specific mutations on beta-lactamase resistance and spectrum could greatly aid drug development. The likelihood of resistance to a new beta-lactam antibiotic affects its potential economic success and clinical usefulness. Therefore, a tool that can predict resistance computationally could integrate into a pre-synthesis drug development pipeline aiding in the decision to synthesize and further test a compound. This would speed this process and produce candidate compounds with a higher likelihood of commercial and clinical success.

5.1.2 Insights from protein-wide mapping of allosteric networks

In our pairwise characterization of the motional associations of residues in CTX-M9 (Chapter 2), we developed an “allosteric network”, which simplifies complex multidimensional

simulation data in order to provide an overview of the dynamic relationships across an enzyme. In our work, this network provides a description of how different regions of a beta-lactamase may interact and insight into the machinery that supports its function. A key strength in the development of this network is the use of mutual information and its identification of associations regardless of the means of communication. In practice, analyzing molecular dynamics simulations for allosteric interactions is difficult because the signals are noisy and multidimensional [94]. Mutual information simplifies this through the measure of linear and non-linear associations. Comparisons since our analysis have found that mutual information on molecular dynamics simulations captures more biologically relevant interactions than linear based methods such as correlation [94]. Furthermore, mutual information identifies associations between two residues regardless of how the interaction transmits. Therefore, it captures interactions between residues communicated by direct and diffuse mechanisms.

5.2 Future Directions

In this dissertation, we have developed methods to characterize determinants of beta-lactamase activity. These methods offer several possibilities for further work in understanding antibiotic resistance. Here, I propose three potential directions:

(1) Refining predictions of mutant effects on function

(2) Characterizing novel beta-lactamase inhibitor resistance in KPC

(3) Characterizing closely linked residue sub-networks

5.2.1 Refining predictions of mutant effects on function

In this dissertation, we developed an approach for predicting the functional effects of mutations to beta-lactamases using two complementary methods. The first method (see Chapter 3)

involved large-scale prediction of allosteric point mutations on enzyme function in a non-carbapenemase, CTX-M9, using an intra-pocket distance metric. The second method (see Chapter 4) employed a more sophisticated conformational approach to predict the effect of mutations on k_{cat} in a carbapenemase, KPC-2. However, this method focused on only one binding-pocket residue and allosteric residues have been shown to affect these enzymes (see Introduction). It would, therefore, be valuable to, first, expand the predictions of k_{cat} from modulation of off-pathway exchange kinetics to include allosteric locations in KPC-2 and, second, to apply the improved kinetic prediction method from Chapter 4 to CTX-M9 to identify mutations that might grant carbapenemase activity.

2.5.1a Predicting effects of allosteric mutations on KPC-2 function

Initial work predicting the effect of mutations on k_{cat} in KPC-2 (Chapter 4) measured how binding-pocket mutations altered a conformational transition. While the methods successfully predicted the change in activity, there was a direct Van-der-Waals interaction between the mutated residue, Trp105, and meropenem (Figure 4.5). From studies of variants of KPC, it is clear that allosteric mutations can also affect KPC k_{cat} values [59–63]. Therefore, I now wish to use this transition-based method to predict the effects of mutations to residues that have no direct interaction with the drug. A successful implementation of this expanded approach would allow me to characterize allosteric residues that support carbapenemase activity which would aid in understanding how KPC-2 provides resistance to carbapenems.

A first step to achieving this goal would involve predicting the effects of second shell mutations on function. Second shell residues are defined as residues which have no direct interactions with the drug but do interact with binding-pocket residues [190]. Second shell residues offer an intermediate step in expanding this method to allosteric mutations as these residues are

one interaction removed from direct interaction with the ligand. Furthermore, the effect of mutations to many of these residues in KPC-2 has been studied and kinetically characterized, providing existing k_{cat} values for comparison [66]. A more ambitious subsequent step would involve predicting the effects of allosteric mutations beyond the second shell. This approach would first utilize allosteric KPC mutations that have already been kinetically characterized [191]. Resulting alterations to this transition would then be compared to reported k_{cat} kinetics.

Next, I would perform novel mutation prediction in a manner similar to the mutant screening simulations employed in Chapter 3 but with the oxyanion hole metric replaced by measuring how mutations affect the lifetime of the catalytically competent state. While computationally expensive and requiring subsequent experimental construction and verification of novel mutations, screening for novel mutations that would affect carbapenemase activity in KPC-2 would yield a better understanding of the mechanisms of this enzyme and how it might mutate in the future. I hypothesize that mutations which decrease catalytically favorable state stability would have similar reductions in k_{cat}.

2.5.1b Granting carbapenemase function to CTX-M9

Another future direction would be understanding the determinants of spectrum in different classes of beta-lactams. This would provide a tool for predicting how a beta-lactamase may acquire full resistance to a previously effective class such as carbapenems. Specifically, identifying mutations that would confer carbapenemase activity to CTX-M9 offers the most useful first step since it could aid further drug development of carbapenems and other beta-lactam antibiotics.

An initial goal with the work in CTX-M9 (Chapter 3) was to identify allosteric residues which might grant carbapenemase activity to CTX-M9. However, the initial distance-based metric failed to do so in meropenem simulations, suggesting that other properties of the active site, beyond those considered, affected spectrum. Subsequent work with KPC-2 (Chapter 4) resulted in a better approach to predict mutations that alter resistance by observing a mutation's effect on an off-pathway conformational transition. Based on our work and characterization of CTX-M9 with meropenem, the acyl-enzyme of CTX-M9:meropenem may undergo a similar conformational transition like KPC-2 but with a highly favorable off-pathway intermediate and highly unfavorable on-pathway intermediate. Therefore, I propose that mutations which alter CTX-M9:meropenem's conformational transition to make on-pathway conformations more favorable may grant carbapenemase function to this non-carbapenemase.

Before screening this possible pathway, one must ensure that catalytically favorable conformations in KPC-2 according to existing criteria are rare in CTX-M9 simulations. CTX-M9's and KPC-2's binding-pocket residues closely match each other (Figure 5.1). This means that the definitions developed to identify catalytically favorable states for KPC-2 with meropenem could apply to CTX-M9. If these definitions are accurate, defined favorable conformations seen in KPC-2:meropenem simulations should be rare in CTX-M9:meropenem simulations, as CTX-M9 is unable to hydrolyze and release meropenem [27]. To confirm this, CTX-M9:meropenem

simulations of wild-type and mutants with high oxyanion hole favorability would be started in a conformation meeting this favorable definition. If the catalytically favorable state's lifetime matches that of KPC-2:meropenem, this would indicate that a different definition is needed to describe specific conformations favorable for carbapenemase activity.

To narrow this definition, conformational co-clustering of CTX-M9 and KPC-2 pockets could identify conformations specific to KPC-2:meropenem and therefore, potentially ones responsible for carbapenemase activity. Specifically, clusters that contain conformations exclusive to KPC-2 that match prior definitions for catalytic favorability would designate conformations aiding carbapenemase activity (Figure 5.2A).

Once the definition of catalytically favorable conformations for carbapenemase activity has been established, CTX-M9 can be screened for mutations that increase the favorability of this conformation. From Chapter 2, CTX-M9 mutant work suggests that major changes to carbapenemase activity likely require multiple mutations. Therefore, a multiple mutation screening approach would need to be developed. These approaches are very difficult because the combinatorial space of possible mutations is extremely large. Genetic algorithms offer a potential multiple mutation approach for CTX-M9. These algorithms have been successfully used in fields to design solutions where all possible solutions cannot be fully constructed and compared [192,193]. These algorithms employ a greedy approach where the algorithm evaluates a series of candidates and selects the best result (the definition of "best" varies by problem). This is an iterative process where the remaining candidates are evaluated with that selected change and the best result taken; each iteration adds one additional change.

For CTX-M9, a genetic algorithm would build a multi-mutant. It would begin with an initial screen of all possible point mutants; likely using swap point mutants with KPC as before.

There are two potential measures to assess a "best performing mutation." The first would evaluate simulations for conformations which meet the catalytically favorable definition or, if none meet it, have the closest root-mean squared distance to this conformation. The second would to start these simulations in this catalytically favorable state and measure the lifetime of the state (see Chapter 4), then select the mutation with the highest persistence time in this state. In a subsequent round, double mutants would be evaluated where all mutants have the best performing mutant of the previous round and one additional point mutation (Figure 5.2B). This would continue until either of these two evaluations meet a certain tolerance to KPC-2 simulations (Figure 5.2B).

A genetic algorithm does carry potential complications with CTX-M9. Mutations in these enzymes often demonstrate sign epistasis [85]. Therefore, there could exist a mutational set that grants carbapenemase activity with n mutations but performs poorly with n-1 mutations. A canonical genetic algorithm would never arrive at this solution because the algorithm would never select the n^{th}-1 set needed at the n^{th} round. Therefore, this algorithm could be augmented with a Monte Carlo approach where the "best" mutation is selected with some probability related to its performance in the previous round. This introduces a degree of randomness that would avoid assuming that all mutations would be additive. Ultimately, this approach could be easily automated and permits sampling of a multi-mutational space to grant CTX-M9 carbapenemase activity.

In addition to a genetic algorithm, chimeric approaches offer alternative experimental approaches to identifying multiple mutations which might change spectrum. These approaches replace sections of the target beta-lactamase, CTX-M9, with the corresponding section from the beta-lactamase of desired spectrum, such as KPC-2. For CTX-M9, I would replace key catalytic loops around the pocket such as the omega loop. These mutants would then be tested for activity and, if carbapenemase activity is identified, amino acids would be randomly reverted back and

these mutants tested or refined with directed evolution. This approach has been employed in other beta-lactamases to successfully aid directed evolution [84,194]. The downside of this approach is that such structural replacement in the protein could eliminate all drug activity through changes to pocket structure or stability producing an un-evolvable mutant.

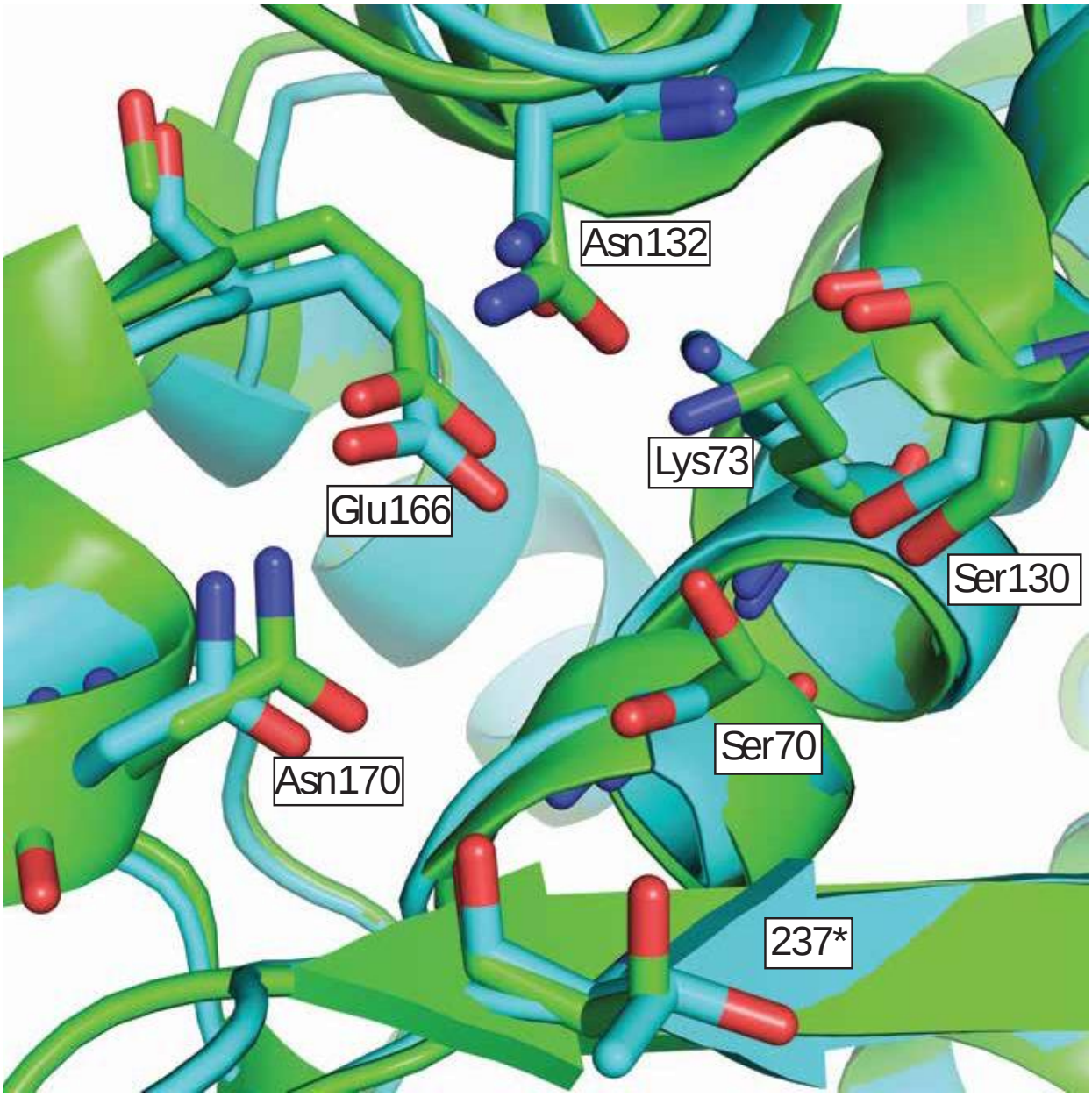

Figure 5.1 Comparison of KPC-2 and CTX-M9 binding-pocket
Crystal structure comparison of KPC-2 (PDB 2OV5) and CTX-M9 (PDB 2P74) demonstrates that major catalytic residues are conserved [37,41]. Structures suggest that catalytically favorable conformational definitions for KPC-2 could quickly translate to CTX-M9. It would be expected that such a conformation would be short lived in CTX-M9:meropenem.

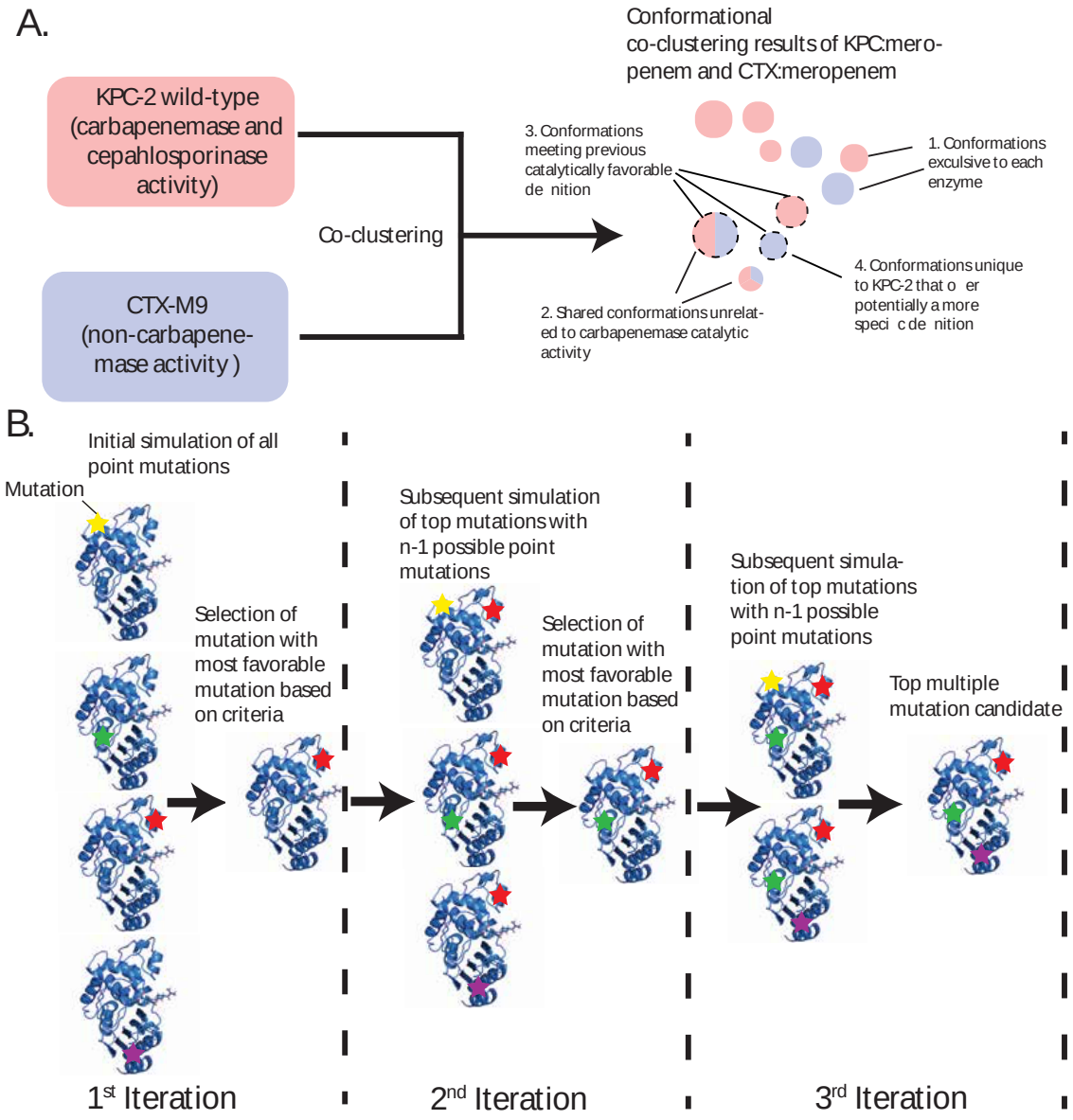

Figure 5.2 Diagram of co-clustering and genetic algorithms
(A) Simulations are performed of both KPC-2 and CTX-M9. Pocket conformations are then co-clustered using a clustering algorithm (such as K-centers). Single clusters will consist of populations with similar structural conformations. Of these, there will be individual clusters that heavily weight one enzyme versus the other indicating unique conformations to that enzyme. New states unique to KPC-2 and satisfying, prior catalytic definitions likely represent potentially more specific conformations conducive to carbapenemase activity compared to CTX-M9 (4).
(B) Simple example of a genetic algorithm for screening four possible mutations. The algorithm runs a series of simulations and then selects the top mutation. It then runs a series of double mutants simulations with this mutation and the remaining set. Each iteration reduces the possible mutations to test and develops a multi-mutant. In reality, this could employ cut-off criteria to stop iterations before all mutations are tested (not shown). Additionally, the criteria used would identify mutants that are showing favorable carbapenemase conformations, as discussed in the text.

5.2.2 Characterizing novel beta-lactamase inhibitor resistance in KPC

New inhibitors offer a strategy in treating KPC-2 carrying infections but often lose efficacy due to novel mutations which grant KPC-2 resistance to these inhibitors [58]. It is not understood how these mutations grant resistance to these inhibitors. In Chapter 4, we characterized an off-pathway conformational transition in the acyl enzyme state of KPC-2. One hypothesis is that beta-lactamase inhibitors function by increasing the favorability of similar off-pathway conformations. Therefore, the methods developed to study off-pathway transitions with KPC:meropenem are well suited to characterized KPC-2's interaction with an inhibitor and understand how novel mutations avoid inhibition. Understanding this interaction would aid in the design of future inhibitors.

Avibactam is the first beta-lactamase inhibitor effective against KPC [195,196]. It works by lowering the minimum inhibitory concentration of a co-delivered normally susceptible beta-lactam [44]. Avibactam is thought to preserve beta-lactam periplasmic concentrations by preventing the hydrolysis of susceptible drugs through competitive competition for the beta-lactamase's binding-pocket [58]. Resistance to avibactam has arisen in KPC mutant enzymes. Currently, most mutations appear in the binding-pocket and second shell, but the combinations of mutations that confer resistance vary [58,197,198]. As a result, there is great interest in understanding how KPC-2 evades this new inhibitor.

Current research suggests that resistant variants of KPC hydrolyze avibactam in ways that are similar to KPC-2 with meropenem (Figure 5.3) and that wild-type KPC with avibactam demonstrates conformations similar to off-pathway conformations with meropenem. Therefore, methods and findings from our study of KPC-2 and meropenem would likely translate to this system and could be used to understand how KPC-2 gains resistance to this inhibitor. Despite its interaction with KPC-2, avibactam is a non-beta-lactam beta-lactamase inhibitor with a bridged

diazabicyclooctane chemical structure (Figure 5.3) [58]. Chemically, avibactam and KPC-2 form stable acyl-enzymes, suggesting that acylation of KPC-2 occurs faster than deacylation [199]. The deacylation step has been measured with a k_{off} of 1.4 x 10^{-4} s^{-1} with a deacylation half time of 82 minutes [200]. This means that KPC-2:avibactam largely exists in the acyl-enzyme form (Figure 5.3). KPC-2's co-crystalized structure with avibactam matches binding-pocket off-pathway conformations of KPC-2:meropenem (RMSD .9Å) and demonstrates a large displacement of Trp105 as compared to the catalytically permissive states of KPC-2 and the KPC-2 crystal structure (Figure 5.4). Based on this information, I hypothesize that KPC-2 and avibactam likely undergo a conformational off-pathway transition in the acyl-enzyme state that is conformationally similar to that with meropenem. As a future direction, I would identify catalytically favorable states in the pocket with avibactam as compared to KPC wild-type and then predict the effect of these mutations and others on potential avibactam activity.

Characterization of the conformational differences between KPC and avibactam-resistant KPC variants provides critical insight into how KPC increases its hydrolytic rate of avibactam to gain resistance. Molecular dynamics simulations offer a means to identify these differences. Specifically, simulations of both types of KPC with avibactam would undergo conformational clustering of the binding-pocket to identify conformations unique to the mutants. This approach is similar to the approach proposed for KPC-2 and CTX-M9 (Figure 5.2A). Clusters unique to avibactam resistant mutants likely represent conformations that promote catalytic activity. I can use our past understanding of catalytic conformations in KPC-2 to further refine these. The conformations unique to resistant mutants could provide useful information about the pocket interactions that support hydrolysis of avibactam and guide future drug development.

Next, these conformations could serve as the basis to predict other mutations which could grant similar avibactam resistance. As with the Trp105 mutants in Chapter 4, other KPC-2:avibactam mutants could be started in these catalytically favorable conformations and the stability of these interactions measured as a surrogate for avibactam activity. Mutants that stabilized this conformation more than wild-type might confer resistance and are candidates for experimental testing. If multiple mutations are required, the previously discussed genetic algorithm approach could be employed. A successful prediction of mutations that cause avibactam resistance would aid in characterizing the avibactam resistance landscape and highlight potential future mutations that could confer resistance.

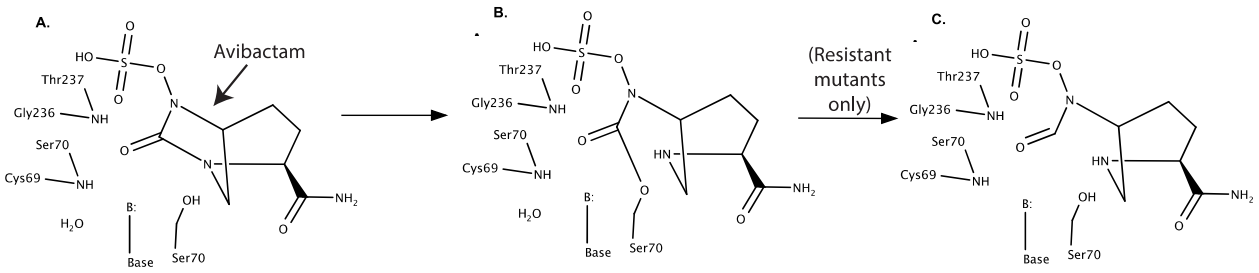

Figure 5.3 Postulated avibactam hydrolysis reaction
Avibactam binds (A) and forms an acyl-enzyme (B) with KPC-2 similar to meropenem (Figure 1.2). In mutants that confer resistance to avibactam, it is also thought to undergo a similar form of hydrolysis (C). At this time, the transition state following the acyl-enzyme has not been characterized (B/C).

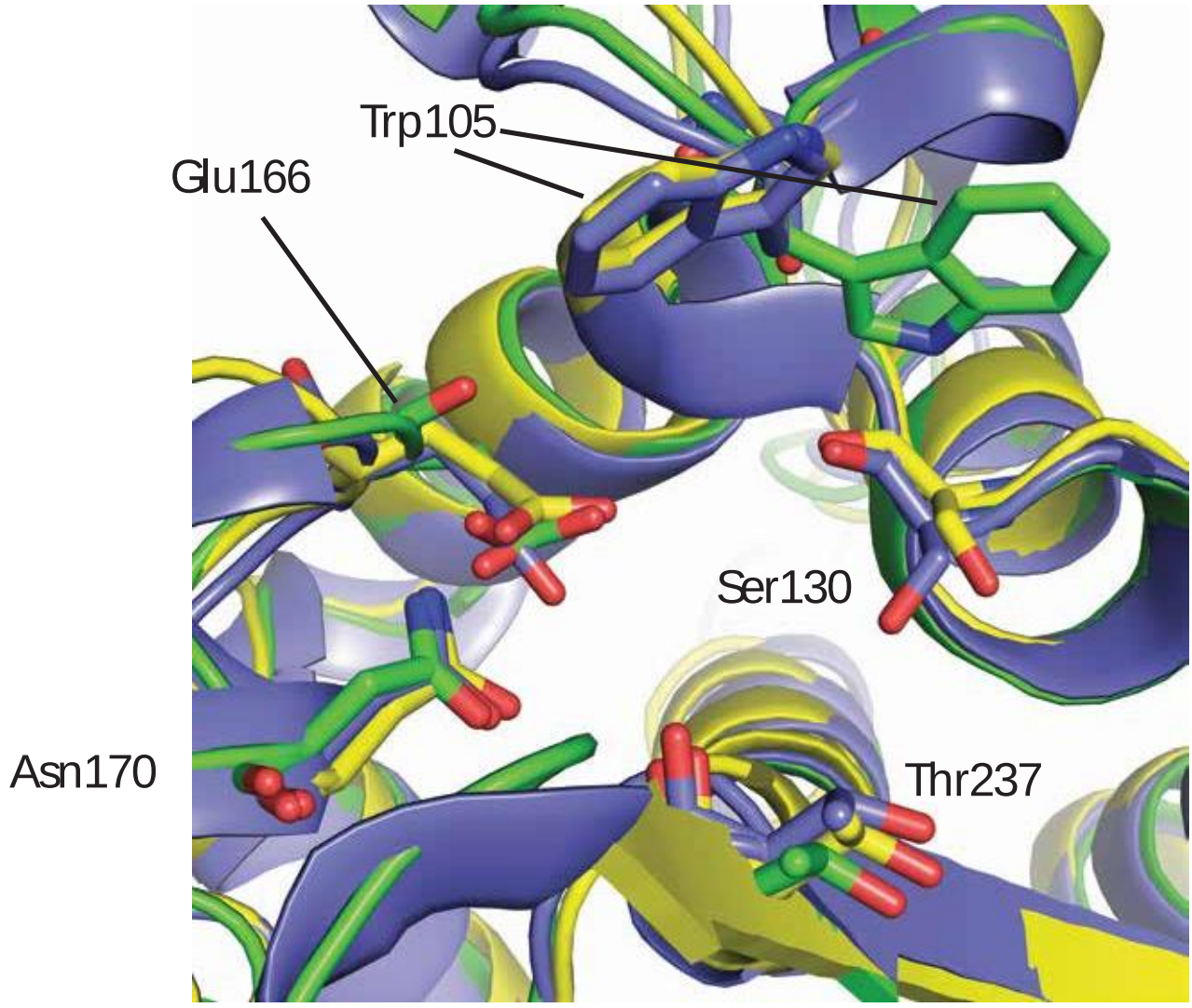

Figure 5.4 KPC-2 off-pathway conformations demonstrate similar binding-pocket conformations to avibactam crystal structure
KPC-2 off-pathway conformations from molecular dynamic simulations (yellow) (PDB 2P74) demonstrate similar binding-pocket conformations to the avibactam crystal structure (violet) (PDB 4ZBE) [41,199]. This conformation is most notable by the displacement of Trp105 as compared to catalytically favorable conformations (green).

5.2.3 Characterizing closely linked residue sub-networks

I can extend approaches in Chapter 2 to identify functionally related groups of residues beyond the pocket in beta-lactamases which could aid in identifying multiple mutations that support enzyme stability or allow for comparison between diverse beta-lactamase families. In this chapter, we developed a method to measure the dynamic atom-to-atom associations across a beta-lactamase. Atoms which have greater association have a higher score in this network. This structure is analogous to graphs. Therefore, algorithms developed from graph theory are highly applicable especially community or cluster identification algorithms [201,202]. Community or cluster algorithms identify highly connected components within a network. In beta-lactamases, each identified cluster, especially those associated with pocket mutations, could represent a group of residues which interact and function together [201–203]. An identified cluster provides information about a possible group of residues that support function or stability or insight about the residue-interaction patterns of the beta-lactamase which could serve as means to compare families of different spectrums.

A common algorithm to identify clusters in biological networks uses hierarchical clustering [204,205]. In this approach, all associations are converted into a distance metric where high association is represented as a small distance and low association represented as a large distance. One can then perform a hierarchical clustering to group residues based on this distance matrix [206]. The resulting dendrogram encodes clusters at various strengths of association. From this dendrogram, one can then choose an association cut-off to select clusters. There are advanced approaches such as weighted correlation network analysis which employ a branch variable height cut-off that considers the underlying network and dendrogram structure [203]. Such approaches

have been used in imaging and gene-coexpression networks and may more accurately identify clusters [203,207,208].

Identified clusters offer potential residues that may need to be co-mutated along with an initial targeted residue to maintain protein function. Our methods in simulation-based mutation prediction focus on the effect of an allosteric mutation on the pocket. These predictions do not take into account the effect of these mutations on stability or other aspects of the protein. As a result, created point mutations could result in a non-functional protein due to changes in the stability of the enzyme. In this case, co-mutating a targeted residue's cluster could potentially rescue function by restoring a group of residue interactions necessary for stability.

Clusters also provide a measure of differences in dynamic interactions between beta-lactamases of drug spectrums. Beta-lactamases from different families have diverse sequences and spectrums but demonstrate similar pocket structure and residues [24]. It is not understood whether these structurally similar but evolutionarily distinct enzymes have similar dynamic interactions across the protein and how these change with alterations to drug spectrum. Comparing clusters between families of different spectrums provides information on changes in residue interactions within the enzyme as it relates to function. Specifically, this would be done by performing simulations of different types of beta-lactamases from different families and calculating the clusters for each beta-lactamase. The difference in clusters could then be quantified by identifying the intersecting and different members of each homologous cluster. Clusters that are shared within members of a family but not between members of different families could identify spectrum related interactions. These interactions could further be studied by mapping the allosteric network to the enzyme structure or creating experimental mutants for resistance testing and structural study.

Identifying these unique clusters offers potential regions of the enzyme to further investigate in order to understand how dynamics corresponds to drug spectrum.

Chapter 6. Conclusion

Understanding mutations and interactions in beta-lactamases which govern function and spectrum is important for the development of future drugs and other strategies to avoid resistance. However, this is challenging due to the influence of allosteric interactions on function. Through three studies, we have identified allosteric residues and biochemical interactions which alter the function of key clinical beta-lactamases. Specifically, in this work, we have mapped allosteric networks that support function, identified resistance enhancing allosteric mutations, and identified a key conformational transition that offers a novel potential target against beta-lactamase resistance. The approaches used have the potential to be adapted to other beta-lactamases to further characterize resistance. In the future, they could increase our understanding of novel mutations and speed response to new resistance in both clinical and pharmacological settings.

Appendix A. Supplementary Methods for Chapter 3

Enzyme kinetics.

Chemicals used are as follows: kanamycin and chloramphenicol were purchased from Fisher Scientific. Nitrocefin was purchased from EMD Millipore (Billerica, MA) and Biovision (Milpitas, CA.) and dissolved in DMSO to form a 10 mM stock solution; any additional dilutions were performed in potassium phosphate saline buffer (pH 7.4). Meropenem sodium carbonate was purchased from LKT laboratories (St. Paul, MN) and used without further purification.

For all kinetic and structural studies, *bla*-CTX-M9 mutants were transformed into the *E.coli* expression strain *BL21-CodonPlus (DE3)-RIPL* (gift of Zygmunt Derewenda). Single-colony stocks were used to inoculate 50 mL LB medium containing 30 mg/mL kanamycin and 34 mg/mL chloramphenicol for overnight growth at 37 °C. 4 ml of each resulting mixture was used to inoculate 2x 500ml TB (Terrific Broth) media containing 30 mg/mL kanamycin and 34 mg/mL chloramphenicol for growth at 37 °C, 220 rpm until OD_{600} measurements reached 1.4. Expression was induced with 0.1 mM isopropyl-b-D-thiogalactopyranoside, and cells were further grown overnight at 18 °C, 220 rpm.

Bacterial cultures were pelleted by centrifugation at 4000 rcf for 20 minutes, the pellets were resuspended in 200 mL ice-cold Sucrose-Tris buffer (pH 9.0) and shaken for 20 minutes at 4 °C. The mixture was centrifuged for 12 minutes at 10500 rcf, 4 °C. Periplasmic protein was then isolated as follows: cell pellets were resuspended in 200 mL 10 mM Tris/HCl pH 9.0, shaken for 20 minutes at 4 °C, centrifuged for 12 minutes at 10500 rcf, 4 °C, and the supernatant containing periplasm was transferred to a fresh tube. Periplasmic protein was precipitated with ammonium sulfate and resuspended in TEAA buffer (pH 7.4). After overnight dialysis, protein purified via anion exchange chromatography (HiTrap Q FF, GE Healthcare, Sweden), followed by size

exclusion chromatography (Superdex 75 10/300 GL, GE Healthcare, Sweden). Eluted protein was dialyzed in 100mM PBS buffer pH 7.4 at 4 °C. The protein concentration was estimated using both 260/280 nm absorbance ratios and BCA assays. Enzymatic purity was assessed by SDS-PAGE.

Steady-state hydrolysis kinetics were measured as follows: nitrocefin was mixed with CTX-M9 enzyme or the indicated mutant in 10mM PBS, pH 7.4 to a final concentration of 0.2 nM enzyme and 2-200 μM nitrocefin as indicated. Nitrocefin hydrolysis was measured using absorbance at 486 nm at 15 s intervals using a Spectramax reader (Molecular Devices, Sunnyvale, CA). Initial velocities were determined by linear fits to the first portion of each reaction, and K_M and k_{cat} values were determined by nonlinear fits of initial velocities as a function of substrate concentration. A change in absorbance at 486-490 nm indicates formation of the acyl intermediate or any later stage in nitrocefin hydrolysis and thus reports on [EI] + [EP] + [P]. Fits of initial velocity data to estimate K_M and k_{cat} incorporated data from at least two biological replicas per mutant per concentration.

Thermostability assays.

Protein melting temperatures were measured using a SYPRO orange thermostability assay (Life Technologies, Carlsbad, CA). Dye fluorescence was monitored continuously in a real time PCR machine (Bio-Rad, Hercules, CA). All measurements were carried out in 10 mM phosphate buffer saline (pH 7.4) with 40 μM protein for *apo* enzyme. The meropenem adduct with CTX-M9 was formed by mixing an enzyme to a final solution of 40 μM with 200 μM meropenem (aqueous stock solution). Enzyme-adduct mixture was incubated on ice for 10 minutes prior to measurement. All measurement runs were performed in 0.5°C increments from 20°C to 90°C. Melting

temperatures were determined as the greatest magnitude of the derivative of the observed fluorescence.

Structural studies.

Crystals of CTX-M enzymes mutants were grown by vapor diffusion using sitting drops at 21 °C over buffer. CTX-M9-T165W was crystallized by mixing an equilibration mixture of 0.7 M potassium phosphate, 18% PEG 3350, pH of 8.2 1µl with 1µl of enzyme at 5 mg/mL in 10 mM sodium phosphate pH 7.5 Crystals were harvested after 7 days. CTX-M9 L48A was crystallized by mixing 1.2 M potassium phosphate pH 8.2 1µl with 1µl of enzyme at 20 mg/ml in 10 mM sodium phosphate pH 7.5. Crystals were harvested after 30 days. CTX-M9 S281A was crystallized by mixing 0.6 M sodium phosphate buffer, 20% PEG 3350, pH 8.4 with 1µl of enzyme (24 mg/mL in 10 mM sodium phosphate pH 7.5). Crystals were harvested after 90 days and diffracted to 6 Å. Crystals were flash frozen in liquid nitrogen prior to data collection.

Data were collected at beamlines 22-ID (T165W) and 22-BM (L48A) at the Advanced Photon Source at 100 K. Reflections were indexed, integrated and scaled using X-ray Detector Software (XDS) for T165W and the HKL software package for L48A, followed by further processing with CCP4 [209]. Structures were solved by molecular replacement using Phaser [210] with chain A of the native CTX-M9 crystal as the starting model (PDB ID: 1YLJ). Rebuilding was performed in Coot [211] followed by refinement with isotropic B-factors using Refmac. Water, PEG, chloride and phosphate molecules were added manually by examination of the Fo-Fc and 2Fo-Fc electron density maps.

Simulation preparation and equilibration.

The acylated meropenem and cefotaxime structures of CTX-M9 wild-type were generated using rigid-body fitting as previously described[4] using the native CTX-M9 crystal structure 1YLJ

[120] as a starting model. Point mutations were modeled using MODELLER's automodel [212] method. Histidine tautomer choices were determined automatically by the GROMACS [123] pdb2gmx utility; active-site protonation states were determined using PROPKA [213], with the remainder automatically determined by GROMACS pdb2gmx. The protein was placed in an octahedral box with a minimum of 2nm separation between periodic images and energy-minimized for 500 steps of steepest-descent minimization in vacuum. The protein was then solvated with TIP3P water and 150 mM NaCl; deacylating waters were not placed manually but spontaneously took the appropriate position during simulation. After solvation, another 500 steps of energy minimization were performed followed by 50,000 steps of NVT equilibration with 2 fs timesteps prior to production simulation with identical settings but in an NPT ensemble using the velocity-rescaling thermostat [127] and Berendsen barostat. Velocities were randomly sampled at start from a Maxwell distribution. Pressure coupling was performed at 1 bar with a 10 ps relaxation constant and a compressibility of 10^{-4} bar^{-1}. Temperature coupling was performed at 37 ºC with a time constant of 10 ps. A direct-space cutoff of 1.2 nm was used for both van der Waals and electrostatic interactions, and long-range electrostatics were treated using Particle Mesh Ewald [128] with a grid spacing of 0.15 nm. Hydrogen bonds were constrained using LINCS [126].

Sequence analyses.

CTX-M family enzyme sequences were retrieved using previously curated accession numbers[12]. A second, broader sequence alignment was generated using the 500 sequences most closely related to CTX-M9 using a PHMMER search[13], discarding one that had a >50% length mismatch. Amino acid multiple sequence alignments were generated using MUSCLE[14]. Phylogenetically corrected sequence mutual information (MI_p) was computed using the APC correction detailed previously[15].

Rigidity analyses.

The KINARI software [214] was used to predict rigid clusters based on the crystal structures of wild-type CTX-M9 (2P74), L48A (5KMT), and T165W (5KMU) at 11 evenly-spaced cutoffs for hydrogen bonds and hydrophobic interactions, determined based on the highest and lowest interaction energies calculated by KINARI in the wild-type crystal structure. Each atom-atom interaction was assigned a rigidity score consisting of the number of rigid clusters in which the pair co-existed across all 11 cut-off levels. Residue-residue scores were computed as the sum of all component atom-atom rigidity scores, and the per-row maximum of resulting matrix was calculated to yield residues most strongly participating in rigid-body interactions for each crystal structure. A complementary analysis was performed using MSU ProFlex [215] : 11 evenly spaced energy cutoffs were again used, and the most stringent cutoff before breakup of the large rigid core was selected. To test the effect of side-chain interactions on the stability of this core, each non-Ala residue in CTX-M9 was computationally mutated to alanine using MODELLER [212], rigid cluster analysis was performed on the resulting set of mutant structures, and each residue was scored based on similarity between the predicted rigid cluster for its alanine point mutant and the wild-type structure.

Appendix B. Supplementary Methods for Chapter 4

Atoms and distances used for structural clustering.

Structural clustering was performed on the bound drug, binding-pocket residues, and other key substrate-interacting residues defined as follows: binding-pocket residues were defined as those with a heavy atom within 5Å of the beta-lactam drug core for more than 10% of snapshots in the initial 20x500ns simulation dataset. The additional substrate-interacting residues used were His219, Arg220, His 274, Lys234, and Glu276 [41,58,65,66]. Structural clustering for kinetic map

construction was performed using rigid-body alignment in Cartesian space. Imputation of committor values and feature selection was performed using all heavy-atom:heavy-atom pair distances among these residues.

Kinetic map analysis.

A kinetic map of the oxyanion-hole to non-oxyanion conformational transition was constructed by structurally and kinetically clustering the eight initial molecular dynamics trajectories that visited both states. Each trajectory **x** can then be expressed as a sequence of clusters rather than a sequence of conformations. Using an interval of 50 ps, we constructed a directed graph between clusters where W_{ij}, the edge weight between nodes *i* and *j*, is calculated as follows:

$$W_{ij} = Count(x(n) = i, x(n+1) = j) \,/\, Count(x(n)), \forall x, \forall n$$

for each trajectory x and time point n. This process of kinetic clustering and graph construction is similar to the construction of a Markov State Model, but because we simply analyze observed transitions rather than propagating the transition matrix in time, the sampling requirements are much less stringent. All 50 kinetic clusters (nodes in the graph) partitioned cleanly between oxyanion-hole and non-oxyanion-hole conformations (>95% non-oxyanion-hole or >90% oxyanion-hole). For visualization, all non-singleton oxyanion-hole nodes of the graph were plotted as well as all non-oxyanion-hole nodes connected to an oxyanion-hole node; the full graph is also given in Figure S2. One singleton node that contained oxyanion hole conformations but was connected only to a non-oxyanion-hole node; this node is shown only in Figure S2.

Visualization of KPC-2 conformational space.

The set of all pairwise distances defined above comprises 18,915 distances; singular value decomposition was employed to obtain an orthonormal basis set, and principal component analysis

was used to select a 148-dimensional projection that captured >99% of the variability between structural snapshots. Snapshots meeting the criteria for the EI or EI* states were completely separable by a hyperplane in the original 18,915-dimensional distance space determined via a support vector machine, suggesting that a reduced-dimension space should be able to capture differences between these states. A two-dimensional projection onto the largest principal components was used for visualization purposes only.

Imputation of committor values.

Because determining a committor value for a structural snapshot requires running 20-80 unbiased molecular dynamics simulations for >50 ns each, we determined values in this manner for 20 structural snapshots. In order to select conformational features associated with the transition between catalytically permissive and nonpermissive states, a larger dataset was desired. We thus imputed committor values for related structural snapshots as follows. K-centers clustering was performed in the 148-dimensional space described above space to yield 30,000 clusters that were then refined with three iterations of k-medoids clustering [216]. These fine clusters were grouped using hierarchical agglomerative clustering using a complete linkage criterion; this was thresholded to the minimum number of clusters that maintained separation between all 20 snapshots that had different "known" committor values. This yielded 27,486 clusters. "Known" committor values were then assigned to all snapshots sharing the same cluster; all clusters not containing a "known" committor value remained undetermined. This yielded 35,651 snapshots committed to EI and 4,448 snapshots committed to EI*. The EI* snapshots were upsampled via data duplication to yield a balanced dataset for feature selection.

Feature selection.

Greedy minimum-redundancy, maximum-relevance feature selection [159] was performed to identify the independent protein-protein distances in the ligand-binding-pocket most associated with the transition from catalytically permissive to nonpermissive states as follows. Structural snapshots labeled with imputed committor values of >80% EI or >80% EI* were assigned to those two classes C_{EI} and C_{EI*}, and the set of features used was $\{d\}$, the set of all distance pairs between non-hydrogen atoms in the KPC-2 binding-pocket. The mRMR statistic was calculated as:

$$mRMR_i = I(d_i; C) - \sum_j I(d_i; d_j)$$

where I(d_i; C) is the distance-pair:class mutual information and I(d_i; d_j) is the distance-pair:distance-pair mutual information summed over all selected distances. Histograms for mutual information were calculated with a fixed bin width of 0.5 Å. A greedy algorithm first proposed by Peng[159] was used to select the top 10 distance pairs that maximize this statistic.

Biased simulations.

Biased simulations were performed using a modified version of Gromacs implementing the minimal-biasing potential formulation [185]. A coupling constant (α) and update step (τ) of 10 and 20ps respectively were used.

References

1. Ventola CL. The Antibiotic Resistance Crisis. Pharm. Ther. 2015 Apr;40(4):277–283.

2. Costantine MM, Rahman M, Ghulmiyah L, Byers BD, Longo M, Wen T, Hankins GDV, Saade GR. Timing of perioperative antibiotics for cesarean delivery: a metaanalysis. Am. J. Obstet. Gynecol. 2008 Sep;199(3):301.e1-301.e6.

3. Bullock R, van Dellen JR, Ketelbey W, Reinach SG. A double-blind placebo-controlled trial of perioperative prophylactic antibiotics for elective neurosurgery. J. Neurosurg. 1988 Nov;69(5):687–691.

4. Piddock LJ. The crisis of no new antibiotics—what is the way forward? Lancet Infect. Dis. 2012 Mar;12(3):249–253.

5. Infectious Diseases Society of America (IDSA), Spellberg B, Blaser M, Guidos RJ, Boucher HW, Bradley JS, Eisenstein BI, Gerding D, Lynfield R, Reller LB, Rex J, Schwartz D, Septimus E, Tenover FC, Gilbert DN. Combating antimicrobial resistance: policy recommendations to save lives. Clin. Infect. Dis. Off. Publ. Infect. Dis. Soc. Am. 2011 May;52 Suppl 5:S397-428.

6. Carlet J, Collignon P, Goldmann D, Goossens H, Gyssens IC, Harbarth S, Jarlier V, Levy SB, N'Doye B, Pittet D, Richtmann R, Seto WH, van der Meer JW, Voss A. Society's failure to protect a precious resource: antibiotics. The Lancet 2011 Jul;378(9788):369–371.

7. Aminov RI. A Brief History of the Antibiotic Era: Lessons Learned and Challenges for the Future [Internet]. Front. Microbiol. 2010 Dec;1

8. Kong K-F, Schneper L, Mathee K. Beta-lactam Antibiotics: From Antibiosis to Resistance and Bacteriology. APMIS Acta Pathol. Microbiol. Immunol. Scand. 2010 Jan;118(1):1–36.

9. Fleming A. On the Antibacterial Action of Cultures of a Penicillium, with Special Reference to their Use in the Isolation of B. influenzæ. Br. J. Exp. Pathol. 1929 Jun;10(3):226–236.

10. Page MI. The mechanisms of reactions of .beta.-lactam antibiotics. Acc. Chem. Res. 1984 Apr;17(4):144–151.

11. Carbapenems - Infectious Diseases [Internet]. Merck Man. Prof. Ed. [date unknown];

12. Penicillins - Infectious Diseases [Internet]. Merck Man. Prof. Ed. [date unknown];

13. Cephalosporins - Infectious Diseases [Internet]. Merck Man. Prof. Ed. [date unknown];

14. Mandell LA, Wunderink RG, Anzueto A, Bartlett JG, Campbell GD, Dean NC, Dowell SF, File TM, Musher DM, Niederman MS, Torres A, Whitney CG, Infectious Diseases Society of America, American Thoracic Society. Infectious Diseases Society of America/American Thoracic Society consensus guidelines on the management of community-acquired

pneumonia in adults. Clin. Infect. Dis. Off. Publ. Infect. Dis. Soc. Am. 2007 Mar;44 Suppl 2:S27-72.

15. Pitout JD, Sanders CC, Sanders WE. Antimicrobial resistance with focus on beta-lactam resistance in gram-negative bacilli. Am. J. Med. 1997 Jul;103(1):51–59.

16. IQVIA Institute for Human Data Science. Medicines Use and Spending in the US: A Review of 2016 and Outlook to 2021. 2017.

17. Walsh C. Molecular mechanisms that confer antibacterial drug resistance. Nature 2000 Aug;406(6797):35021219.

18. LaPlante K, Cunha C, Morrill H, Rice L, Mylonakis E. Antimicrobial Stewardship: Principles and Practice. CABI; 2016.

19. Spratt BG, Cromie KD. Penicillin-binding proteins of gram-negative bacteria. Rev. Infect. Dis. 1988 Aug;10(4):699–711.

20. Lu WP, Kincaid E, Sun Y, Bauer MD. Kinetics of beta-lactam interactions with penicillin-susceptible and -resistant penicillin-binding protein 2x proteins from Streptococcus pneumoniae. Involvement of acylation and deacylation in beta-lactam resistance. J. Biol. Chem. 2001 Aug;276(34):31494–31501.

21. Knowles JR. Penicillin resistance: the chemistry of .beta.-lactamase inhibition. Acc. Chem. Res. 1985 Apr;18(4):97–104.

22. ANTIBIOTIC RESISTANCE THREATS in the United States, 2013 [Internet]. Centers for Disease Control and Prevention; 2013.

23. O'Neill J. Tackling Drug-Resistant Infections Globally: Final Report and Recommendations. Review on Antimicrobial Resistance; 2016.

24. Lee D, Das S, Dawson NL, Dobrijevic D, Ward J, Orengo C. Novel Computational Protocols for Functionally Classifying and Characterising Serine Beta-Lactamases. PLOS Comput. Biol. 2016 Jun;12(6):e1004926.

25. Moellering RCJ. NDM-1 — A Cause for Worldwide Concern. N. Engl. J. Med. 2010 Dec;363(25):2377–2379.

26. Blair JMA, Webber MA, Baylay AJ, Ogbolu DO, Piddock LJV. Molecular mechanisms of antibiotic resistance. Nat. Rev. Microbiol. 2015 Jan;13(1):42–51.

27. Bethel CR, Taracila M, Shyr T, Thomson JM, Distler AM, Hujer KM, Hujer AM, Endimiani A, Papp-Wallace K, Bonnet R, Bonomo RA. Exploring the Inhibition of CTX-M-9 by ?-Lactamase Inhibitors and Carbapenems ▽. Antimicrob. Agents Chemother. 2011 Jul;55(7):3465–3475.

28. Rankin DJ, Rocha EPC, Brown SP. What traits are carried on mobile genetic elements, and why? Heredity 2011 Jan;106(1):1–10.

29. Mc Ginty SÉ, Rankin DJ. The evolution of conflict resolution between plasmids and their bacterial hosts. Evol. Int. J. Org. Evol. 2012 May;66(5):1662–1670.

30. Bush K, Jacoby GA. Updated Functional Classification of β-Lactamases. Antimicrob. Agents Chemother. 2010 Mar;54(3):969–976.

31. Falagas ME, Lourida P, Poulikakos P, Rafailidis PI, Tansarli GS. Antibiotic treatment of infections due to carbapenem-resistant Enterobacteriaceae: systematic evaluation of the available evidence. Antimicrob. Agents Chemother. 2013 Sep;AAC.01222-13.

32. Beta-lactams [Internet]. Merck Man. Prof. Ed. [date unknown];

33. Weinstein AJ. The Cephalosporins: Activity and Clinical Use. Drugs 1980 Aug;20(2):137–154.

34. Kim S, Thiessen PA, Bolton EE, Chen J, Fu G, Gindulyte A, Han L, He J, He S, Shoemaker BA, Wang J, Yu B, Zhang J, Bryant SH. PubChem Substance and Compound databases. Nucleic Acids Res. 2016 Jan;44(Database issue):D1202–D1213.

35. Maveyraud L, Mourey L, Kotra LP, Pedelacq J-D, Guillet V, Mobashery S, Samama J-P. Structural Basis for Clinical Longevity of Carbapenem Antibiotics in the Face of Challenge by the Common Class A β-Lactamases from the Antibiotic-Resistant Bacteria. J. Am. Chem. Soc. 1998 Sep;120(38):9748–9752.

36. Lamotte-Brasseur J, Dive G, Dideberg O, Charlier P, Frère JM, Ghuysen JM. Mechanism of acyl transfer by the class A serine beta-lactamase of Streptomyces albus G. Biochem. J. 1991 Oct;279(Pt 1):213–221.

37. Chen Y, Bonnet R, Shoichet BK. The acylation mechanism of CTX-M beta-lactamase at 0.88 a resolution. J. Am. Chem. Soc. 2007 May;129(17):5378–5380.

38. Fonseca F, Chudyk EI, van der Kamp MW, Correia A, Mulholland AJ, Spencer J. The basis for carbapenem hydrolysis by class A β-lactamases: a combined investigation using crystallography and simulations. J. Am. Chem. Soc. 2012 Nov;134(44):18275–18285.

39. Curley K, Pratt RF. The Oxyanion Hole in Serine beta-Lactamase Catalysis: Interactions of Thiono Substrates with the Active Site. Bioorganic Chem. 2000 Dec;28(6):338–356.

40. Murphy BP, Pratt RF. Evidence for an oxyanion hole in serine beta-lactamases and DD-peptidases. Biochem. J. 1988 Dec;256(2):669–672.

41. Ke W, Bethel CR, Thomson JM, Bonomo RA, van den Akker F. Crystal structure of KPC-2: insights into carbapenemase activity in class A beta-lactamases. Biochemistry (Mosc.) 2007 May;46(19):5732–5740.

42. Strynadka NCJ, Adachi H, Jensen SE, Johns K, Sielecki A, Betzel C, Sutoh K, James MNG. Molecular structure of the acyl-enzyme intermediate in β-lactam hydrolysis at 1.7 Å resolution. Nature 1992 Oct;359(6397):359700a0.

43. Herzberg O, Moult J. Bacterial resistance to beta-lactam antibiotics: crystal structure of beta-lactamase from Staphylococcus aureus PC1 at 2.5 A resolution. Science 1987 May;236(4802):694–701.

44. Drawz SM, Bonomo RA. Three Decades of β-Lactamase Inhibitors. Clin. Microbiol. Rev. 2010 Jan;23(1):160–201.

45. Jacob F, Joris B, Lepage S, Dusart J, Frère JM. Role of the conserved amino acids of the 'SDN' loop (Ser130, Asp131 and Asn132) in a class A β-lactamase studied by site-directed mutagenesis. Biochem. J. 1990 Oct;271(2):399–406.

46. Pemberton OA, Zhang X, Chen Y. Molecular Basis of Substrate Recognition and Product Release by the Klebsiella pneumoniae Carbapenemase (KPC-2). J. Med. Chem. 2017 Apr;60(8):3525–3530.

47. Bush K, Jacoby GA, Medeiros AA. A functional classification scheme for beta-lactamases and its correlation with molecular structure. Antimicrob. Agents Chemother. 1995 Jun;39(6):1211–1233.

48. Bush K. Bench-to-bedside review: The role of beta-lactamases in antibiotic-resistant Gram-negative infections. Crit. Care Lond. Engl. 2010;14(3):224.

49. Canton R, Gonzalez-Alba JM, Galán JC. CTX-M enzymes: origin and diffusion. Antimicrob. Resist. Chemother. 2012;3:110.

50. Livermore DM, Canton R, Gniadkowski M, Nordmann P, Rossolini GM, Arlet G, Ayala J, Coque TM, Kern-Zdanowicz I, Luzzaro F, Poirel L, Woodford N. CTX-M: changing the face of ESBLs in Europe. J. Antimicrob. Chemother. 2007 Feb;59(2):165–174.

51. Cantón R, Coque TM, Baquero F. Multi-resistant Gram-negative bacilli: from epidemics to endemics. Curr. Opin. Infect. Dis. 2003 Aug;16(4):315–325.

52. Paterson DL, Bonomo RA. Extended-Spectrum β-Lactamases: a Clinical Update. Clin. Microbiol. Rev. 2005 Oct;18(4):657–686.

53. Queenan AM, Bush K. Carbapenemases: the Versatile β-Lactamases. Clin. Microbiol. Rev. 2007 Jul;20(3):440–458.

54. Bratu S, Tolaney P, Karumudi U, Quale J, Mooty M, Nichani S, Landman D. Carbapenemase-producing Klebsiella pneumoniae in Brooklyn, NY: molecular epidemiology and in vitro activity of polymyxin B and other agents. J. Antimicrob. Chemother. 2005 Jul;56(1):128–132.

55. Tracking CRE | HAI | CDC [Internet]. 2017;

56. Tumbarello M, Trecarichi EM, De Rosa FG, Giannella M, Giacobbe DR, Bassetti M, Losito AR, Bartoletti M, Del Bono V, Corcione S, Maiuro G, Tedeschi S, Celani L, Cardellino CS, Spanu T, Marchese A, Ambretti S, Cauda R, Viscoli C, Viale P, ISGRI-SITA (Italian Study Group on Resistant Infections of the Società Italiana Terapia Antinfettiva). Infections caused by KPC-producing Klebsiella pneumoniae: differences in therapy and mortality in a multicentre study. J. Antimicrob. Chemother. 2015 Jul;70(7):2133–2143.

57. Daikos GL, Tsaousi S, Tzouvelekis LS, Anyfantis I, Psichogiou M, Argyropoulou A, Stefanou I, Sypsa V, Miriagou V, Nepka M, Georgiadou S, Markogiannakis A, Goukos D, Skoutelis A. Carbapenemase-producing Klebsiella pneumoniae bloodstream infections: lowering mortality by antibiotic combination schemes and the role of carbapenems. Antimicrob. Agents Chemother. 2014;58(4):2322–2328.

58. Papp-Wallace KM, Winkler ML, Taracila MA, Bonomo RA. Variants of β-Lactamase KPC-2 That Are Resistant to Inhibition by Avibactam. Antimicrob. Agents Chemother. 2015 Jul;59(7):3710–3717.

59. Poirel L, Naas T, Thomas IL, Karim A, Bingen E, Nordmann P. CTX-M-Type Extended-Spectrum β-Lactamase That Hydrolyzes Ceftazidime through a Single Amino Acid Substitution in the Omega Loop. Antimicrob. Agents Chemother. 2001 Dec;45(12):3355–3361.

60. Bonnet R, Recule C, Baraduc R, Chanal C, Sirot D, Champs CD, Sirot J. Effect of D240G substitution in a novel ESBL CTX-M-27. J. Antimicrob. Chemother. 2003 Jul;52(1):29–35.

61. Bonnet R, Dutour C, Sampaio JL, Chanal C, Sirot D, Labia R, De Champs C, Sirot J. Novel cefotaximase (CTX-M-16) with increased catalytic efficiency due to substitution Asp-240-->Gly. Antimicrob. Agents Chemother. 2001 Aug;45(8):2269–2275.

62. Cortina GA, Kasson PM. Excess positional mutual information predicts both local and allosteric mutations affecting beta lactamase drug resistance. Bioinformatics 2016 Jul;btw492.

63. J. Latallo M, A. Cortina G, Faham S, K. Nakamoto R, M. Kasson P. Predicting allosteric mutants that increase activity of a major antibiotic resistance enzyme. Chem. Sci. 2017;8(9):6484–6492.

64. Papp-Wallace KM, Taracila M, Wallace CJ, Hujer KM, Bethel CR, Hornick JM, Bonomo RA. Elucidating the role of Trp105 in the KPC-2 β-lactamase. Protein Sci. Publ. Protein Soc. 2010 Sep;19(9):1714–1727.

65. Papp-Wallace KM, Taracila M, Hornick JM, Hujer AM, Hujer KM, Distler AM, Endimiani A, Bonomo RA. Substrate Selectivity and a Novel Role in Inhibitor Discrimination by Residue 237 in the KPC-2 β-Lactamase. Antimicrob. Agents Chemother. 2010 Jul;54(7):2867–2877.

66. Papp-Wallace KM, Taracila MA, Smith KM, Xu Y, Bonomo RA. Understanding the Molecular Determinants of Substrate and Inhibitor Specificities in the Carbapenemase

KPC-2: Exploring the Roles of Arg220 and Glu276. Antimicrob. Agents Chemother. 2012 Aug;56(8):4428–4438.

67. Joachimiak A, Katzenellenbogen BS, Greene GL, Gil G, Zhou H, Nowak J, Katzenellenbogen JA, Bruning JB, Hahm JB, Nettles KW, Kulp K, Hochberg RB, Sharma SK, Kim Y. NFκB selectivity of estrogen receptor ligands revealed by comparative crystallographic analyses. Nat. Chem. Biol. 2008 Apr;4(4):nchembio.76.

68. Valentini G, Chiarelli L, Fortin R, Speranza ML, Galizzi A, Mattevi A. The Allosteric Regulation of Pyruvate Kinase A SITE-DIRECTED MUTAGENESIS STUDY. J. Biol. Chem. 2000 Jun;275(24):18145–18152.

69. Gidh-Jain M, Zhang Y, Poelje PD van, Liang JY, Huang S, Kim J, Elliott JT, Erion MD, Pilkis SJ, el-Maghrabi MR. The allosteric site of human liver fructose-1,6-bisphosphatase. Analysis of six AMP site mutants based on the crystal structure. J. Biol. Chem. 1994 Nov;269(44):27732–27738.

70. Verma D, Jacobs DJ, Livesay DR. Variations within Class-A β-Lactamase Physiochemical Properties Reflect Evolutionary and Environmental Patterns, but not Antibiotic Specificity. PLOS Comput. Biol. 2013 Jul;9(7):e1003155.

71. Juárez-Vázquez AL, Edirisinghe JN, Verduzco-Castro EA, Michalska K, Wu C, Noda-García L, Babnigg G, Endres M, Medina-Ruíz S, Santoyo-Flores J, Carrillo-Tripp M, Ton-That H, Joachimiak A, Henry CS, Barona-Gómez F. Evolution of substrate specificity in a retained enzyme driven by gene loss [Internet]. eLife [date unknown];6

72. Goh CS, Bogan AA, Joachimiak M, Walther D, Cohen FE. Co-evolution of proteins with their interaction partners. J. Mol. Biol. 2000 Jun;299(2):283–293.

73. Kawaguchi M, Inoue K, Iuchi I, Nishida M, Yasumasu S. Molecular co-evolution of a protease and its substrate elucidated by analysis of the activity of predicted ancestral hatching enzyme. BMC Evol. Biol. 2013 Oct;13:231.

74. Altschul SF, Gish W, Miller W, Myers EW, Lipman DJ. Basic local alignment search tool. J. Mol. Biol. 1990 Oct;215(3):403–410.

75. Walther-Rasmussen J, Høiby N. Class A carbapenemases. J. Antimicrob. Chemother. 2007 Sep;60(3):470–482.

76. Hall BG, Barlow M. Evolution of the serine β-lactamases: past, present and future. Drug Resist. Updat. 2004 Apr;7(2):111–123.

77. Wright GD, Poinar H. Antibiotic resistance is ancient: implications for drug discovery. Trends Microbiol. 2012 Apr;20(4):157–159.

78. Massova I, Mobashery S. Kinship and Diversification of Bacterial Penicillin-Binding Proteins and β-Lactamases. Antimicrob. Agents Chemother. 1998 Jan;42(1):1–17.

79. Sarria JC, Vidal AM, Kimbrough RC. Infections Caused by Kluyvera Species in Humans. Clin. Infect. Dis. 2001 Oct;33(7):e69–e74.

80. Ashkenazy H, Erez E, Martz E, Pupko T, Ben-Tal N. ConSurf 2010: calculating evolutionary conservation in sequence and structure of proteins and nucleic acids. Nucleic Acids Res. 2010 Jul;38(suppl 2):W529–W533.

81. Guthrie VB, Allen J, Camps M, Karchin R. Network Models of TEM β-Lactamase Mutations Coevolving under Antibiotic Selection Show Modular Structure and Anticipate Evolutionary Trajectories. PLOS Comput. Biol. 2011 Sep;7(9):e1002184.

82. Yang J-S, Seo SW, Jang S, Jung GY, Kim S. Rational Engineering of Enzyme Allosteric Regulation through Sequence Evolution Analysis. PLOS Comput. Biol. 2012 Jul;8(7):e1002612.

83. Salverda MLM, De Visser JAGM, Barlow M. Natural evolution of TEM-1 β-lactamase: experimental reconstruction and clinical relevance. FEMS Microbiol. Rev. 2010 Nov;34(6):1015–1036.

84. De Luca F, Benvenuti M, Carboni F, Pozzi C, Rossolini GM, Mangani S, Docquier J-D. Evolution to carbapenem-hydrolyzing activity in noncarbapenemase class D β-lactamase OXA-10 by rational protein design. Proc. Natl. Acad. Sci. U. S. A. 2011 Nov;108(45):18424–18429.

85. Weinreich DM, Delaney NF, DePristo MA, Hartl DL. Darwinian Evolution Can Follow Only Very Few Mutational Paths to Fitter Proteins. Science 2006 Apr;312(5770):111–114.

86. Fraser JS, van den Bedem H, Samelson AJ, Lang PT, Holton JM, Echols N, Alber T. Accessing protein conformational ensembles using room-temperature X-ray crystallography. Proc. Natl. Acad. Sci. U. S. A. 2011 Sep;108(39):16247–16252.

87. Hospital A, Goñi JR, Orozco M, Gelpí JL. Molecular dynamics simulations: advances and applications. Adv. Appl. Bioinforma. Chem. AABC 2015 Nov;8:37–47.

88. Lu C, Stock G, Knecht V. Mechanisms for allosteric activation of protease DegS by ligand binding and oligomerization as revealed from molecular dynamics simulations. Proteins Struct. Funct. Bioinforma. 2016 Nov;84(11):1690–1705.

89. Bowman GR, Bolin ER, Hart KM, Maguire BC, Marqusee S. Discovery of multiple hidden allosteric sites by combining Markov state models and experiments. Proc. Natl. Acad. Sci. 2015 Mar;112(9):2734–2739.

90. Mouchlis VD, Bucher D, McCammon JA, Dennis EA. Membranes serve as allosteric activators of phospholipase A2, enabling it to extract, bind, and hydrolyze phospholipid substrates. Proc. Natl. Acad. Sci. 2015 Feb;112(6):E516–E525.

91. Oliva M, Dideberg O, Field MJ. Understanding the acylation mechanisms of active-site serine penicillin-recognizing proteins: A molecular dynamics simulation study. Proteins Struct. Funct. Bioinforma. 2003 Oct;53(1):88–100.

92. Hart KM, Ho CMW, Dutta S, Gross ML, Bowman GR. Modelling proteins' hidden conformations to predict antibiotic resistance. Nat. Commun. 2016 Oct;7:ncomms12965.

93. Hart KM, Moeder KE, Ho CMW, Zimmerman MI, Frederick TE, Bowman GR. Designing small molecules to target cryptic pockets yields both positive and negative allosteric modulators. PloS One 2017;12(6):e0178678.

94. Bowerman S, Wereszczynski J. Detecting Allosteric Networks Using Molecular Dynamics Simulation. Methods Enzymol. 2016;578:429–447.

95. Vallee BL, Riordan JF. Dynamics of local conformation and enzyme function. Ciba Found. Symp. 1977;(60):197–223.

96. Nussinov R, G. Wolynes P. A second molecular biology revolution? The energy landscapes of biomolecular function. Phys. Chem. Chem. Phys. 2014;16(14):6321–6322.

97. Monod J, Wyman J, Changeux J-P. On the nature of allosteric transitions: A plausible model. J. Mol. Biol. 1965 May;12(1):88–118.

98. Nussinov R. Introduction to Protein Ensembles and Allostery. Chem. Rev. 2016 Jun;116(11):6263–6266.

99. Weinkam P, Chen YC, Pons J, Sali A. Impact of mutations on the allosteric conformational equilibrium. J. Mol. Biol. 2013 Feb;425(3):647–661.

100. Aumeran C, Chanal C, Labia R, Sirot D, Sirot J, Bonnet R. Effects of Ser130Gly and Asp240Lys Substitutions in Extended-Spectrum β-Lactamase CTX-M-9. Antimicrob. Agents Chemother. 2003 Sep;47(9):2958–2961.

101. Pérez-Llarena FJ, Kerff F, Abián O, Mallo S, Fernández MC, Galleni M, Sancho J, Bou G. Distant and New Mutations in CTX-M-1 β-Lactamase Affect Cefotaxime Hydrolysis. Antimicrob. Agents Chemother. 2011 Sep;55(9):4361–4368.

102. Pérez-Llarena FJ, Cartelle M, Mallo S, Beceiro A, Pérez A, Villanueva R, Romero A, Bonnet R, Bou G. Structure-function studies of arginine at position 276 in CTX-M beta-lactamases. J. Antimicrob. Chemother. 2008 Apr;61(4):792–797.

103. Gazouli M, Tzelepi E, Sidorenko SV, Tzouvelekis LS. Sequence of the gene encoding a plasmid-mediated cefotaxime-hydrolyzing class A beta-lactamase (CTX-M-4): involvement of serine 237 in cephalosporin hydrolysis. Antimicrob. Agents Chemother. 1998 May;42(5):1259–1262.

104. Sougakoff W, Goussard S, Courvalin P. The TEM-3 β-lactamase, which hydrolyzes broad-spectrum cephalosporins, is derived from the TEM-2 penicillinase by two amino acid substitutions. FEMS Microbiol. Lett. 1988 Dec;56(3):343–348.

105. Poirel L, Gniadkowski M, Nordmann P. Biochemical analysis of the ceftazidime-hydrolysing extended-spectrum beta-lactamase CTX-M-15 and of its structurally related beta-lactamase CTX-M-3. J. Antimicrob. Chemother. 2002 Dec;50(6):1031–1034.

106. Delmas J, Robin F, Carvalho F, Mongaret C, Bonnet R. Prediction of the Evolution of Ceftazidime Resistance in Extended-Spectrum β-Lactamase CTX-M-9. Antimicrob. Agents Chemother. 2006 Feb;50(2):731–738.

107. Xu D, Guo H, Cui Q. Antibiotic deactivation by a dizinc beta-lactamase: mechanistic insights from QM/MM and DFT studies. J. Am. Chem. Soc. 2007 Sep;129(35):10814–10822.

108. Hermann JC, Pradon J, Harvey JN, Mulholland AJ. High Level QM/MM Modeling of the Formation of the Tetrahedral Intermediate in the Acylation of Wild Type and K73A Mutant TEM-1 Class A β-Lactamase†. J. Phys. Chem. A 2009 Oct;113(43):11984–11994.

109. Nichols DA, Hargis JC, Sanishvili R, Jaishankar P, Defrees K, Smith EW, Wang KK, Prati F, Renslo AR, Woodcock HL, Chen Y. Ligand-Induced Proton Transfer and Low-Barrier Hydrogen Bond Revealed by X-ray Crystallography. J. Am. Chem. Soc. 2015 Jul;137(25):8086–8095.

110. Rod TH, Radkiewicz JL, Brooks CL. Correlated motion and the effect of distal mutations in dihydrofolate reductase. Proc. Natl. Acad. Sci. 2003 Jun;100(12):6980–6985.

111. Watney JB, Agarwal PK, Hammes-Schiffer S. Effect of mutation on enzyme motion in dihydrofolate reductase. J. Am. Chem. Soc. 2003 Apr;125(13):3745–3750.

112. Karplus M, Kuriyan J. Molecular dynamics and protein function. Proc. Natl. Acad. Sci. U. S. A. 2005 May;102(19):6679–6685.

113. Cover TM, Thomas JA. Elements of Information Theory. New York, NY, USA: John Wiley & Sons; 2012.

114. Kasson PM, Ensign DL, Pande VS. Combining molecular dynamics with bayesian analysis to predict and evaluate ligand-binding mutations in influenza hemagglutinin. J. Am. Chem. Soc. 2009 Aug;131(32):11338–11340.

115. Kamberaj H, van der Vaart A. Extracting the causality of correlated motions from molecular dynamics simulations. Biophys. J. 2009 Sep;97(6):1747–1755.

116. Karplus M, Kushick JN. Method for estimating the configurational entropy of macromolecules. Macromolecules 1981 Mar;14(2):325–332.

117. Ichiye T, Karplus M. Collective motions in proteins: a covariance analysis of atomic fluctuations in molecular dynamics and normal mode simulations. Proteins 1991;11(3):205–217.

118. Lange OF, Grubmüller H. Generalized correlation for biomolecular dynamics. Proteins Struct. Funct. Bioinforma. 2006 Mar;62(4):1053–1061.

119. Brandman R, Brandman Y, Pande VS. A-Site Residues Move Independently from P-Site Residues in all-Atom Molecular Dynamics Simulations of the 70S Bacterial Ribosome. PLoS ONE 2012 Jan;7(1):e29377.

120. Chen Y, Shoichet B, Bonnet R. Structure, function, and inhibition along the reaction coordinate of CTX-M beta-lactamases. J. Am. Chem. Soc. 2005 Apr;127(15):5423–5434.

121. Nukaga M, Bethel CR, Thomson JM, Hujer AM, Distler A, Anderson VE, Knox JR, Bonomo RA. Inhibition of class A beta-lactamases by carbapenems: crystallographic observation of two conformations of meropenem in SHV-1. J.Am.Chem.Soc. 2007 Nov;130:12656–12662.

122. Case DA, Darden TA, Cheatham III TE, Simmerling CL, Wang J, Duke RE, Luo R, Merz KM, Pearlman DA, Crowley M. AMBER 9. Univ. Calif. San Franc. 2006;45

123. Pronk S, Páll S, Schulz R, Larsson P, Bjelkmar P, Apostolov R, Shirts MR, Smith JC, Kasson PM, Spoel D van der, Hess B, Lindahl E. GROMACS 4.5: a high-throughput and highly parallel open source molecular simulation toolkit. Bioinformatics 2013 Apr;29(7):845–854.

124. Hornak V, Abel R, Okur A, Strockbine B, Roitberg A, Simmerling C. Comparison of multiple Amber force fields and development of improved protein backbone parameters. Proteins Struct. Funct. Bioinforma. 2006 Nov;65(3):712–725.

125. Lindorff-Larsen K, Piana S, Palmo K, Maragakis P, Klepeis JL, Dror RO, Shaw DE. Improved side-chain torsion potentials for the Amber ff99SB protein force field. Proteins Struct. Funct. Bioinforma. 2010;NA-NA.

126. Hess B, Bekker H, Berendsen HJC, Fraaije JGEM. LINCS: A linear constraint solver for molecular simulations. J. Comput. Chem. 1997;18(12):1463–1472.

127. Bussi G, Donadio D, Parrinello M. Canonical sampling through velocity rescaling. J. Chem. Phys. 2007 Jan;126(1):014101.

128. Darden T, York D, Pedersen L. Particle mesh Ewald: An N · log(N) method for Ewald sums in large systems. J. Chem. Phys. 1993 Jun;98(12):10089–10092.

129. Leinberger DM, Grimm V, Rubtsova M, Weile J, Schröppel K, Wichelhaus TA, Knabbe C, Schmid RD, Bachmann TT. Integrated Detection of Extended-Spectrum-Beta-Lactam Resistance by DNA Microarray-Based Genotyping of TEM, SHV, and CTX-M Genes. J. Clin. Microbiol. 2010 Feb;48(2):460–471.

130. Edgar RC. MUSCLE: multiple sequence alignment with high accuracy and high throughput. Nucleic Acids Res. 2004 Mar;32(5):1792–1797.

131. Saladin M, Cao VTB, Lambert T, Donay J-L, Herrmann J-L, Ould-Hocine Z, Verdet C, Delisle F, Philippon A, Arlet G. Diversity of CTX-M beta-lactamases and their promoter regions from Enterobacteriaceae isolated in three Parisian hospitals. FEMS Microbiol. Lett. 2002 Apr;209(2):161–168.

132. Bauer AW, Perry DM, Kirby WM. Single-disk antibiotic-sensitivity testing of staphylococci: An analysis of technique and results. AMA Arch. Intern. Med. 1959 Aug;104(2):208–216.

133. Warshel A. Electrostatic Origin of the Catalytic Power of Enzymes and the Role of Preorganized Active Sites. J. Biol. Chem. 1998 Oct;273(42):27035–27038.

134. Warshel A. Molecular dynamics simulations of biological reactions. Acc. Chem. Res. 2002 Jun;35(6):385–395.

135. Delmas J, Chen Y, Prati F, Robin F, Shoichet BK, Bonnet R. Structure and Dynamics of CTX-M Enzymes Reveal Insights into Substrate Accommodation by Extended-spectrum β-Lactamases. J. Mol. Biol. 2008 Jan;375(1):192–201.

136. Shimamura T, Ibuka A, Fushinobu S, Wakagi T, Ishiguro M, Ishii Y, Matsuzawa H. Acyl-intermediate structures of the extended-spectrum class A beta-lactamase, Toho-1, in complex with cefotaxime, cephalothin, and benzylpenicillin. J. Biol. Chem. 2002 Nov;277(48):46601–46608.

137. Jack BR, Meyer AG, Echave J, Wilke CO. Functional Sites Induce Long-Range Evolutionary Constraints in Enzymes [Internet]. PLoS Biol. 2016 May;14(5)

138. Tomanicek SJ, Wang KK, Weiss KL, Blakeley MP, Cooper J, Chen Y, Coates L. The active site protonation states of perdeuterated Toho-1 β-lactamase determined by neutron diffraction support a role for Glu166 as the general base in acylation. FEBS Lett. 2011 Jan;585(2):364–368.

139. Cartelle M, Tomas M del M, Molina F, Moure R, Villanueva R, Bou G. High-Level Resistance to Ceftazidime Conferred by a Novel Enzyme, CTX-M-32, Derived from CTX-M-1 through a Single Asp240-Gly Substitution. Antimicrob. Agents Chemother. 2004 Jun;48(6):2308–2313.

140. Hujer AM, Hujer KM, Bonomo RA. Mutagenesis of amino acid residues in the SHV-1 β-lactamase: the premier role of Gly238Ser in penicillin and cephalosporin resistance. Biochim. Biophys. Acta BBA - Protein Struct. Mol. Enzymol. 2001 May;1547(1):37–50.

141. Perez-Llarena FJ, Kerff F, Abian O, Mallo S, Fernandez MC, Galleni M, Sancho J, Bou G. Distant and new mutations in CTX-M-1 beta-lactamase affect cefotaxime hydrolysis. Antimicrob Agents Chemother 2011 Sep;55(9):4361–8.

142. Sun T, Bethel CR, Bonomo RA, Knox JR. Inhibitor-resistant class A beta-lactamases: consequences of the Ser130-to-Gly mutation seen in Apo and tazobactam structures of the SHV-1 variant. Biochemistry (Mosc.) 2004 Nov;43(44):14111–14117.

143. Totir MA, Padayatti PS, Helfand MS, Carey MP, Bonomo RA, Carey PR, van den Akker F. Effect of the inhibitor-resistant M69V substitution on the structures and populations of trans-enamine beta-lactamase intermediates. Biochemistry (Mosc.) 2006 Oct;45(39):11895–11904.

144. Christensen H, Martin MT, Waley SG. Beta-lactamases as fully efficient enzymes. Determination of all the rate constants in the acyl-enzyme mechanism. Biochem. J. 1990 Mar;266(3):853–861.

145. Saves I, Burlet-Schiltz O, Maveyraud L, Samama JP, Promé JC, Masson JM. Mass spectral kinetic study of acylation and deacylation during the hydrolysis of penicillins and cefotaxime by beta-lactamase TEM-1 and the G238S mutant. Biochemistry (Mosc.) 1995 Sep;34(37):11660–11667.

146. Adamski CJ, Cardenas AM, Brown NG, Horton LB, Sankaran B, Prasad BVV, Gilbert HF, Palzkill T. Molecular basis for the catalytic specificity of the CTX-M extended-spectrum β-lactamases. Biochemistry (Mosc.) 2015 Jan;54(2):447–457.

147. Zou T, Risso VA, Gavira JA, Sanchez-Ruiz JM, Ozkan SB. Evolution of conformational dynamics determines the conversion of a promiscuous generalist into a specialist enzyme. Mol. Biol. Evol. 2015 Jan;32(1):132–143.

148. Jakalian A, Jack DB, Bayly CI. Fast, efficient generation of high-quality atomic charges. AM1-BCC model: II. Parameterization and validation. J. Comput. Chem. 2002 Dec;23(16):1623–1641.

149. Wang J, Wolf RM, Caldwell JW, Kollman PA, Case DA. Development and testing of a general amber force field. J Comput Chem 2004 Jul;25(9):1157–74.

150. Berendsen HJC, Postma JPM, Gunsteren WF van, DiNola A, Haak JR. Molecular dynamics with coupling to an external bath. J. Chem. Phys. 1984 Oct;81(8):3684–3690.

151. Bauer AW, Kirby WM, Sherris JC, Turck M. Antibiotic susceptibility testing by a standardized single disk method. Am. J. Clin. Pathol. 1966 Apr;45(4):493–496.

152. Hudzicki J. Kirby-Bauer disk diffusion susceptibility test protocol. Am Soc Microbiol 2009;

153. Thomas VL, McReynolds AC, Shoichet BK. Structural bases for stability-function tradeoffs in antibiotic resistance. J Mol Biol 2010 Feb;396(1):47–59.

154. Wang X, Minasov G, Shoichet BK. Evolution of an antibiotic resistance enzyme constrained by stability and activity trade-offs. J Mol Biol 2002 Jun;320(1):85–95.

155. Bernstein NJ, Pratt RF. On the importance of a methyl group in beta-lactamase evolution: free energy profiles and molecular modeling. Biochemistry (Mosc.) 1999 Aug;38(32):10499–510.

156. Doucet N, De Wals PY, Pelletier JN. Site-saturation mutagenesis of Tyr-105 reveals its importance in substrate stabilization and discrimination in TEM-1 beta-lactamase. J Biol Chem 2004 Oct;279(44):46295–303.

157. Escobar WA, Miller J, Fink AL. Effects of site-specific mutagenesis of tyrosine 105 in a class A beta-lactamase. Biochem J 1994 Oct;303 (Pt 2):555–8.

158. Petit A, Maveyraud L, Lenfant F, Samama JP, Labia R, Masson JM. Multiple substitutions at position 104 of beta-lactamase TEM-1: assessing the role of this residue in substrate specificity. Biochem J 1995 Jan;305 (Pt 1):33–40.

159. Peng H, Long F, Ding C. Feature selection based on mutual information: criteria of max-dependency, max-relevance, and min-redundancy. IEEE Trans. Pattern Anal. Mach. Intell. 2005 Aug;27(8):1226–1238.

160. Dunn SD, Wahl LM, Gloor GB. Mutual information without the influence of phylogeny or entropy dramatically improves residue contact prediction. Bioinformatics 2008 Feb;24(3):333–40.

161. Bisignano P, Doerr S, Harvey MJ, Favia AD, Cavalli A, De Fabritiis G. Kinetic characterization of fragment binding in AmpC beta-lactamase by high-throughput molecular simulations. J Chem Inf Model 2014 Feb;54(2):362–6.

162. Bos F, Pleiss J. Multiple molecular dynamics simulations of TEM beta-lactamase: dynamics and water binding of the omega-loop. Biophys J 2009 Nov;97(9):2550–8.

163. Chudyk EI, Limb MA, Jones C, Spencer J, van der Kamp MW, Mulholland AJ. QM/MM simulations as an assay for carbapenemase activity in class A beta-lactamases. Chem Commun Camb 2014 Dec;50(94):14736–9.

164. Hermann JC, Hensen C, Ridder L, Mulholland AJ, Holtje HD. Mechanisms of antibiotic resistance: QM/MM modeling of the acylation reaction of a class A beta-lactamase with benzylpenicillin. J Am Chem Soc 2005 Mar;127(12):4454–65.

165. Lamotte-Brasseur J, Lounnas V, Raquet X, Wade RC. pKa calculations for class A beta-lactamases: influence of substrate binding. Protein Sci 1999 Feb;8(2):404–9.

166. Suarez D, Diaz N, Merz KM. Molecular dynamics simulations of the dinuclear zinc-beta-lactamase from Bacteroides fragilis complexed with imipenem. J Comput Chem 2002 Dec;23(16):1587–600.

167. Wade RC, Gabdoulline RR, Ludemann SK, Lounnas V. Electrostatic steering and ionic tethering in enzyme-ligand binding: insights from simulations. Proc Natl Acad Sci U A 1998 May;95(11):5942–9.

168. Aminov RI, Mackie RI. Evolution and ecology of antibiotic resistance genes. FEMS Microbiol Lett 2007 Jun;271(2):147–61.

169. Davies J, Davies D. Origins and evolution of antibiotic resistance. Microbiol Mol Biol Rev 2010 Sep;74(3):417–33.

170. Martinez JL. Antibiotics and antibiotic resistance genes in natural environments. Science 2008 Jul;321(5887):365–7.

171. Motlagh HN, Wrabl JO, Li J, Hilser VJ. The ensemble nature of allostery. Nature 2014 Apr;508(7496):331–9.

172. Kalp M, Carey PR. Carbapenems and SHV-1 β-Lactamase Form Different Acyl-Enzyme Populations in Crystals and Solution. Biochemistry (Mosc.) 2008 Nov;47(45):11830–11837.

173. Wilkinson AS, Ward S, Kania M, Page MG, Wharton CW. Multiple conformations of the acylenzyme formed in the hydrolysis of methicillin by Citrobacter freundii beta-lactamase: a time-resolved FTIR spectroscopic study. Biochemistry (Mosc.) 1999 Mar;38(13):3851–3856.

174. Citri N, Samuni A, Zyk N. Acquisition of substrate-specific parameters during the catalytic reaction of penicillinase. Proc. Natl. Acad. Sci. U. S. A. 1976 Apr;73(4):1048–1052.

175. Page MGP. The kinetics of non-stoichiometric bursts of β-lactam hydrolysis catalysed by class C β-lactamases. Biochem. J. 1993 Oct;295(1):295–304.

176. Page MGP. Extended-spectrum β-lactamases: structure and kinetic mechanism. Clin. Microbiol. Infect. 2008 Jan;14:63–74.

177. Pratt RF. ß-Lactamase: inhibition [Internet]. In: The Chemistry of β-Lactams. Springer, Dordrecht; 1992 p. 229–271.

178. Waley SG. ß-Lactamase: mechanism of action [Internet]. In: The Chemistry of β-Lactams. Springer, Dordrecht; 1992 p. 198–228.

179. Kasson PM, Lindahl E, Pande VS. Atomic-Resolution Simulations Predict a Transition State for Vesicle Fusion Defined by Contact of a Few Lipid Tails. PLOS Comput. Biol. 2010 Jun;6(6):e1000829.

180. Pande VS, Rokhsar DS. Folding pathway of a lattice model for proteins. Proc. Natl. Acad. Sci. 1999 Feb;96(4):1273–1278.

181. Du R, Pande VS, Grosberg AY, Tanaka T, Shakhnovich ES. On the transition coordinate for protein folding. J. Chem. Phys. 1998 Jan;108(1):334–350.

182. Yang L, Tan C, Hsieh M-J, Wang J, Duan Y, Cieplak P, Caldwell J, Kollman PA, Luo R. New-Generation Amber United-Atom Force Field. J. Phys. Chem. B 2006 Jul;110(26):13166–13176.

183. Röblitz S, Weber M. Fuzzy Spectral Clustering by PCCA+: Application to Markov State Models and Data Classification. Adv Data Anal Classif 2013 Jun;7(2):147–179.

184. Wernet P, Nordlund D, Bergmann U, Cavalleri M, Odelius M, Ogasawara H, Näslund LÅ, Hirsch TK, Ojamäe L, Glatzel P, Pettersson LGM, Nilsson A. The Structure of the First Coordination Shell in Liquid Water [Internet]. Science 2004 Apr;

185. White AD, Voth GA. Efficient and Minimal Method to Bias Molecular Simulations with Experimental Data. J. Chem. Theory Comput. 2014 Aug;10(8):3023–3030.

186. Sali A, Blundell TL. Comparative protein modelling by satisfaction of spatial restraints. J. Mol. Biol. 1993 Dec;234(3):779–815.

187. I. Chudyk E, L. Limb MA, Jones C, Spencer J, Kamp MW van der, J. Mulholland A. QM/MM simulations as an assay for carbapenemase activity in class A β-lactamases. Chem. Commun. 2014;50(94):14736–14739.

188. Goff DA, Jankowski C, Tenover FC. Using rapid diagnostic tests to optimize antimicrobial selection in antimicrobial stewardship programs. Pharmacotherapy 2012 Aug;32(8):677–687.

189. Cavin RK, Lugli P, Zhirnov VV. Science and Engineering Beyond Moore's Law. Proc. IEEE 2012 May;100(Special Centennial Issue):1720–1749.

190. Drawz SM, Bethel CR, Hujer KM, Hurless KN, Distler AM, Caselli E, Prati F, Bonomo RA. The role of a second-shell residue in modifying substrate and inhibitor interactions in the SHV beta-lactamase: a study of ambler position Asn276. Biochemistry (Mosc.) 2009 Jun;48(21):4557–4566.

191. Wang D, Chen J, Yang L, Mou Y, Yang Y. Phenotypic and Enzymatic Comparative Analysis of the KPC Variants, KPC-2 and Its Recently Discovered Variant KPC-15. PLOS ONE 2014 Oct;9(10):e111491.

192. Jones G, Willett P, Glen RC, Leach AR, Taylor R. Development and validation of a genetic algorithm for flexible docking1. J. Mol. Biol. 1997 Apr;267(3):727–748.

193. Dandekar T, Argos P. Potential of genetic algorithms in protein folding and protein engineering simulations. Protein Eng. 1992 Oct;5(7):637–645.

194. Morin S, Clouthier CM, Gobeil S, Pelletier JN, Gagné SM. Backbone resonance assignments of an artificially engineered TEM-1/PSE-4 Class A β-lactamase chimera. Biomol. NMR Assign. 2010 Oct;4(2):127–130.

195. Coleman K. Diazabicyclooctanes (DBOs): a potent new class of non-β-lactam β-lactamase inhibitors. Curr. Opin. Microbiol. 2011 Oct;14(5):550–555.

196. Shlaes DM. New β-lactam–β-lactamase inhibitor combinations in clinical development. Ann. N. Y. Acad. Sci. 2013;1277(1):105–114.

197. Livermore DM, Warner M, Jamrozy D, Mushtaq S, Nichols WW, Mustafa N, Woodford N. In Vitro Selection of Ceftazidime-Avibactam Resistance in Enterobacteriaceae with KPC-3 Carbapenemase. Antimicrob. Agents Chemother. 2015 Sep;59(9):5324–5330.

198. Shields RK, Chen L, Cheng S, Chavda KD, Press EG, Snyder A, Pandey R, Doi Y, Kreiswirth BN, Nguyen MH, Clancy CJ. Emergence of Ceftazidime-Avibactam Resistance Due to Plasmid-Borne blaKPC-3 Mutations during Treatment of Carbapenem-Resistant Klebsiella pneumoniae Infections. Antimicrob. Agents Chemother. 2017 Mar;61(3):e02097-16.

199. Krishnan NP, Nguyen NQ, Papp-Wallace KM, Bonomo RA, van den Akker F. Inhibition of Klebsiella β-Lactamases (SHV-1 and KPC-2) by Avibactam: A Structural Study. PloS One 2015;10(9):e0136813.

200. Ehmann DE, Jahić H, Ross PL, Gu R-F, Hu J, Durand-Réville TF, Lahiri S, Thresher J, Livchak S, Gao N, Palmer T, Walkup GK, Fisher SL. Kinetics of Avibactam Inhibition against Class A, C, and D β-Lactamases [Internet]. [date unknown];

201. Malliaros FD, Vazirgiannis M. Clustering and Community Detection in Directed Networks: A Survey. Phys. Rep. 2013 Dec;533(4):95–142.

202. Kuramochi M, Karypis G. Frequent subgraph discovery. In: Proceedings 2001 IEEE International Conference on Data Mining. 2001 p. 313–320.

203. Langfelder P, Horvath S. WGCNA: an R package for weighted correlation network analysis. BMC Bioinformatics 2008 Dec;9:559.

204. Girvan M, Newman MEJ. Community structure in social and biological networks. Proc. Natl. Acad. Sci. 2002 Jun;99(12):7821–7826.

205. Johnson SC. Hierarchical clustering schemes. Psychometrika 1967 Sep;32(3):241–254.

206. Kraskov A, Stögbauer H, Andrzejak RG, Grassberger P. Hierarchical Clustering Based on Mutual Information [Internet]. ArXivq-Bio0311039 2003 Nov;

207. Horvath S, Zhang B, Carlson M, Lu KV, Zhu S, Felciano RM, Laurance MF, Zhao W, Qi S, Chen Z, Lee Y, Scheck AC, Liau LM, Wu H, Geschwind DH, Febbo PG, Kornblum HI, Cloughesy TF, Nelson SF, Mischel PS. Analysis of oncogenic signaling networks in glioblastoma identifies ASPM as a molecular target. Proc. Natl. Acad. Sci. 2006 Nov;103(46):17402–17407.

208. Langfelder P, Horvath S. Eigengene networks for studying the relationships between co-expression modules. BMC Syst. Biol. 2007 Nov;1:54.

209. Collaborative Computational Project N. The CCP4 suite: programs for protein crystallography. Acta Crystallogr Biol Crystallogr 1994 Sep;50(Pt 5):760–3.

210. McCoy AJ, Grosse-Kunstleve RW, Adams PD, Winn MD, Storoni LC, Read RJ. Phaser crystallographic software. J Appl Crystallogr 2007 Aug;40(Pt 4):658–674.

211. Emsley P, Lohkamp B, Scott WG, Cowtan K. Features and development of Coot. Acta Crystallogr Biol Crystallogr 2010 Apr;66(Pt 4):486–501.

212. Fiser A, Sali A. Modeller: generation and refinement of homology-based protein structure models. Methods Enzym. 2003;374:461–91.

213. Li H, Robertson AD, Jensen JH. Very fast empirical prediction and rationalization of protein pKa values. Proteins 2005 Dec;61(4):704–21.

214. Fox N, Jagodzinski F, Li Y, Streinu I. KINARI-Web: a server for protein rigidity analysis. Nucleic Acids Res 2011 Jul;39(Web Server issue):W177-83.

215. Jacobs DJ, Rader AJ, Kuhn LA, Thorpe MF. Protein flexibility predictions using graph theory. Proteins 2001 Aug;44(2):150–65.

216. Beauchamp KA, Bowman GR, Lane TJ, Maibaum L, Haque IS, Pande VS. MSMBuilder2: Modeling Conformational Dynamics at the Picosecond to Millisecond Scale. J. Chem. Theory Comput. 2011 Oct;7(10):3412–3419.